

2018

A wearable near-infrared diffuse optical system for monitoring in vivo breast tumor hemodynamics during chemotherapy infusions

<https://hdl.handle.net/2144/32083>

Downloaded from DSpace Repository, DSpace Institution's institutional repository

BOSTON UNIVERSITY
COLLEGE OF ENGINEERING

Dissertation

**A WEARABLE NEAR-INFRARED DIFFUSE OPTICAL SYSTEM FOR
MONITORING IN VIVO BREAST TUMOR HEMODYNAMICS
DURING CHEMOTHERAPY INFUSIONS**

by

FEI TENG

B.S., South China Normal University, 2009

Submitted in partial fulfillment of the
requirements for the degree of
Doctor of Philosophy

2018

Approved by

First Reader

Darren Roblyer, Ph.D.
Assistant Professor of Biomedical Engineering

Second Reader

Irving J. Bigio, Ph.D.
Professor of Biomedical Engineering
Professor of Electrical and Computer Engineering
Professor of Physics
Professor of Medicine

Third Reader

Michelle Sander, Ph.D.
Assistant Professor of Electrical and Computer Engineering
Assistant Professor of Materials Science and Engineering

Fourth Reader

Muhammad H. Zaman, Ph.D.
Professor of Biomedical Engineering
Professor of Materials Science and Engineering

Fifth Reader

Shyamsunder Erramilli, Ph.D.
Professor of Physics
Professor of Biomedical Engineering
Professor of Materials Science and Engineering

ACKNOWLEDGEMENTS

During my graduate study at Boston University, I have been fortunate to receive help from so many people around. They made this work possible.

First, I would like to express my gratitude to my advisor Dr. Darren Roblyer. Thank you for taking me to the field of diffuse optics, shaping my interest in medical imaging, teaching me how to approach and identify problems, and showing me an example in becoming a motivated, productive, reliable, and entrepreneurial professional.

Second, I wish to extend my gratitude to my committee members: Dr. Irving Bigio, Dr. Michelle Sander, Dr. Muhammad Zaman, and Dr. Shyamsunder Erramilli, for your patience, insightful comments, and kind help. A special thanks to Dr. Bigio for the preprint of your book chapters, also your mini-lectures.

Third, I want to thank Dr. Anna Swan, Dr. Roberto Paiella, Dr. Enrico Bellotti, and Dr. Luca Dal Negro for your endorsement on my academic competence, also your recommendation letters for my Ph.D. application at Boston University ECE department.

Fourth, I want to thank the fellows at Biomedical Optical Technologies Lab. Thank you for validating my imaging system as human volunteers, also your helpful advice on my project. A special thanks to Dr. Vivian Pera for your guidance on physiological data processing and beyond.

Fifth, I want to thank the collaborators at Fraunhofer CMI on Boston University campus, including Dr. Alexis Sauer-Budge, Timothy Cormier, David Chargin, and Samuel Brookfield. It was my great pleasure working with you for more than three years on wearable optical probe design.

Last but not the least, I would like to thank you my parents (Yanli Sun, Gangjun Teng) for supporting my decisions, and placing your faith in me. Thank you my grandparents (Yuzhen Lou, Xianwu Sun) for your caring. Thank you my wife (Yuting Li) for the unconditional love and endless happiness.

**A WEARABLE NEAR-INFRARED DIFFUSE OPTICAL SYSTEM FOR
MONITORING IN VIVO BREAST TUMOR HEMODYNAMICS
DURING CHEMOTHERAPY INFUSIONS**

FEI TENG

Boston University, College of Engineering, 2018

Major Professor: Darren Roblyer, Ph.D., Assistant Professor of Biomedical Engineering

ABSTRACT

Neoadjuvant chemotherapy (NAC) is increasingly being utilized to reduce tumor burden prior to surgery for breast cancer patients with stage II or higher disease. A pathologic complete response (pCR) to NAC has been correlated with longer 5-year survival and is generally considered as an absence of invasive cancer in the breast and axillary nodes at the time of surgery. Unfortunately, only about 10% of patients achieve pCR during NAC, and it may take months after the first infusion to determine response with methods that rely on anatomic information, such as palpation, mammography, ultrasound, and MRI. Functional imaging technologies such as Positron Emission Tomography, Magnetic Resonance Spectroscopy, and more recently, Diffuse Optical Spectroscopy, have shown promise for earlier predictions of therapy response. However, most of these techniques suffer from high expense, lack of portability, and safety issues related to the use of ionizing radiation or exogenous contrast agents. Furthermore, the repeated patient visits required by these techniques may hamper their clinical adoption for this purpose.

This project aims to develop a new wearable diffuse optical device that can be used to investigate if very early timepoints during a patient's first chemotherapy infusion are predictive of overall response (pCR versus non-pCR) to NAC. These timepoints correspond to an already scheduled patient visit and have so far been unexplored for their prognostic value. The development of this continuous-wave diffuse optical imaging device was conducted in three stages. First, a prototype rigid probe was designed and developed to test key optical and electrical components. Second, a high optode-density flexible probe was design and fabricated which can conform to the curved surface of the human breast. Finally, a control box with miniaturized electronics and high-speed electronics was designed and fabricated to complete a clinic-ready system. This system was then tested in both the laboratory setting and as part of a normal-volunteer clinical study in healthy subjects during a breath hold hemodynamic challenge.

To the best of our knowledge, this is the first imaging device that targets deep breast tissue measurements through a non-invasive and wearable fashion. With this device, real-time monitoring of fast tissue hemodynamics will enable new time-dependent tissue optical biomarkers that have the potential to predict patients' pathologic benefit from neoadjuvant chemotherapy at early timepoints.

TABLE OF CONTENTS

TABLE OF CONTENTS.....	viii
LIST OF TABLES	xiii
LIST OF FIGURES	xiv
LIST OF ABBREVIATIONS.....	xviii
CHAPTER 1. INTRODUCTION	1
CHAPTER 2. BACKGROUND	6
2.1. Introduction	6
2.2. Breast cancer treatment	6
2.3. Breast tissue composition as measured with diffuse optical technologies.....	8
2.4. Breast tissue optical properties.....	9
2.4.1 Breast tissue absorption	9
2.4.2 Breast tissue scattering	11
2.4.3 The Modified Beer-Lambert law	12
2.5. Light propagation in diffusive media	14
2.5.1 Transport theory	14
2.5.2 Diffusion equation	15
2.5.3 Analytical solution of diffusion equation for CW diffuse optical imaging.....	16
2.5.4 Numerical solutions to the diffusion equation.....	18
2.6. Diffuse optical tomography.....	19
2.6.1 Levenberg-Marquardt (LM) minimization	19
2.6.2 Tikhonov regularization minimization	20

2.7. CW diffuse optical spectroscopic imaging instrumentation	21
2.7.1 Light sources.....	22
2.7.2 Light detectors	24
2.7.3 Electronic switches and multiplexers	26
2.8. Feasibility testing and prototype development of a CW wearable probe.	31
2.8.1 Selection of optical transducers	32
2.8.2 Validation of LED - photodiode pairs	34
CHAPTER 3. GENERATION II CW DIFFUSE OPTICAL SPECTROSCOPIC	
IMAGING SYSTEM	38
3.1 Introduction	39
3.2 Instrument Design	42
3.3 Instrument Performance	45
3.3.1 Signal to Noise Ratio (SNR), Dynamic Range, and System Crosstalk.....	45
3.3.2 System Drift.....	47
3.3.3 Thermal Stability	48
3.3.4 Probe Accuracy.....	50
3.4 <i>In vivo</i> Measurements.....	53
3.4.1 Cuff Occlusion Test.....	53
3.4.2 Normal Volunteer Test	54
3.5 Discussion	56
3.6 Disclosures	58
3.7 Acknowledgements	58

CHAPTER 4. GENERATION III CW DIFFUSE OPTICAL SPECTROSCOPIC

IMAGING SYSTEM	59
4.1 Introduction	59
4.2 Methods	62
4.2.1 Wavelength selection.....	63
4.2.2 Optode Topology	63
4.2.3 Printed circuit board (PCB) design.....	66
4.2.4 Biocompatible probe housing	67
4.2.5 System characterization	68
4.2.6 Channel phantom for simulated breath hold tumor hemodynamics	69
4.2.7 Normal volunteer breath hold study	71
4.2.8 Rise time and fall time calculations during breath hold	71
4.2.9 Effect of system acquisition speed on the accuracy and precision of fall time calculations	72
4.2.10 Tomographic reconstructions	73
4.3 Results	75
4.3.1 Wavelength selection.....	75
4.3.2 Optode geometry validation	76
4.3.3 System performance	77
4.3.4 Channel phantom results	79
4.3.5 Fall time analysis	80
4.3.6 Normal volunteer results	82

4.4 Discussion	84
CHAPTER 5. SUMMARY AND FUTURE DIRECTIONS	87
5.1 SUMMARY	87
5.2 Future directions.....	88
APPENDIX	91
1. Gen2 – Wearable Electronics Design.....	91
1.1 Schematic capture	91
1.2 PCB stack-up	92
1.3 PCB layout (Top layer).....	92
1.4 PCB layout (Bottom layer)	93
1.5 Contributions	93
2. Gen3 – Wearable Electronics Design.....	94
2.1 Schematic capture	94
2.2 PCB stack-up	98
2.3 PCB layout (Rigid top layer)	99
2.3 PCB layout (Flexible bottom layer).....	100
2.5 Contributions	100
3. Portable Electronic Enclosure Design.....	101
3.1 Overview	101
3.1 Front view with dimensions (inch)	102
3.2 Bottom view with dimensions (inch).....	102
3.3 Back view with dimensions (inch)	103

3.4 Side view with dimensions (inch)	103
3.5 Contributions	104
4. Blood Liquid Phantom Recipe	104
BIBLIOGRAPHY	106
VITA	118

LIST OF TABLES

Table 2. 1 Hemoglobin composition in healthy female breast tissue	8
Table 4. 1 System characteristics of high density wearable imaging system	79

LIST OF FIGURES

Figure 2. 1 Premenopausal breast tissue optical absorption in near infrared.....	10
Figure 2. 2 Normalized electromagnetic field distribution of Mie scattering to the incident light at 750 nm by a one-micron spherical particle. The refractive index of sphere is 1.5, while the refractive index of medium is 1.33. Data adapted from online calculation tool: https://omlc.org/calc/mie_calc.html	12
Figure 2. 3 (a) Fluence rate distribution in semi-infinite homogeneous diffusive media ($\mu_a = 0.01/\text{mm}$, $\mu_s' = 1/\text{mm}$) generated by incident pencil beam. (b) Sensitivity function of optical signal at detector position D, with a source-detector separation of 30 mm.	17
Figure 2. 4 Iterative solution searching constrained by fluence rate difference also regularization term. Adapted from Wikipedia	21
Figure 2. 5 Format of optical signals in a CW measurement.....	21
Figure 2. 6 Schematics of a planar diffused silicon photodiode. Adapted from technical notes from OSI Optoelectronics.....	25
Figure 2. 7 Instrument diagram of a broadband optical imaging system. Adapted from (Anderson et al. 2015).....	28
Figure 2. 8 Instrument diagram of a CW tomographic imaging system. Adapted from (Flexman et al. 2011).	29
Figure 2. 9 System diagram and optical probe layout of a CW/FD diffuse optical imaging system design. Adapted from (Cerussi et al. 2006)	30
Figure 2. 10 Condition number of the matrix of extinction coefficients	33

Figure 2. 11 Responsivity of Si sensing module.....	34
Figure 2. 12 Optical probe of first generation diffuse optical imaging system	35
Figure 2. 13 Diagram of the rigid probe testing platform. Green shown the rigid PCB containing 12 LEDs and one photodiode.....	36
Figure 2. 14 Validation of single source and detector module with respect to different separations and forward current. Left: Measurements at 850 nm. Right: Measurements at 750 nm.	37
Figure 3. 1 (a) Flexible PCB and optical components. (b) Top and (c) bottom view of the wearable probe. (d) Flexibility of the probe under gentle pressure.	43
Figure 3. 2 Schematic view of CW diffuse optical imaging system. Solid line: electrical signal. Red arrow: optical signal.....	45
Figure 3. 3 System drift test. Results are shown for (a) the 750 nm and (b) 850 nm optical channels. An average drift of 0.18% or less was observed over the 90 minute test. ..	47
Figure 3. 4 System thermal response to local probe temperature changes. The red solid line corresponds to the local temperature measured at the probe, while the black solid line corresponds to the normalized changes in detector voltage levels. The shaded area indicates the standard derivation calculated from the optodes that share the same wavelength. The red dashed lines show the upper and lower bound of normal physiological temperature of human skin.(Olesen, 1982)	48
Figure 3. 5 Probe results compared to a dissolved oxygen sensor for (a) oxygen saturation and (b) chromophore concentration changes measurements taken from a blood- intralipid phantom during phantom deoxygenation.	50

Figure 3. 6 (a) The probe is secured to the subject's skin using IV tape during cuff occlusion measurements. (b) and (c) Hemodynamic response at forearm during cuff occlusion test.....	53
Figure 3. 7 Hemodynamic fluctuations of healthy female breast tissue at resting state. (a) Oxyhemoglobin (HbO ₂) and deoxyhemoglobin (HHb), (b) total hemoglobin (THb).	56
Figure 4. 1 Optode geometries. Left: 12-pointed star. Middle: Rectangular geometry. Right: Central rectangular geometry.....	64
Figure 4. 2 Simulation geometry utilized for optode configuration comparisons. The inclusion mimics a 35 mm diameter breast tumor embedded in healthy breast tissue.	65
Figure 4. 3 (a) Bottom and (b) top view of rigid-flex PCB. (c) Top and (d) bottom view of the potted wearable probe.	67
Figure 4. 4 Wearable probe attached to the curved surface of human bust model.	68
Figure 4. 5 (a) Channel phantom geometry. (b) Unfilled and (c) filled channel phantom.	70
Figure 4. 6 Condition numbers associated with wavelength pair selections. The dashed isoline indicates 100.5. The condition number corresponding to 750 nm and 850 nm is shown with the red dot markers.	75
Figure 4. 7 Tomographic reconstruction results from various simulated chromophore perturbations in an embedded inclusion (tumor). Simulation ground truth is indicated on the y-axes and reconstructed values are indicated on the x-axis. (a) Reconstructed	

changes in HbO ₂ and HHb for perturbations in HHb. (b) Reconstructed changes in HbO ₂ and HHb for perturbations in HbO ₂ .	77
Figure 4. 8 Signal to noise for probe source-detector separations.	78
Figure 4. 9 $\Delta\mu_a$ reconstructions using the Rytov approximation. Changes in μ_a are shown in the X-Z plane through the center of the channel. The color bar and isolines indicate the % of target $\Delta\mu_a$ reconstructed. The same regularization parameter, $\alpha = 1$, was used for all three reconstructions.	80
Figure 4. 10 HHb fall time extraction accuracy and precision with respect to probe acquisition speeds.	81
Figure 4. 11 ROC curve analysis for differentiating benign and malignant tissue types based on fall times in a simulated system as acquisition speeds are reduced from 1 Hz to 0.1 Hz.	82
Figure 4. 12 HHb concentration changes in healthy breast tissue during breath hold challenge. (a) Results from the wearable optical probe at Biomedical Optical Technologies Lab at Boston University, (b) results adapted from Flexman's study at Columbia University	84
Figure 5. 1 MPU-9250 QFN application schematic for I ² C operation	90

LIST OF ABBREVIATIONS

CAD	Computer-aided design
CW	Continuous wave
DOSI	Diffuse optical spectroscopic imaging
DOT	Diffuse optical tomography
DPF	Differential pathlength factor
FD	Frequency domain
FEM	Finite element method
HbO ₂	Oxyhemoglobin
HHb	Deoxyhemoglobin
LABC	Locally advanced breast cancer
LED	Light-emitting diode
MBLL	Modified Beer-Lambert Law
NAC	Neoadjuvant chemotherapy
NR	No response
PCB	Printed circuit board
pCR	Pathologic complete response
PD	Photodiode
PR	Partial response
StO ₂	Tissue oxygen saturation
THb	Total hemoglobin
SNR	Signal to noise ratio
μ_a	Absorption coefficient
μ'_s	Reduced scattering coefficient
Φ	Fluence rate
λ	Regularization parameter

CHAPTER 1. INTRODUCTION

Locally advanced breast cancer (LABC) are breast tumors that are generally large (>2 cm), may have a direct extension to the skin or chest wall, or present with regional cancer metastasis to lymph or mammary nodes (Garg and Prakash 2015). LABC presents at least three substantial challenges to clinical treatment. First, the 5 year overall survival rate for LABC patients can be as low as 76% even after a combination of surgery, radiotherapy and chemotherapy (SEER Cancer Statistics Review 2018). Second, with traditional treatment procedures most subjects have to endure mastectomy, which aggressively removes the entire affected breast and axillary lymph nodes (Steligo 2017). Third, some primary breast tumors may not be resectable as the cancer invades the skin or chest wall.

To overcome these challenges, preoperative chemotherapy, also called neoadjuvant chemotherapy (NAC), was introduced to shrink tumor size before surgery, and it has been increasingly adopted as the default treatment plan for LABC patients (Ragaz, Band, and Goldie 2012). The pathological outcome to NAC, proposed by the American Joint Committee on Cancer (AJCC) 8th edition, is staged as complete response (pCR): absence of invasive carcinoma in the breast and node, partial response (PR): downgrade in either or both tumor (T) or node (N) stage, and no response (NR): stable or increase in either or both T or N stage (AJCC 2017). Guided by this criteria, about 10% of LABC patients are expected to achieve pCR, 60% PR, and about 20 to 30% of this population are NR even after weeks to months of treatment, and some patients may even develop progressive response (Kuerer et al. 2000; Esserman 2004; Keam et al. 2013).

Therefore, predicting patients' response to chemotherapy at earlier timepoints based on tissue anatomic or functional information could be valuable in optimizing the chemotherapy treatment plan and maximizing outcomes, especially for the subjects who fail to receive benefits from NAC.

Several traditional clinical imaging methods have been explored for breast cancer monitoring during the course of NAC. For example, positron emission tomography/computed tomography (PET/CT) using fluorine-18-fluorodeoxyglucose (18F-FDG) has been reported to predict patients' response with about 80 - 90% accuracy (Schelling et al. 2000; Chen et al. 2004; Biersack, Bender, and Palmedo 2008). Magnetic resonance imaging (MRI) and functional MRI have both demonstrated prognostic value in cancer monitoring (Esserman et al. 1999; Heldahl et al. 2011; Rigter et al. 2013; Dave et al. 2017). Specifically, contrast-enhanced magnetic resonance imaging (CE-MRI) has shown superior performance in the specificity of prediction results compared to diffusion-weighted magnetic resonance imaging (DW-MRI), while DW-MRI has an edge in sensitivity (Gu et al. 2017). Ultrasonography and mammography have both been applied for NAC monitoring as well, but their prognostic accuracy is not comparable to the imaging modalities mentioned above (Tadayyon et al. 2016; Gu et al. 2017; Nam et al. 2017).

Unfortunately, these clinical imaging modalities are accompanied by high expense, lack of portability, and safety issues due to the use of ionizing radiation or exogenous contrast agents. In contrast, diffuse optical imaging, which utilizes near infrared light and portable imaging platforms, avoids these limitations. NAC monitoring

with diffuse optical imaging thus can be far more adaptive to patients' scheduled chemotherapy infusions. Among the variants of diffuse optical imaging, both continuous-wave (CW) and temporally-modulated (i.e. frequency-domain (FD)) are popular in academic research exploring chemotherapy response. For example, researchers at Dartmouth College developed a FD diffuse optical imaging system that employs radio-frequency intensity modulated near-infrared (NIR) light to quantitatively image both the scattering and absorption coefficients of tissue (Pogue et al. 1997). The Beckman Laser Institute at University of California, Irvine and the University of Pennsylvania both developed hybrid FD/CW clinical prototypes for breast imaging (Shah et al. 2001a; Culver et al. 2003). Commercial systems for diffuse optical breast imaging have also been developed and approved (Intes et al. 2004). Previous studies with these instruments have demonstrate that the pathological response of LABC patients to neoadjuvant chemotherapy can often be determined within weeks to months after the start of treatment, and are typically associated with a decrease of hemoglobin concentration and water content, and an increase of lipid concentration (Cerussi et al. 2007; Jiang et al. 2009; Choe and Durduran 2012).

Most recently, the acute response (first hours to days of treatment) to NAC has also been shown to manifest through significant difference between responders and non-responders when monitored with diffuse optical instruments. For example, in a study of 23 LABC subjects, tissue oxyhemoglobin concentration was determined to discriminate the pathological outcome from chemotherapy on the very first day after initial infusion (Roblyer et al. 2011). This study, if further confirmed with a larger sample size, may

indicate that a patient's response to chemotherapy can be confirmed within hours of the start of treatment, which could substantially minimize treatment burden and ineffective chemotherapy.

This work aimed to address several unmet needs of existing breast cancer diffuse optical monitoring devices. First, previous designs typically deliver light to and from the patient using optical fibers. This type of design is often bulky, heavy, and fragile. Second, the optical probe or patient/device interface is typically rigid and poorly conforms to the natural shape of human tissue. This is limiting as it may be uncomfortable for the patient, especially during extended measurements. Typical solutions include adjusting the position of individual fiber tips (Flexman et al. 2011) or adjusting the distance or the angle between compressing plates (Ge et al. 2008; Choe et al. 2009; Anderson et al. 2015). Third, for optical probes with limited number of light sources and detectors, a 2D mapping of tissue properties may require the probe head to be sequentially scanned over gridded positions on the skin (Roblyer et al. 2011). Therefore, data acquisition for each iteration may take 10s of minutes, and poor temporal and spatial resolution from this imaging protocol excludes the possibility of real time monitoring of tissue hemodynamics.

This thesis describes three iterations of breast tissue imaging systems that progressively address the limitations described above. The overall goal of this work was to develop a wearable probe that could perform breast cancer therapy monitoring at high spatial and temporal resolution. The final product of this work is a clinical-ready high-optode density and flexible wearable probe and electronics control box. This imaging

probe has been validated through both *in vitro* and *in vivo* studies.

This thesis is organized into five chapters and one appendix. Chapter 2 describes the background and motivation of this work, including breast cancer and treatment, diffuse optics theory and its applications for breast tissue imaging, and CW diffuse optical spectroscopic imaging system instrumentation. It also includes a description of the preliminary system designs that led to the development of the wearable tissue imaging device. Chapter 3 through 4 describe the system design, characterization, and verification and validation of two iterations of the wearable imaging device. Chapter 5 is a summary of this work and future directions. The Appendix section includes the electronic and mechanical computer-aided design (CAD) of the imaging systems and the recipes for tissue simulating optical phantoms used in this work.

CHAPTER 2. BACKGROUND

2.1. Introduction

The relevant background for this work includes the fundamentals of breast cancer treatment, diffuse optical spectroscopic imaging, algorithms for solving diffuse optical inversion problems, and the electrical engineering theory relevant to diffuse optical imaging system design.

2.2. Breast cancer treatment

The earliest recorded case of breast cancer comes from the 1600 BC Edwin Smith Papyrus in ancient Egypt (American Cancer Society 2018). For thousands of years, people have suggested a variety of causes to account for the development of breast cancer. The ancient Greeks described breast cancer as a humoral disease, and this belief lasted until the 17th century. By then physicians challenged the humoral theory of cancer, and attributed the cause of breast cancer to patients' living style. By the 19th century, the hopelessness of not knowing gave rise to a wave of psychological theories, which argued the origin of breast cancer is due to cancerophobia (Brechon 2012). Rigorous investigations into the origins and development of breast cancer were facilitated with the advance of modern medicine, which gave birth to more systemic theories of breast cancer. This included the realization that breast cancer often originates from specific genetic mutations including (but not limited to) mutations in the BRCA1 and BRCA2 genes (Hall et al. 1990; Wooster et al. 1995), the p53 gene (Malkin et al. 1990), the PTEN gene (Li et al. 1997), and the PIK3CA gene (Campbell et al. 2004).

In one sense, cancer can be thought of as a genetic disease, and mutations in key

genes promote abnormal cell growth and proliferation from the milk ducts or the lobules of the female breast. This leads to *Intraductal Carcinoma* or *Lobular Carcinoma*. The former accounts for 85% of breast cancer cases (Welsh 2013). Though less prevalent, several other types of breast cancer may appear as *Tubular Carcinoma*, *Mucinous Carcinoma*, and *Papillary Carcinoma*. The stage of breast cancer is typically described according to the TNM system, and are ranked from stage 0 (carcinoma *in situ*) to 4 (metastatic breast cancer). The TNM stages for LABC are 2 or higher. Breast cancer is widespread across the globe. According to the cancer statistics from National Cancer Institute, in the U.S., about 1 in 8 women will develop invasive breast cancer over the course of her lifetime (National Cancer Institute 2018). In 2018, breast cancer is estimated to include 15.3% of new cancer cases, and contributes to 6.7% of all cancer deaths (National Cancer Institute 2018).

Clinical treatment of breast cancer largely falls within two categories. Local treatments aim to remove the malignant lesions within the breast and the affected lymph nodes. Examples include surgery and radiation therapy. Systemic treatments, including chemotherapy, hormone therapy, and targeted therapy, are administered with the goal of eliminating cancer cells throughout the body. Due to the complexity of breast cancer, a treatment plan is tailored to the biology of the tumor, the cancer stage, and the physical condition of the subject whenever possible. Most patients, however, will experience a combination of surgery, local therapy, and systemic therapy.

2.3. Breast tissue composition as measured with diffuse optical technologies.

Diffuse optical technologies utilize near-infrared light to extract concentrations of chromophores, or light absorbing species in tissue. This typically includes oxy and deoxyhemoglobin, water, and lipids (Jacques 2013). Prior studies have measured the composition of healthy and cancerous breast tissue using diffuse optical technologies, and a summary of these results are included here.

The composition of human breast tissue is strongly correlated with the menopausal status of a female subject (Cerussi et al. 2001; Shah et al. 2004). On average, the lipid content increases from approximately 30% to 68%, while water content decreases from 45% to 10% before and after menopause (Cerussi et al. 2001). Hemoglobin has been shown to decrease from more than 40 μM to less than 15 μM due to absence of the menstrual cycle (Cerussi et al. 2001). A summary of the results of several relevant studies that measured total hemoglobin (THb) and oxygen saturation (StO₂) are shown in Table 2.1.

Study	Sample size	Menopausal status	THb (μM)	StO ₂ (%)
(Cerussi et al. 2001)	15	Pre	40.5	76.3
(Shah et al. 2004)	18	Pre	26.5	74
(Cerussi et al. 2001)	6	Post	14.6	91.9
(Shah et al. 2004)	13	Post	15.1	75
(Durduran et al. 2002)	52	N/A ¹	34	68

Table 2. 1 Hemoglobin composition in healthy female breast tissue

1: The age distribution of subjects is 32±12 years, which indicate the majority are premenopausal. For details, see Figure 5 of the reference.

The dynamic changes of THb and StO₂ with respect to time and space are the focus of this study. Changes in THb may be potentially linked to vessel dilation or contraction caused by partial pressure variations of carbon dioxide in the blood, or an imbalance of flow rate between oxygenated and deoxygenated blood (Cipolla 2009). StO₂ is calculated as the percentage of oxygenated hemoglobin (HbO₂) concentration to THb concentration, which serves as an indirect biomarker of tissue metabolic rate.

2.4. Breast tissue optical properties

Biological tissue, if examined from the perspective of light-tissue interactions, is well described by its optical absorption μ_a and optical scattering μ_s coefficients, which indicate the average distance that a photon is likely to propagate before undergoing either an absorption or scattering event. Tissue absorption occurs as the incoming photons transfer optical energy to electrons, which pump them up into higher energy states; while the scattering events are the result of gradients and discontinuities in the index of refraction at the spatial scale from nanometers to micrometers. At NIR wavelengths, tissue scattering is typically one or two orders greater than absorption strength, and biological tissue is typically described as an optically diffuse media (Jacques 2013).

2.4.1 Breast tissue absorption

Figure 2.1 shows the weighted absorption contribution from the major absorbers in pre-menopause breast tissue at wavelengths between 600 nm to 900 nm. This plot was produced based on the breast composition properties described in section 2.3. The concentration of oxyhemoglobin (HbO₂) is 19.6 μM , the concentration of deoxyhemoglobin (HHb) is 6.9 μM , and the tissue is assumed to contain 34.5% water,

and 41% fat. The extinction coefficient spectrum of water is adapted from (Hale and Querry 1973), while the extinction coefficient spectrum of hemoglobin is adapted from omlc.org/ (Prahl 1998). Hemoglobin dominates the absorption of breast tissue for the majority of the spectrum.

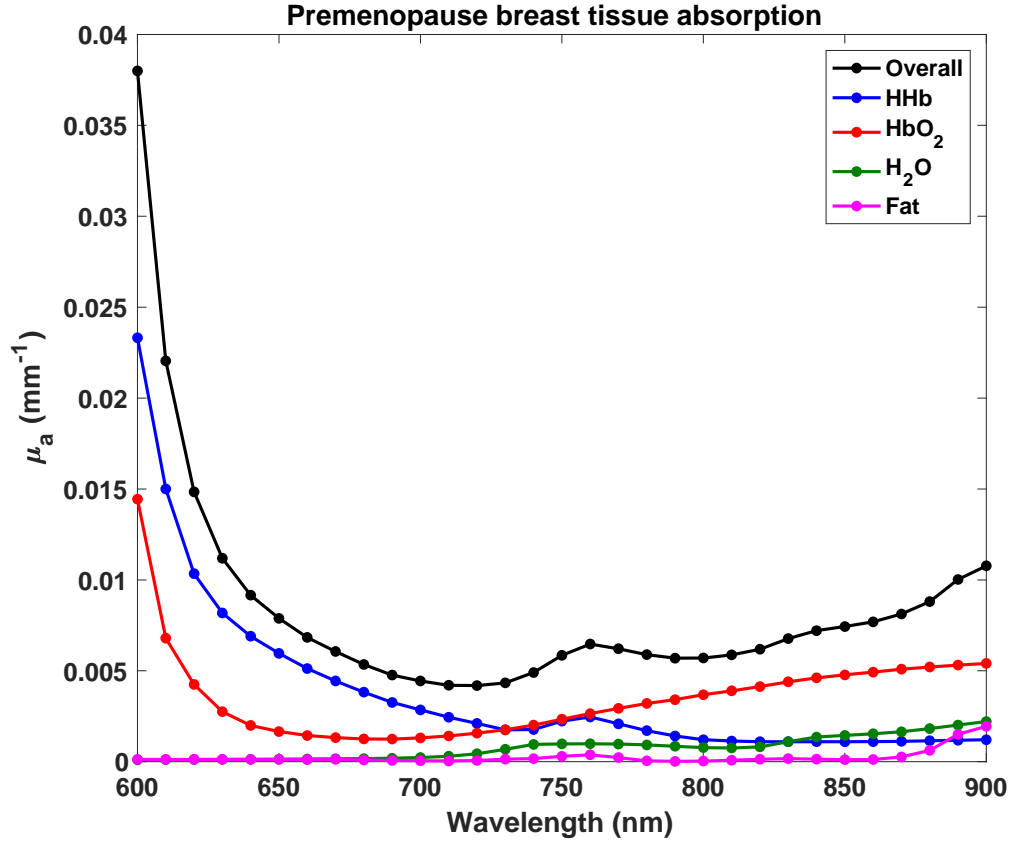


Figure 2. 1 Premenopausal breast tissue optical absorption in near infrared.

The chromophore composition of breast tissue and the tissue optical absorption are linked through Beer's Law, which describes the absorption coefficient $\mu_a(\lambda)$ as the sum of individual absorbers' contribution,

$$\mu_a(\lambda) = 2.303 \cdot \sum_{i=1}^N \varepsilon_i(\lambda) \cdot C_i \quad (1)$$

where ε and C are the molar extinction coefficient and the concentration of a tissue chromophore, respectively.

2.4.2 Breast tissue scattering

The scattering of photons by biological tissue at NIR wavelengths are predominantly described by Mie scattering due to the fact that the size of organelles, membranes and other intracellular structures generally are less than one order difference from the illumination wavelength (Bigio and Fantini 2016). The structural components of the extracellular matrix, including collagen and elastin, generally scatter incident photons according to Rayleigh scattering. The polar plot in Figure 2.2 represents the probability of photon distribution from Mie scattering events, with unpolarized light and a one-micron isotropic scattering particle. The scattered electromagnetic field is highly anisotropic. It indicates a photon is more likely to be forward scattered than back scattered, with the peak probability along the incident direction. This field distribution can be quantitatively summarized by an anisotropy factor g ,

$$g \equiv \langle \cos\theta \rangle = \int_{4\pi} \cos\theta \cdot p(\theta) d\Omega \quad (2)$$

where θ is the polar angle between the incident and scattered photon, p is the scattering phase function, Ω is the solid angle of the scattered photon. For most biological tissue, g is typically around 0.9 (Jacques 2013). By introducing g factor, the scattering mean free path $1/\mu_s$ can be extended to $1/((1 - g)\mu_s)$, which represents the mean distance after which a photon's direction becomes random. The term $(1 - g)\mu_s$ can be expressed as μ'_s , which is called the reduced scattering coefficient.

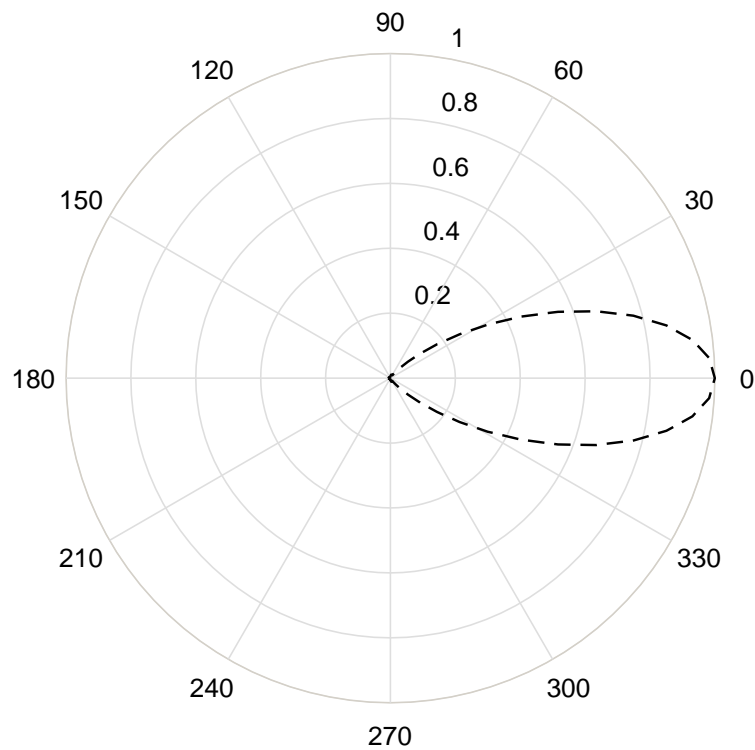


Figure 2. 2 Normalized electromagnetic field distribution of Mie scattering to the incident light at 750 nm by a one-micron spherical particle. The refractive index of sphere is 1.5, while the refractive index of medium is 1.33. Data adapted from online calculation tool: https://omlc.org/calc/mie_calc.html

2.4.3 The Modified Beer-Lambert law

A simple equation for calculating tissue functional and the optical properties from diffuse optical measurement is the modified Beer-Lambert law (MBLL). In 1988, Delpy and his colleagues developed this concept, and validated it through Monte Carlo simulation and experimental time-domain diffuse optical imaging (Delpy et al. 1988). A central idea of this method is to account for the fact that both absorption and scattering contribute to photon pathlength. It accounts for this by multiplying the optical density

term with a differential pathlength factor (*DPF*). The *DPF* can be expressed as a function of tissue optical properties and light emitter and detector separation d (Scholkmann and Wolf 2013):

$$DPF(\lambda) = \frac{1}{2} \left(\frac{3\mu'_s(\lambda)}{\mu_a(\lambda)} \right)^{1/2} \left[1 - \frac{1}{(1+d \cdot (3\mu'_s(\lambda) \cdot \mu_a(\lambda))^{1/2})} \right] \quad (3)$$

This expression indicates that DPF increases with greater μ'_s , and decreases with greater μ_a . The MBLL can be written as:

$$I(\lambda) = I_0(\lambda) e^{-\mu_a(\lambda) \cdot d \cdot DPF(\lambda) + G(\lambda)} \quad (4)$$

where $G(\lambda)$ is a wavelength, medium, and geometry dependent constant. I_0 and I are optical intensity measured at light emitter and detector, respectively. For repeated tissue measurements with an unchanging imaging setup, the $G(\lambda)$ factor can be cancelled out between successive measurements, thus leading to the differential format of MBLL for the $(k + 1)th$ measurement, which is expressed in terms of the change in tissue optical density (OD):

$$\Delta OD = -\log \left(\frac{I(t = k + 1, \lambda)}{I(t = k, \lambda)} \right) = \sum_{i=1}^N \Delta \mu_a^{i,k}(\lambda) \cdot DPF(\lambda) \cdot d \quad (5)$$

The differential MBLL provides a convenient way to compute the changes in tissue absorption using repeated optical physiological monitoring, but it is a simplified method that carries assumptions that may be unrealistic in certain circumstances. First, it assumes tissue scattering changes are small compared to changes in absorption. This condition is likely to be well satisfied only during short timeframe tissue hemodynamic monitoring. Second, it assumes that the underlying tissue is optically homogeneous, and changes within the tissue are homogeneous from one measurement to the next. Therefore,

when utilizing the differential MBLL as a tool for extracting tissue parameters, one should be aware of these assumptions and how they may affect accuracy.

2.5. Light propagation in diffusive media

2.5.1 Transport theory

Photon transport in biological tissue can be described by the Radiative Transfer Equation (RTE) based on conservation of energy within infinitesimal volume $dV(\mathbf{r})$, where \mathbf{r} is a vector pointing from light source to a spatial point of interest. It describes radiance $L(\mathbf{r}, \hat{\Omega}, t)$, defined as the optical power received per unit area, per unit solid angle that is propagating along direction $\hat{\Omega}(\theta, \varphi)$ at time t from differential volume dV . RTE considers changes in radiance due to photon diffusion, photon collision and light sources.

$$\frac{1}{c} \frac{\partial L(\mathbf{r}, \hat{\Omega}, t)}{\partial t} = -\hat{\Omega} \cdot \nabla L(\mathbf{r}, \hat{\Omega}, t) - (\mu_a + \mu_s) L(\mathbf{r}, \hat{\Omega}, t) + \mu_s \int_{4\pi} L(\mathbf{r}, \hat{\Omega}', t) p(\hat{\Omega}', \hat{\Omega}) d\Omega' + q(\mathbf{r}, \hat{\Omega}, t) \quad (6)$$

where $q(\mathbf{r}, \hat{\Omega}, t)$ is light source. The positive terms on the right-hand side of Equation 6 indicates photon accumulation within dV through incoming photon scattering and generation, while the negative terms indicates photon dissipation through outgoing scattering and absorption. The difference between these two processes represent the net changes in photon density.

The transport theory is a rigorous and universally applicable method in describing photon movements in diffusive media, but it does not provide a convenient analytical

expression of radiance, and numerical computation with RTE is generally accessible through Monte Carlo methods (Wang, Jacques, and Zheng 1995).

2.5.2 Diffusion equation

The diffusion equation is the truncated result after the radiance, the source term, and the scattering phase function of the RTE are expanded into a set of basis functions. In the time domain it can be written as

$$\frac{1}{c} \frac{\partial \Phi(\mathbf{r}, t)}{\partial t} + \mu_a \Phi(\mathbf{r}, t) - \nabla [D \nabla \Phi(\mathbf{r}, t)] = q(\mathbf{r}, t) \quad (7)$$

where $D = c_n / [3(\mu'_s + \mu_a)]$ is diffusion coefficient and c_n is the speed of light in diffusive media. $\Phi(\mathbf{r}, t)$ is the fluence rate, which represents the incoming photons per unit area, per unit time from all solid angles.

There are three assumptions required to simplify the RTE into the diffusion equation. First, the reduced scattering coefficient μ'_s is much larger than μ_a ; second, the source emission is isotropic; third, the time for substantial current density change is much longer than the time to traverse one transport mean free path. A detailed derivation of the diffusion equation from RTE can be found in Sections 9.2 to 9.5 in the textbook *Quantitative Biomedical Optics* (Bigio and Fantini 2016). The optical properties of biological tissue at NIR wavelengths can typically satisfy these assumptions after a propagation distance greater than several transport mean free paths (Yoo, Liu, and Alfano 1990). Therefore, the diffusion equation can be used as an important component in methods for analyzing diffuse optical imaging measurements. It should be noted that the observation of fluence rate is measured in the “far field”, which is typically centimeters away from the light source.

2.5.3 Analytical solution of diffusion equation for CW diffuse optical imaging

Given a homogeneous distribution of tissue optical properties measured with a CW light source, the diffusion coefficient in Equation 7 becomes spatially homogeneous, and the fluence rate is time-independent, further simplifying the diffusion equation:

$$\mu_a \Phi(\mathbf{r}) - D \nabla^2 \Phi(\mathbf{r}) = q(\mathbf{r}) \quad (8)$$

For a semi-infinite geometry and Robin boundary condition at the air-tissue interface; the fluence rate evaluated at a point A in tissue can be written as (Bigio and Fantini 2016):

$$\Phi_{S \rightarrow A} = -\frac{3(\mu'_s + \mu_a)}{4\pi} 2z_0 z \left(\mu_{eff} + \frac{1}{r} \right) \frac{e^{-\mu_{eff}|\mathbf{r}|}}{|\mathbf{r}|} \quad (9)$$

where $|\mathbf{r}|$ is the distance between physical source location S and point A , z_0 is the location of the effective source depth from tissue-air interface. $\mu_{eff} = \sqrt{3\mu_a(\mu'_s + \mu_a)}$ is the effective attenuation coefficient. Figure 2.3 (a) shows the fluence rate distribution based on Equation (9), as an incident pencil beam transmits into diffusive media, photon propagation gets randomized, which turns the fluence rate distribution into an isotropic profile along the depth of the photon penetration.

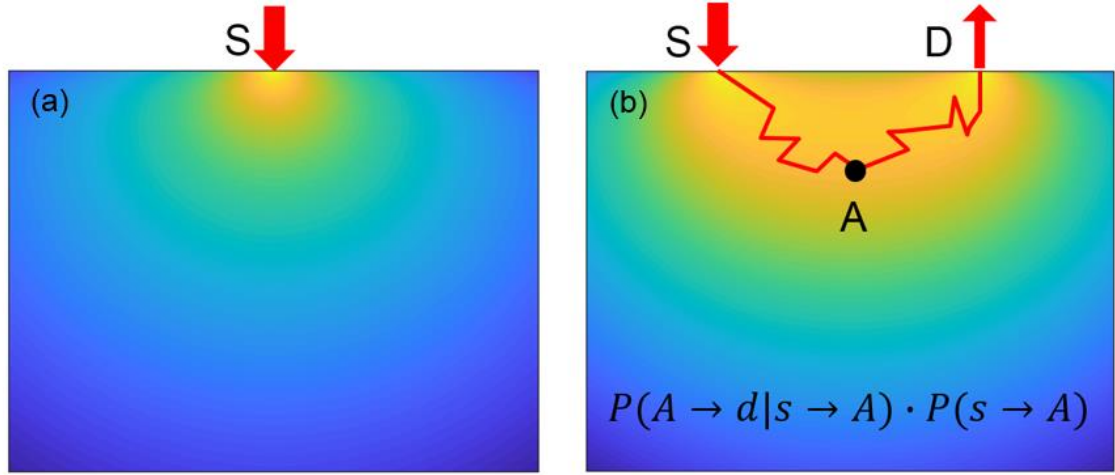


Figure 2.3 (a) Fluence rate distribution in semi-infinite homogeneous diffusive media ($\mu_a = 0.01/\text{mm}$, $\mu'_s = 1/\text{mm}$) generated by incident pencil beam. (b) Sensitivity function of optical signal at detector position D , with a source-detector separation of 30 mm.

For non-invasive deep tissue imaging, one is typically not only interested in the measured fluence rate at the surface, but also the propagation path of the detected photons. The probability for a photon reaching photodetector D via the aforementioned point A is proportional to the sensitivity of detected signal to local optical property perturbation at point A . The sensitivity function thus correlates the actual CW optical signal with optical property changes in diffusive media, which can be constructed by multiplying fluence rate from source S to point A , then to photodetector D . This can be written as (Bigio and Fantini 2016):

$$s(\mathbf{r}) = \frac{\Phi_{S \rightarrow D}(\boldsymbol{\mu}_r + \delta\boldsymbol{\mu}_{r=A}) - \Phi_{S \rightarrow D}(\boldsymbol{\mu}_r)}{\delta\boldsymbol{\mu}_{r=A}} = k \cdot \Phi_{S \rightarrow A} \cdot \Phi_{A \rightarrow D} \quad (10)$$

where k is a spatially independent factor of fluence rate. Figure 2.3 (b) indicates the propagation path of the detected photons traverse a banana-shaped volume in the underlying homogeneous diffusive media. As a rule-of-thumb, the depth of penetration, defined as the FWHM of sensitivity in the plane perpendicular to light source and detector, is generally about or less than half of the source-detector separation. This potentially allows diffuse optical imaging to detect the primary tumors in breast tissue, as well as metastatic lesions embedded up to several centimeters deep in tissue.

2.5.4 Numerical solutions to the diffusion equation

The analytical forms of the fluence rate and sensitivity function assume homogeneous tissue optical properties. For inhomogeneous diffusive media, which is a closer estimate to human breast tissue, numerical tools are required for fluence rate calculations. Relevant methods include the Finite Difference Method, the Finite Volume Method, and Finite Element Method (FEM). FEM is considered as the most popular option due to its ability to account for conservative systems (e.g. heat conduction, fluid dynamics) and non-conservative systems (e.g. light-tissue interactions), and the ability to create adaptive meshes for irregular boundaries. FEM requires the imaging domain to be divided into interconnected elements, where the differential forms of diffusion equation are discretized and evaluated over mesh nodes.

Consider an optical probe with M source-detector pairs, and a FEM mesh with N nodes inside. If only optical absorption changes are considered, the discretized expression of sensitivity function for a CW measurement, also called the Jacobian matrix, can be written in terms of a $M \times N$ matrix:

$$J = \begin{pmatrix} \frac{\partial \Phi_1}{\partial \mu_a^1} & \frac{\partial \Phi_1}{\partial \mu_a^2} & \dots & \frac{\partial \Phi_1}{\partial \mu_a^{N-1}} & \frac{\partial \Phi_1}{\partial \mu_a^N} \\ \frac{\partial \Phi_2}{\partial \mu_a^1} & \frac{\partial \Phi_2}{\partial \mu_a^2} & \dots & \frac{\partial \Phi_2}{\partial \mu_a^{N-1}} & \frac{\partial \Phi_2}{\partial \mu_a^N} \\ \vdots & \vdots & \ddots & \vdots & \vdots \\ \frac{\partial \Phi_{M-1}}{\partial \mu_a^1} & \frac{\partial \Phi_{M-1}}{\partial \mu_a^2} & \dots & \frac{\partial \Phi_{M-1}}{\partial \mu_a^{N-1}} & \frac{\partial \Phi_{M-1}}{\partial \mu_a^N} \\ \frac{\partial \Phi_M}{\partial \mu_a^1} & \frac{\partial \Phi_M}{\partial \mu_a^2} & \dots & \frac{\partial \Phi_M}{\partial \mu_a^{N-1}} & \frac{\partial \Phi_M}{\partial \mu_a^N} \end{pmatrix}$$

The Jacobian matrix can be computed using FEM methods for arbitrary measurement geometries and tissue optical property spatial distributions.

2.6. Diffuse optical tomography

Tomographic reconstruction of tissue optical or functional properties may be considered as the opposite or inverse of the process used to calculate optical fluence rates described in Section 2.5. Searching for the optimal reconstructed tissue properties is mathematically equivalent to solving a least square problem, where the calculated fluence rate Φ_C is the best approximation of the measured data Φ_M . This can be expressed as:

$$\boldsymbol{\mu} = \underset{\boldsymbol{\mu}}{\operatorname{argmin}}\{\|\Phi_M - \Phi_C\|^2\} \quad (11)$$

2.6.1 Levenberg-Marquardt (LM) minimization

Without spatial prior estimates of tissue optical properties, minimization to the object function in Equation 11 can be achieved through the LM algorithm, which iteratively reduces the cost function. To reach a local minimal within the solution space, the first order derivative of object function is set zero, which leads to the update equation for the i th iteration of minimization:

$$[J^T J + \lambda \cdot \mathbf{diag}(J^T J)] \Delta \boldsymbol{\mu}_i = J^T \delta_{i-1} \quad (12)$$

where λ is a regularization parameter that monotonically decrease with each iteration. Since the square matrix $J^T J$ is ill-conditioned, Kenneth Levenberg and Donald Marquardt added and modified a diagonal matrix term respectively, so as to stabilize and optimize solution searching (Levenberg 1944; Marquardt 1963).

The inverse problem described above is ill-posed due to the vast number of unknown tissue optical properties (10K~10M nodes for 3D mesh) that need to be determined by at most hundreds of independent measured variables. A minimized object function is typically not enough to reach accurate reconstruction results that represents the actual tissue optical or functional properties, and the reconstructed tomographic results and rate of convergence are largely dependent on the initial guess of tissue properties (Madsen, Nielsen, and Tingleff 2004).

2.6.2 Tikhonov regularization minimization

To overcome the concerns raised in Section 2.6.1, in many cases, tissue spatial priori information are considered and utilized in the object function:

$$\boldsymbol{\mu} = \underset{\boldsymbol{\mu}}{\operatorname{argmin}} \left\{ \|\Phi_M - \Phi_C(\boldsymbol{\mu}, \mathbf{r}_d)\|^2 + \lambda \cdot \|\mathbf{L}(\boldsymbol{\mu} - \boldsymbol{\mu}_{prior})\|^2 \right\} \quad (13)$$

where \mathbf{L} is a regularization matrix and λ serves as a regularization parameter that stays constant with each iteration. Figure 2.4 shows the iterative solution searching process in a 2D solution space. The value of object function is not only constrained by the sum of squared fluence rate residuals, which is represented by the isolines, but also limited by tissue optical property residuals, which is represented by the size of the shaded circle.

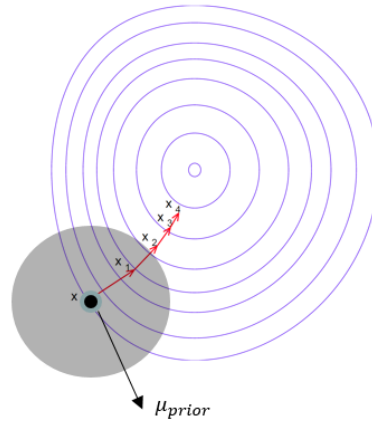


Figure 2. 4 Iterative solution searching constrained by fluence rate difference also regularization term. Adapted from Wikipedia

2.7. CW diffuse optical spectroscopic imaging instrumentation

CW diffuse optical spectroscopic imaging (DOSI) is the simplest and most economic form of diffuse optical imaging. As shown in Figure 2.5, the optical signals for CW measurements are generally DC signal or modulated at a low (i.e., KHz) modulation frequency.

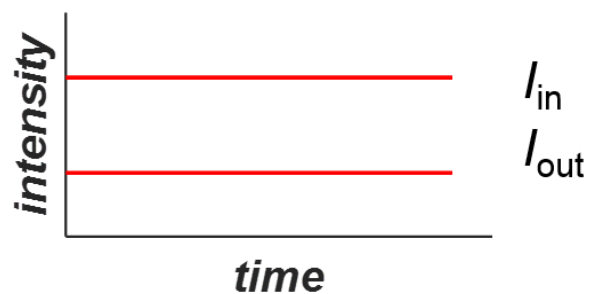


Figure 2. 5 Format of optical signals in a CW measurement

The simplicity of this technique promotes its wide applications in the domain of consumer devices, such as fitness trackers, as well as in medical devices including pulse oximeters. Applications of CW diffuse optical tissue imaging typically assumes that the

tissue scattering properties are constant over seconds to minutes timescales, due to the generally stable distribution of intercellular and extracellular particle density. For the past several decades, CW DOSI has emerged as a new technology for breast cancer monitoring. This section will review the components of CW DOSI instruments and then describe several representative instrument designs that have been utilized in prior clinical studies.

2.7.1 Light sources

White light sources, such as halogen lamps, are commonly used for CW DOSI because of the importance of using multiple wavelength to extract chromophore concentrations (Bevilacqua et al. 2000; Cerussi et al. 2006). The spectrum of halogen lamps, coming from the black-body radiation of hot tungsten filament, generally extends from the ultraviolet (UV), visible, near-infrared, and infrared wavelengths. Light emitted from white light sources are typically collected and delivered through optical fibers, while the optical spectrum for CW imaging can be continuous or selectively filtered into discrete wavelengths.

Light emitting diodes (LED) are also popular light source for CW DOSI instruments (Bozkurt et al. 2005; Zhang, Yan, and Strangman 2011; Eggebrecht et al. 2014; Yuan et al. 2014; Teng et al. 2017). LED emission spectra are largely determined by the bandgap between the conduction and valence bands of the semiconductor substrate. For LEDs with peak emission at NIR wavelengths, the substrate of PN junction is typically Aluminum Gallium Arsenide, Gallium Arsenide, or Gallium Arsenide Phosphide (Dakin and Brown 2006).

Applications of LEDs for tissue measurement have both pros and cons. On the negative side:

1. LED light sources are generally not friendly for fiber coupling due to their Lambertian emission profiles.
2. For tissue contact measurement, LED light source poorly approximate a pencil beam, which is often an assumption in the simulation of diffuse optical imaging (Farrell, Patterson, and Wilson 1992).
3. Due to temperature sensitivity of the underlying semiconductor substrate, the central wavelength of LEDs is subject to change due to package overheating (Dakin and Brown 2006).

However, on the positive side:

1. Compared to white light sources, LEDs are relatively efficient in energy conversion from electricity to light.
2. The smallest standardized LED size can be on the order of tens of microns, which can be fit into miniaturized consumer and clinical wearable formats.
3. Some LED packages support total internal reflection lenses, which substantially decrease the half angle of light emission from around 50 degrees to less than 15, which turns the incident light from LEDs into a closer estimate to pencil beam.

Laser diodes are also widely used in CW diffuse optical imaging designs

(Tamura, Hoshi, and Okada 1997; Macnab and Stothers 2008; Flexman et al. 2011).

Compared to the previous two classes of light sources, the emitted light from laser diodes is coherent, with much smaller divergence angles, and the spectral width is typically at

the level of one tenth of nanometer (Daly 1984). The default approach for light delivery from laser diodes is through optical fibers, which complicates their potential use in wearable optical devices for the human body.

Among these three light source options, the LEDs were used for the wearable probe presented in this work, due to their inherent and unparalleled advantage in package size for tissue contact measurement.

2.7.2 Light detectors

The most common photodetectors used in CW DOSI instrumentation are photomultiplier tubes (PMT), photodiodes (PD) and avalanche photodiodes (APD).

PMTs are a type of highly sensitive photo-detection devices that accelerate photoelectrons through an electric field, and amplify the photocurrent through a series of cascaded dynodes. Though PMTs have a gain between 10^3 to 10^6 , their dynamic range is limited to approximately 30 dB. This makes PMT an ideal photodetector for low light detection, but less desirable for optical detection of tissue hemodynamics as changes in hemoglobin concentration may strongly alter light attenuation during a measurement. Also, the bulky size of PMT sensing module and its high voltage power supply are not feasible for wearable physiological sensing.

PDs operate by absorption of photons or charged particles and generate a flow of current in an external circuit proportional to the incident power. As a type of basic structure for PDs, the P-N junction is formed by diffusing either a P-type impurity, such as Boron, into an N-type bulk silicon wafer, or an N-type impurity, such as Phosphorous,

into a P-type bulk silicon wafer. Figure 2.6 shows the schematics of a planar diffused silicon photodiode.

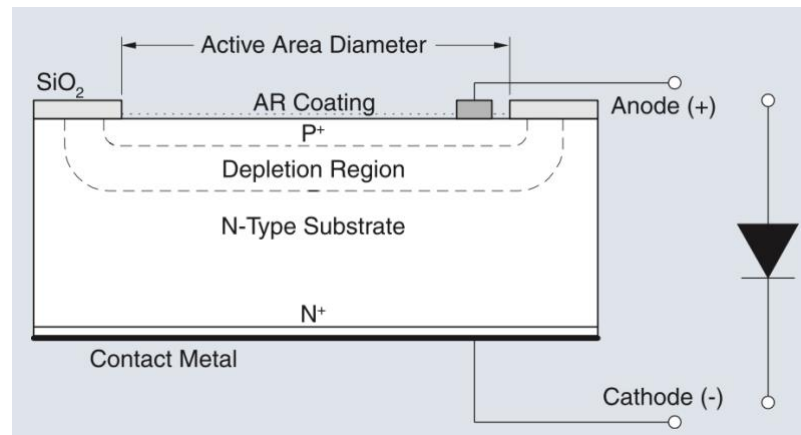


Figure 2. 6 Schematics of a planar diffused silicon photodiode. Adapted from technical notes from OSI Optoelectronics.

There are several key aspects of PDs to consider in optical sensor design. First, the spectral sensitivity of the substrate. Silicon is typically chosen as the substrate of PDs for NIR light detection due to its spectral sensitivity from approximately 300 to 1100 nm. Second, the responsivity of a PD is a measure of the photocurrent generated per unit detected optical power, which is a function of quantum efficiency, incident wavelength, and the detector gain. Therefore, it is desirable if the PD exhibits high responsivity to the wavelengths of light source. Third, noise-equivalent power (NEP), defined as the minimum input optical power that generate a photocurrent equal to the noise current in a 1 Hertz bandwidth. This determines, in part, the sensitivity of PD to low light detection. Fourth, the impedance of PD. This can be affected by the dimension, package, and operating mode of the PD. This frequency-dependent parameter determines the rise and fall time of the device, which limits the frequency of light it can measure. Fifth, noise. A

PD may suffer from statistical fluctuation in both the photocurrent and the dark current, which contributes to shot noise. This is the dominate noise source when a PD is biased with an external voltage (Kingston 1995). Another noise source is due to the thermal generation of carriers, which is thus named as thermal noise. Sixth, operating mode. A PD can be operated in photoconductive mode or photovoltaic mode, depending on the implement of a bias voltage. For light collection in tissue measurement, photoconductive mode is much more common due to shorter temporal response and better linearity, although stronger dark current and noise current can be expected.

An APD is a high-speed, highly-sensitive photodiode with an internal gain on the order of 100. The electron-hole pairs are generated from exposure to light with higher photon energy than the band gap energy. A reverse voltage applied to the PN junction of the APD causes the electrons to drift towards N layer and holes towards P layer. An avalanche effect occurs when the electron-hole pairs acquire sufficient energy to create additional electron pairs by colliding with the crystal lattice. However, compared to a PD, an APD typically picks up more noise, needs a high voltage supply, and its dynamic range is lower than most PDs.

Among these three light detector options, the PDs were used for the wearable probe presented in this work, due to their inherent advantage in package size for tissue contact measurement, as well as the unparalleled dynamic range needed from the optical measurements at different source-detector separations.

2.7.3 Electronic switches and multiplexers

A CW DOSI imaging system, especially with multiple optodes, requires electronic switches and multiplexers. Electrical switches are a type of devices controlling the on and off of signal line. As an example, a metal-oxide-semiconductor field-effect transistor (MOSFET) is a three-terminal device that can be for electrical current switching applications. For example, it can be used to control the forward current to an LED during CW measurements.

Multiplexer (MUX) integrated circuits (ICs) are devices that select and route one of several analog or digital input signals into a single line. In terms of multi-optode CW DOSI instrumentation, MUX can be implemented to collect from multiple optical sensing channels. Demultiplexers (DEMUX), on the other hand, reverses the channel switching process in MUXs, and can be applied to switch driving current into different light sources.

Multiplexers in CW diffuse optical measurement can be implemented to perform frequency-division multiplexing (FDM) (Flexman et al. 2008) and time-division multiplexing (TDM) (Teng et al. 2017). FDM is inherently an analog technology, where continuous data acquisition is performed by combining electrical sensing signals at different modulation frequencies. TDM is a digital technology which uses time to separate the different data streams. TDM sequentially scans individual input channels then deliver signals to associated receivers.

With the help of digital bus and serial communication protocols, the multiplexing of large numbers of measurement channels can be engineered with elegance. For example, the serial control protocol I²C allows a master I²C processor to control up to

127 slave processors through only a data line (SDA) and a clock line (SCL). Channel selection within each slave can be chosen by calling its 8-bit register address. This protocol, due to its simplicity in wire connection and large capacity in channel selection, is widely applied in portable consumer and medical tissue imaging devices, and is used in the wearable probe developed in this work.

2.7.4 Previous CW DOSI instrumentation designed for breast imaging

Several prior CW instruments helped to inspire the work conducted in this thesis. For example, in 2010, researchers at Tufts University developed a broadband continuous-wave optical mammography system (Yu et al. 2010) which is shown in Figure 2.7. Imaging on the breast is performed in a parallel plate geometry where the breast is mildly compressed between two polycarbonate plates.

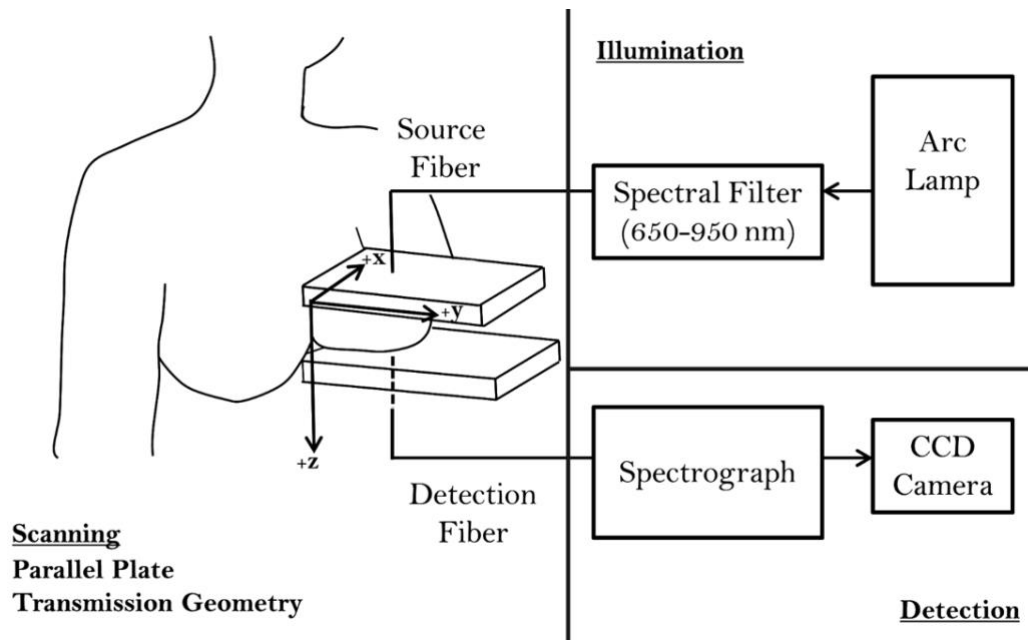


Figure 2. 7 Instrument diagram of a broadband optical imaging system. Adapted from (Anderson et al. 2015).

This instrument is capable of extracting the concentrations of tissue hemoglobin, water, and lipids, as well as the oxygen saturation in two-dimensional optical mammograms (Anderson et al. 2015).

A different tomographic breast tissue imaging system was developed at Columbia University and utilizes modulated light sources (~KHz) and aligns optical fibers into a hemisphere geometry that fits to the shape of female breast tissue.

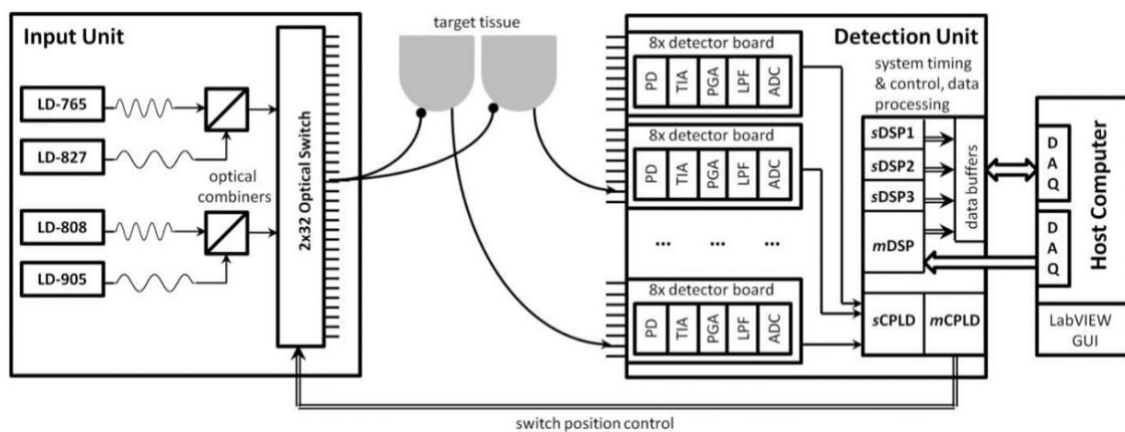


Figure 2. 8 Instrument diagram of a CW tomographic imaging system. Adapted from (Flexman et al. 2011).

This system performs real-time monitoring of breast tissue hemodynamics as a subject performs a breathhold. Clinical results derived from this instrument demonstrate the potential of breast hold measurement for separating healthy subjects from breast cancer subjects (Flexman et al. 2013).

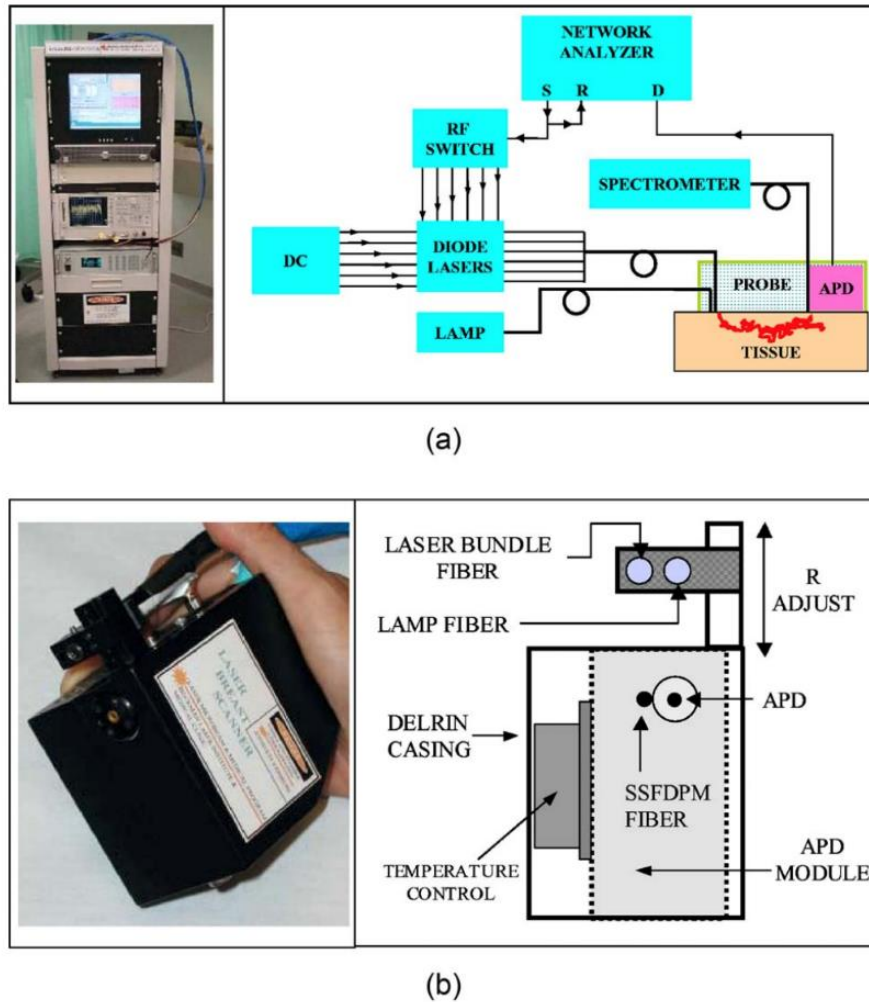


Figure 2. 9 System diagram and optical probe layout of a CW/FD diffuse optical imaging system design. Adapted from (Cerussi et al. 2006)

Our research group use a CW/FD DOSI system designed by the Beckman Laser Institute at University of California, Irvine. The CW module in this instrument is complementary to the FD measurements, and ultimately allows quantitative tissue optical property extraction over a continuous NIR spectrum. Figure 2.9 shows the system schematic diagram, also the layout of the optical probe for both CW and FD diffuse optical measurements.

These representative diffuse optical systems have successfully demonstrated their feasibility for clinical breast cancer imaging. They were used to conduct real-time as well as longitudinal measurements on breast cancer patients. These technologies utilized both transmission and remission imaging geometries over breast tissue and achieved topographic and tomographic tissue functional information. However, these designs also has several limitations. First, they use optical fibers for light delivery to and from the patient. This type of design is often bulky, heavy, and fragile. Second, the optical probe or patient/device interface is typically rigid and poorly conforms to the natural shape of human tissue, which could be uncomfortable for the patient, especially during extended measurements. Third, for optical probes with limited number of light sources and detectors, a 2D mapping of tissue properties may require the probe head sequentially scan over gridded positions on the skin. Therefore, data acquisition for each iteration may take 10s of minutes, and poor temporal and spatial resolution from this imaging protocol excludes the possibility of real time monitoring of tissue hemodynamics.

This thesis proposes, designs, and validates a breast tissue imaging system that addresses the limitations described above with wearable probes. To the best of my knowledge, this is the very first wearables designed or used for breast measurements.

2.8. Feasibility testing and prototype development of a CW wearable probe.

The goal of this work was to develop the first optical wearable probe for breast tumor monitoring. The following sections describes component feasibility testing, component selection, and early prototype probe design and fabrication. It also describes some probe testing data that were not included in subsequent chapters due to manuscript

space limitations (Chapters 3 and 4 are either published or in preparation for publication). Chapters 3 and 4 then describe more advanced wearable probe clinical prototypes and relevant *in vitro* and *in vivo* testing.

2.8.1 Selection of optical transducers

The optical transducers for the wearable diffuse optical imaging probe were chosen based on several criteria. First: the cost and simplicity of the hardware design. During the design process it was decided that the components should be commercially available off-the-shelf, which helps to reduce the cost of prototype design and simplifies fabrication of additional probes. Economical optical transducers, such as LEDs and photodiodes, are the favorable candidates in this sense. Second: fitness to a wearable device. Light emitters and detectors with surface mount packages have a low profile, compact pin layout, and have durable electrical contact with flexible copper layers. Thirds: the optical spectrum for tissue imaging. The emission spectrum of light source should cover relevant NIR wavelengths, where tissue absorption is strongly affected by hemoglobin concentration and its changes.

In order to address the question of wavelength selection, a condition number analysis was utilized to optimize the accuracy of extracting tissue hemodynamics (Corlu et al. 2003). The condition number $\kappa(A)$ of a matrix that maps extinction coefficients for HbO₂ and HHb is was used based on prior work (Corlu et al. 2003). It quantitatively measures the amplification of the noise from the input to the output. Therefore, optimized wavelength pairs correspond to a condition number close to one, which indicates calculations with Beer's Law at the chosen spectrum add zero uncertainty to the changes

in absorbance. This is the ideal case for calculating changes in tissue chromophore concentration. The condition number is expressed as

$$\kappa(A) = \|A^{-1}\| \cdot \|A\| \quad (14)$$

where $A = \begin{pmatrix} \varepsilon_{\lambda_1}^{HbO_2} & \varepsilon_{\lambda_1}^{HHb} \\ \varepsilon_{\lambda_2}^{HbO_2} & \varepsilon_{\lambda_2}^{HHb} \end{pmatrix}$ is the matrix of extinction coefficients for HbO₂ and HHb at

the chosen wavelength pair. In Figure 2.10, a contour line that represents $\kappa = 10^{0.5}$ is shown. The wavelength pairs that correspond to the region inside of the dashed line were considered to be the best choices for extractions of HbO₂ and HHb changes.

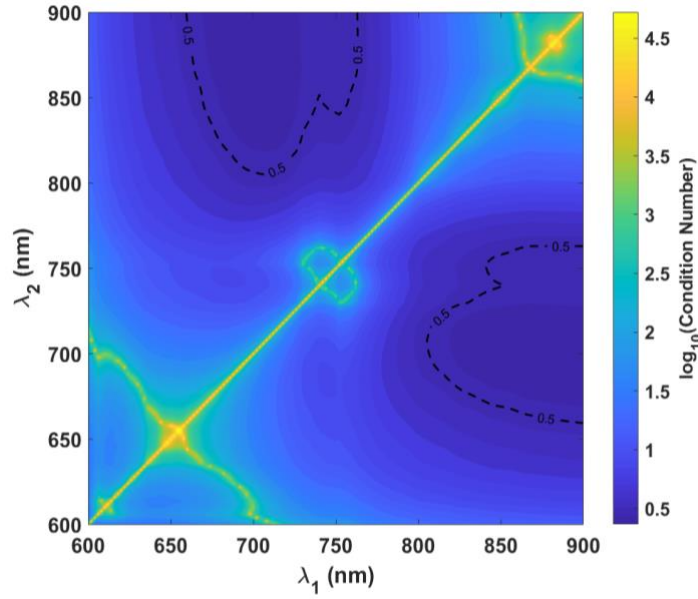


Figure 2. 10 Condition number of the matrix of extinction coefficients

Based on the condition number analysis as well as the other criteria described above, the following LEDs were chosen as optical sources for the wearable probe: SMT750-23 and SMT850-23. Both of these LEDs are in the PLCC-2 package and manufactured from Roithner Lasertechnik. Their central wavelengths are 750 nm and 850

nm, respectively. Two different photodetectors were considered for the wearable probe: the S4797-01, a Si photodiode made from Hamamatsu Photonics, and the TSL250RD-TR, an 8-SOIC Si light-to-voltage sensing module made from TAOS Inc. Both have relatively high responsivity at the LED wavelengths. Figure 2.11 shows the responsivity of the TSL250RD-TR.

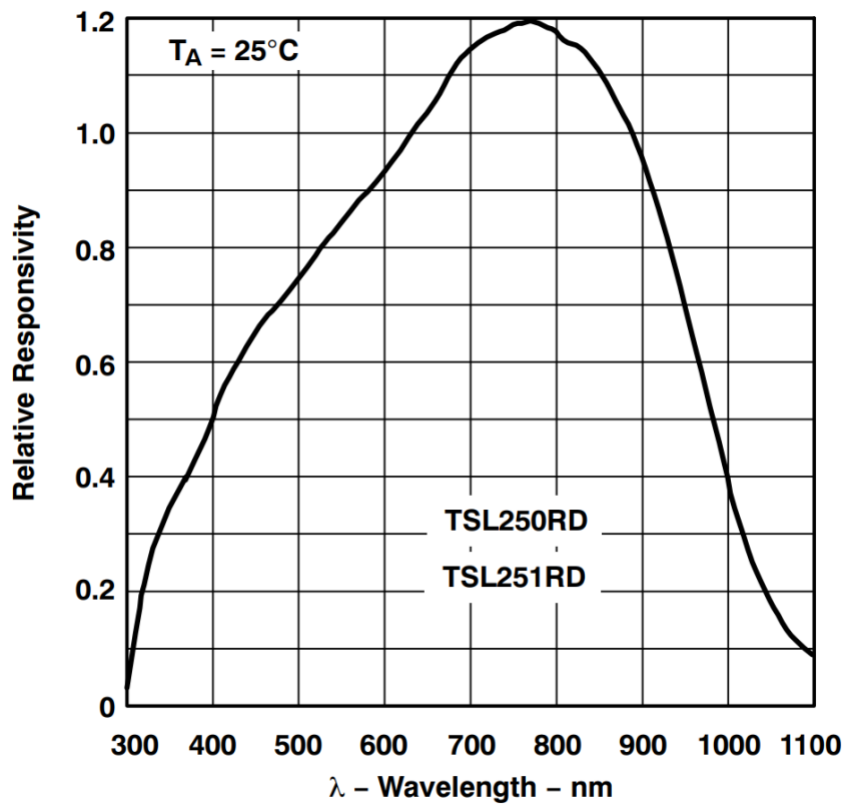


Figure 2. 11 Responsivity of Si sensing module

2.8.2 Validation of LED - photodiode pairs

A rigid printed circuit board (PCB) was designed and fabricated to test and validate the LEDs and the first photodiode (S4797-01, Hamamatsu Inc.). This test platform is shown in Figure 2.12. It contains six pairs of LEDs and one photodiode. The

layout of these optical transducers is based on previous design for breast tissue imaging, which places light sources onto the corners of a hexagon, while the detector is centered within this geometry (Chance et al. 2005). The source-detector optode separation is 25.4 mm and is similar to the set up in our frequency domain DOSI imaging system (Cerussi et al. 2006).

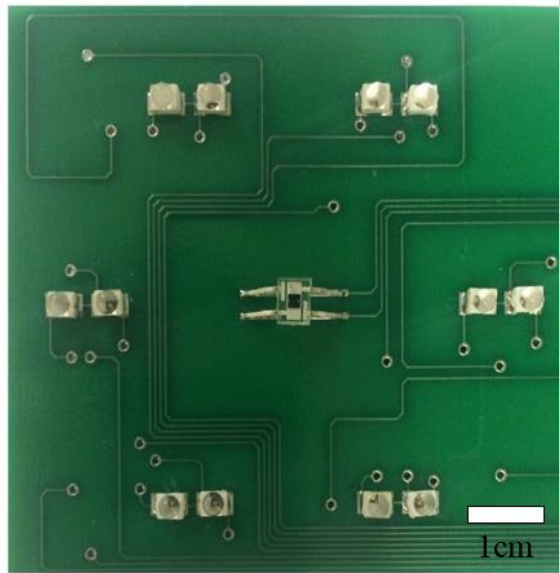


Figure 2. 12 Optical probe of first generation diffuse optical imaging system

The rigid optical probe was initially tested using a tissue-simulating solid silicone phantom. A diagram of a phantom measurement layout is shown in Figure 2.13. The collected photocurrent was conditioned with a transimpedance amplifier (TIA) before data acquisition with a 16-bit DAQ board (USB-6361, National Instruments).

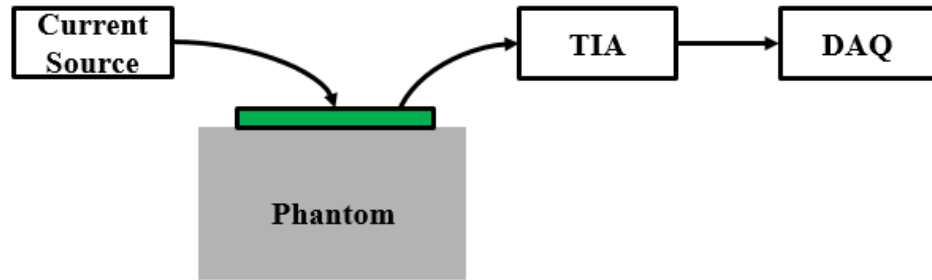


Figure 2. 13 Diagram of the rigid probe testing platform. Green shown the rigid PCB containing 12 LEDs and one photodiode.

Unfortunately, electrical noise strongly contaminated the transducer signal in this design. This was due to electromagnetic interference with the tiny photocurrent from the photodiode. To solve this problem, the S4797-01 photodiode was replaced with the TSL250RD-TR (TAOS Inc), which contained an integrated TIA within the detector package. Additionally, the optical signals were modulated at 1 kHz and the detected signal was passed through an analog band-pass filter to reduce noise. Additional design details of this source-detector pair are included in Chapter 3.

Validation of this new optode configuration was performed by fabricating a pair of small rigid PCBs for the LEDs and detector. The benefit of this design is that the source-detector separation can be adjusted freely through a wide range. The separation of light source and detector was tested from 21 mm to 49 mm. This range roughly corresponds to the range of advanced breast tumor diameters (Elkin et al. 2005). The system linearity was evaluated at each source-detector separation from phantom measurements by adjusting the LED forward current. In addition, dark measurement result, which is taken with a piece of black rubber, was compared with the phantom

measurements to quantify the signal to noise (SNR) level.

Figure 2.14 shows the results from the linearity testing. The data indicate excellent system linearity from 10 mA to 90 mA for most measurements, although detector saturation was a problem for short optode separations (less or equal to 20 mm). For longer optode separations, the collected signal was greater than the background noise by at least one order of magnitude. These results indicate that this transducer pair is promising for tissue optical measurements over a wide range of optode separations.

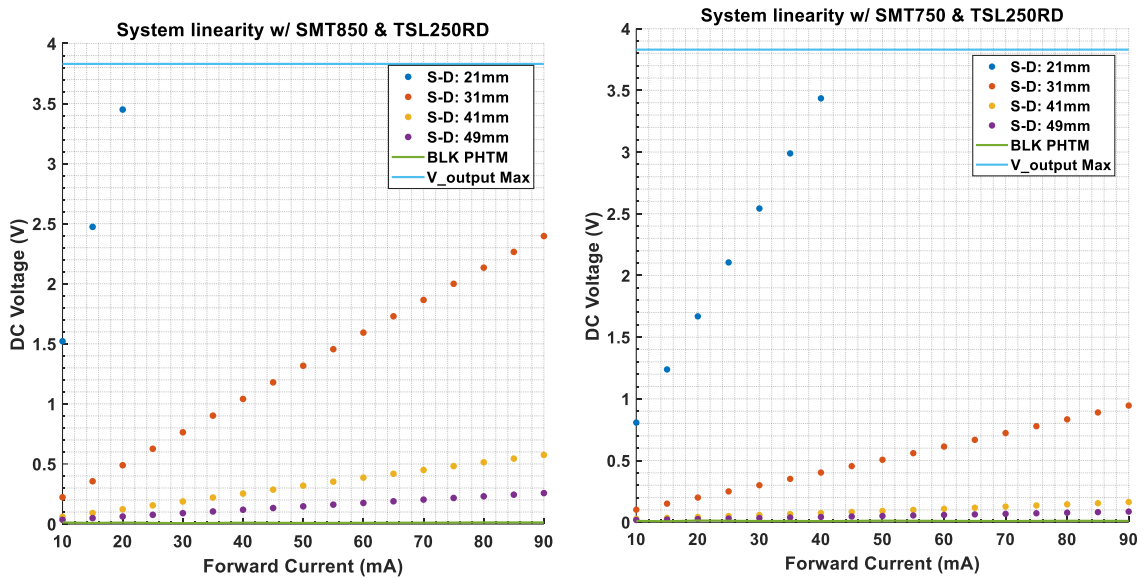


Figure 2. 14 Validation of single source and detector module with respect to different separations and forward current. Left: Measurements at 850 nm. Right: Measurements at 750 nm.

The LEDs and photodiode package described above were used for the wearable prototypes described in the following chapters.

CHAPTER 3. GENERATION II CW DIFFUSE OPTICAL SPECTROSCOPIC IMAGING SYSTEM

The Chapter is published in the Journal of Biomedical Optics 2017;22(1):14001. doi: 10.1117/1.JBO.22.1.014001, with the following title and contributing authors:

Wearable near-infrared optical probe for continuous monitoring during breast cancer neoadjuvant chemotherapy infusions

Fei Teng^a, Timothy Cormier^b, Alexis Sauer-Budge^b, Rachita Chaudhury^c, Vivian Pera^c, Raef Istfan^c, David Chargin^b, Samuel Brookfield^b, Naomi Yu Ko^d, Darren M. Roblyer^c

^a Boston University, Dept. of Electrical and Computer Engineering, Boston, MA, 02215, USA

^b Boston University, Fraunhofer Center for Manufacturing Innovation, Boston, MA, 02446, USA

^c Boston University, Dept. of Biomedical Engineering, Boston, MA, 02215, USA

^d Section of Hematology and Oncology, Women's Health Unit, Boston Medical Center, 801 Massachusetts Ave, First Floor, Boston, MA, 02118, USA

3.1 Introduction

Optical wearables may provide new opportunities for tracking healthy and disease states longitudinally, including time points currently unobtainable with standard-of-care clinical imaging modalities. Superficial-probing wearable optical heart rate monitors are widely available in the consumer space for fitness tracking, but there has been substantially less development in the medical space for deep tissue applications in oncology. We present here a new diffuse optical wearable probe, designed to track tumor metabolism and hemodynamic changes during breast cancer chemotherapy treatment. This new imaging platform may allow for the identification of important new prognostic timepoints that can be used to modify treatment and drug regimens for individual patients.

The optical measurement of tumors in the breast typically requires the measurement of multiply-scattered near-infrared (NIR) light which has traveled up to several centimeters in depth. Due to the diffusive nature of photon propagation in thick biological tissue, techniques that employ these measurements are usually referred to as Diffuse Optical Imaging (DOI) or Diffuse Optical Spectroscopy (DOS). (Jacques and Pogue 2008) These methods have been widely shown to be capable of extracting tissue level concentrations and/or changes in concentration of key functional parameters in the breast, brain, muscle, and other tissues. Depending on wavelengths utilized, the parameters may include oxyhemoglobin, deoxyhemoglobin, water, and lipids. (Choe and Durduran 2012) Diffuse optical techniques can be broadly classified into three variants: continuous wave (CW), frequency-domain (FD), and time-domain (TD) methods. FD and

TD techniques provide separation of optical absorption and scattering effects, but typically require modulated or pulsed laser sources and sensitive avalanche photodiodes (APD) or photomultiplier tube (PMT) detectors.(Pogue et al. 1997; Pham et al. 2000; Yu et al. 2003) CW techniques can provide relative changes in tissue chromophores if assumptions or prior knowledge of the wavelength dependence of scattering are available.(Gao et al. 2011) In situations where the optical scattering can be assumed to be time-invariant, CW DOI or DOS can be used to monitor hemodynamic and metabolic changes in tissue with relatively simple instrumentation and analysis techniques. This is especially relevant over short time periods (seconds to hours).(Benni et al. 2005; Coyle, Ward, and Markham 2007; Tisdall et al. 2009) Measurements are possible with inexpensive LEDs and photodiodes, and surface-mount packaging of these components reduces the device footprint and facilitates the design of flexible optical probes that can be used in direct contact with skin. These features provide the possibility for wearable CW imaging probes for measurements of deep tissue hemodynamics. Several optical wearables have been previously developed and applied for studies related to cardiology,(Stojanovic and Karadaglic 2013) general purpose blood oxygen saturation,(Muehlemann, Haensse, and Wolf 2008; Stojanovic and Karadaglic 2013) and cerebral activity,(Muehlemann, Haensse, and Wolf 2008; Atsumori et al. 2009; Piper et al. 2014; McKendrick, Parasuraman, and Ayaz 2015; Pinti et al. 2015) but we know of no prior work in optical wearables for tumor chemotherapy monitoring.

Prior DOI and DOS instrumentation, which include both largely immobile platforms and more portable handheld probes, have been previously utilized to monitor

chemotherapy response in breast cancer patients receiving neoadjuvant (presurgical) chemotherapy. FD techniques,(Shah et al. 2001b; Zhou et al. 2007; Cerussi et al. 2010; Roblyer et al. 2011; Ueda et al. 2012; Jiang et al. 2014) TD techniques,(Torricelli et al. 2003; Spinelli et al. 2005; Taroni et al. 2010; Falou et al. 2012) and CW techniques (Flexman et al. 2011, 2013; Anderson et al. 2015) have been employed to track tumor hemoglobin, water, and lipid changes throughout treatment. Most prior studies have been focused on changes in tissue chromophore concentrations after weeks of treatment. For example, Cerussi et al. showed that, by comparing the functional properties between tumor and normal tissue, breast cancer patients who achieved pathologic complete response to neoadjuvant chemotherapy had a 23% reduction in total hemoglobin on average by the midpoint in treatment compared to a 11% reduction in partial and non-responders.(Cerussi et al. 2011) Other groups have shown similar trends.(Zhu et al. 2008; Soliman et al. 2010; Busch et al. 2013; Jiang et al. 2014) Recently, it was reported that changes in oxyhemoglobin concentration on the first day after an initial chemotherapy infusion could statistically differentiate responders from non-responders.(Roblyer et al. 2011) We hypothesize that hemodynamic changes during the first chemotherapy infusion (typically lasting several hours) may also be prognostic of long-term treatment response. A new wearable CW DOI probe is presented here which was designed to monitor these very early time points. The performance of the probe was evaluated *in vitro* using tissue-simulating phantoms and *in vivo* with a cuff occlusion test. Additionally, a normal volunteer was measured continuously over a period of 10 minutes to evaluate the stability and comfort of the probe.

3.2 Instrument Design

The CW wearable probe was designed to be flexible in order to accommodate the natural curvature of human breast tissue. Figure 3.1(a) shows the flexible printed circuit board (PCB) with optical and electrical components. The flexible PCB was fabricated with two mil (51 μm) copper and polyimide. From the central hub of the wearable probe, six flexible arms radiate and form into the backbone of a hexagon. Each arm has an LED pair at its terminal end; the seventh arm terminates with a micro-HDMI connector. A photodiode module is positioned at the central hub.

The surface mount LED pairs (SMT750-23 and SMT850-23, Roithner Lasertechnik) have a peak emission wavelength of 750 nm and 850 nm, and each generates a total optical output power of approximately 20 mW at a 50 mA forward current.(Eggebrecht et al. 2014) The optical detector module (TSL250RD, ams AG) has a 1 mm active area photodiode with an integrated transimpedance amplifier with an irradiance responsivity of approximately 74 mV/($\mu\text{W}/\text{cm}^2$). The source-detector separation between the LEDs and the photodiode is 25.4 mm. Similar source-detector separations have been shown to provide adequate optical depth penetration for measurements of most breast tumors eligible for neoadjuvant chemotherapy. (Benni et al. 2005; Izzetoglu et al. 2005; Cerussi et al. 2007; Roblyer et al. 2011) A thin plastic stiffener was fabricated to add rigidity from the central hub to the 7th radiating arm, which serves as the cable connection point. A 19-pin micro HDMI cable is used to communicate between the wearable probe and benchtop control electronics. Figures 3.1(b) and 3.1(c) show the completed probe. A hexagonal medical grade silicone housing

encapsulates the probe and has a dimension of 90.7 mm between the opposite vertices. The maximum thickness of the encapsulated probe is 11.3 mm, and it has a total mass of 48.9 grams. The probe is highly flexible along all dimensions except the dimension parallel to the HDMI cable due to the plastic stiffener (Fig 3.1(d)).

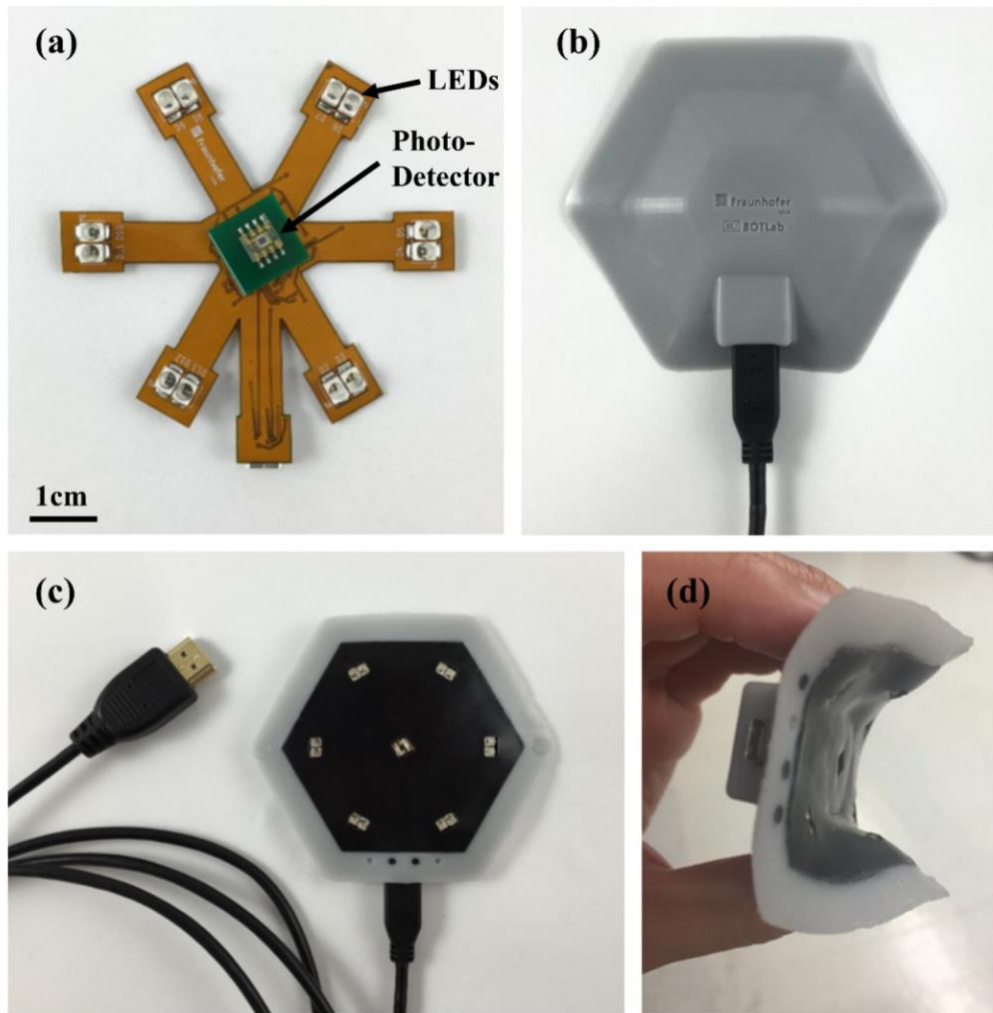


Figure 3. 1 (a) Flexible PCB and optical components. (b) Top and (c) bottom view of the wearable probe. (d) Flexibility of the probe under gentle pressure.

Figure 3.2 shows a block diagram of the probe and control electronics. A data acquisition board (National Instruments USB-6361) provides a low frequency sinusoidal

analog signal as a modulation input to the current controller (ILX Lightwave, LDX-3525B), which in turn provides the forward current to the LEDs with a modulation index of 0.9. The forward current is modulated at 1 KHz to assist in rejection of background noise, 60 Hz electrical noise and harmonics, and to match the response from the photodetector. A 4-bit digital control signal is also generated by the DAQ to control the sequence of LED illumination. Digital and analog signals are delivered to the probe through an HDMI cable. The digital lines are fed into a 4-to-16 line decoder (74HC/HCT4514, Philips Semiconductors) which direct the current into individual LEDs through a bank of MOSFET switches. On the detection side, the photodiode provides a linear response to light intensity, and photocurrent is converted to a voltage signal with an integrated transimpedance amplifier. The amplified signal is routed through the HDMI cable and is further amplified by 10 dB and filtered through a custom 1 KHz 8th order Bessel band-pass filter (BPF) with a 200 Hz -3dB passband width prior to data acquisition. The probe is controlled using a custom LabView program.

During operation, each of the twelve LEDs is illuminated sequentially, and a complete measurement cycle is defined as measurements collected from all twelve optode pairs. Data is acquired at 100K samples per second with a sampling length of 50 ms for each optode. Due to the delay from BPF settling time, and other optical and electronic components, a 35 ms delay was added between optode measurements. A complete measurement cycle takes 1020 ms (85 ms x 12). A delay can be added between measurements cycles depending on desired experimental conditions.

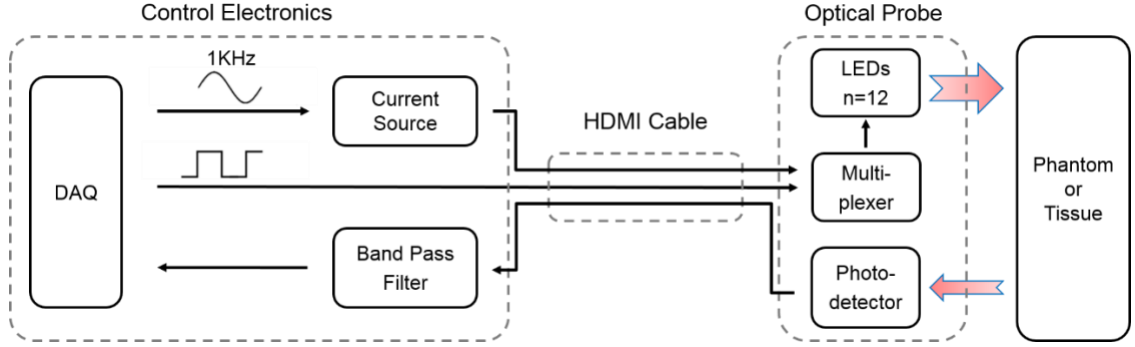


Figure 3. 2 Schematic view of CW diffuse optical imaging system. Solid line: electrical signal. Red arrow: optical signal

3.3 Instrument Performance

Initial performance testing was conducted using tissue simulating silicone solid phantoms and blood-intralipid based liquid phantoms.

3.3.1 Signal to Noise Ratio (SNR), Dynamic Range, and System Crosstalk

The system voltage outputs were processed using a Fast Fourier Transform (FFT) with a rectangular window to compute SNR and dynamic range. Power measurements of the signal-of-interest were summed over a 500 Hz band centered at 1 KHz in the FFT, and DC and the first ten harmonics were excluded for these calculations. SNR and dynamic range were calculated as $10\log(P_{\text{signal}}/P_{\text{noise}})$. SNR measurements were taken on a set of three breast-like tissue-simulating solid phantoms with the following optical properties: phantom 1: $\mu_a = 0.0054 \text{ mm}^{-1}$ (750nm), $\mu_a = 0.0038 \text{ mm}^{-1}$ (850nm), $\mu'_s = 1.2 \text{ mm}^{-1}$ (750nm), $\mu'_s = 1.0 \text{ mm}^{-1}$ (850nm); phantom 2: $\mu_a = 0.0045 \text{ mm}^{-1}$ (750nm), $\mu_a = 0.0032 \text{ mm}^{-1}$ (850nm), $\mu'_s = 1.1 \text{ mm}^{-1}$ (750nm), $\mu'_s = 0.9 \text{ mm}^{-1}$ (850nm); phantom 3: $\mu_a = 0.0036 \text{ mm}^{-1}$ (750nm), $\mu_a = 0.0026 \text{ mm}^{-1}$ (850nm), $\mu'_s = 0.9 \text{ mm}^{-1}$ (750nm), $\mu'_s = 0.8$

mm-1 (850nm). These optical properties closely match prior reported normal breast tissue values.(Durduran et al. 2002; Shah et al. 2004) A SNR greater than 68 dB for channels with 750 nm LEDs, and greater than 71 dB for channels with 850 nm LEDs was achieved for measurement on a breast-like tissue-simulating solid phantom. The system dynamic range was at least 80.4dB when measuring the maximum optical signal level. During normal operation, it is possible that light may travel directly from source to detector along the tissue surface causing undesired optical source-detector crosstalk. Additionally, inductive coupling may cause undesired electrical crosstalk at the PCB level or in the HDMI cable. In order to evaluate both electrical and optical crosstalk, measurements were taken on a highly absorbing black phantom, and a 7 dB signal for the 750 nm LEDs, and 6 dB signal for 850 nm LEDs was observed at the 1 KHz modulation frequency relative to the average noise floor. This indicates that the crosstalk signal is at least 60 dB weaker than the signal from breast-like tissue phantom measurements.

3.3.2 System Drift

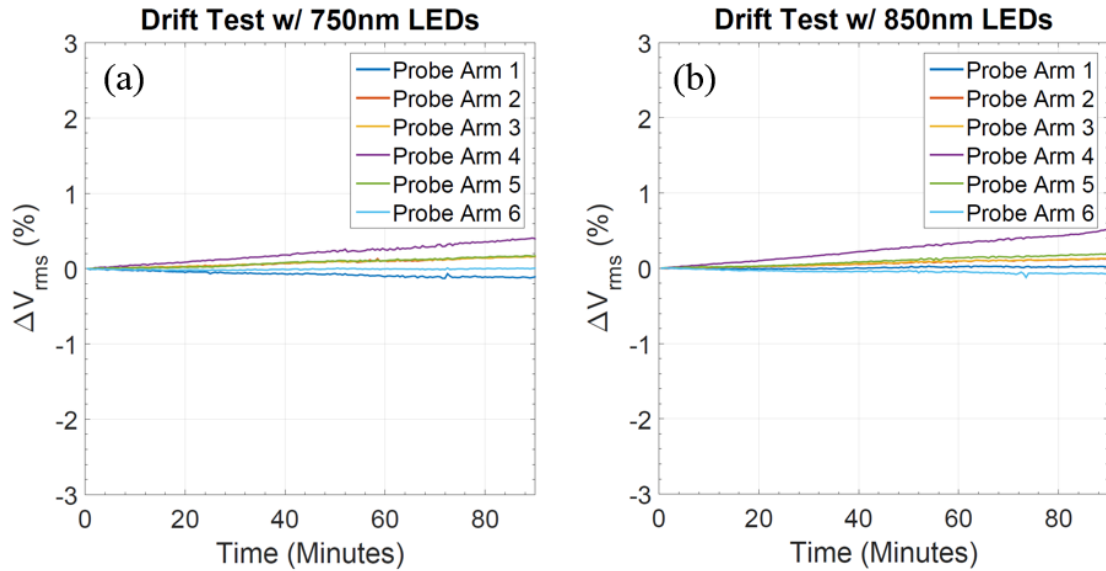


Figure 3. 3 System drift test. Results are shown for (a) the 750 nm and (b) 850 nm optical channels. An average drift of 0.18% or less was observed over the 90-minute test.

A system drift test was performed to evaluate the repeatability of the system under static experimental conditions. 180 repeat measurement cycles were acquired over 90 minutes (a typical chemotherapy infusion length), and results from each source-detector (optode) pair were normalized relative to the Root-Mean-Square value of modulated signal (V_{rms}) from the first measurement. Fig 3 shows the drift for each source-detector pair (each source-detector pair is identified by its probe arm in the figure legend). On average, an absolute system precision of 0.17% was achieved for optical channels with 750 nm LEDs and a precision of 0.18% was achieved for optical channels with 850 nm LEDs. The largest single optode drift was observed in probe arm 4, equaling

0.40% and 0.51% for the 750 nm and 850 nm LEDs, respectively. These results indicate that the probe is capable of highly repeatable measurements.

3.3.3 Thermal Stability

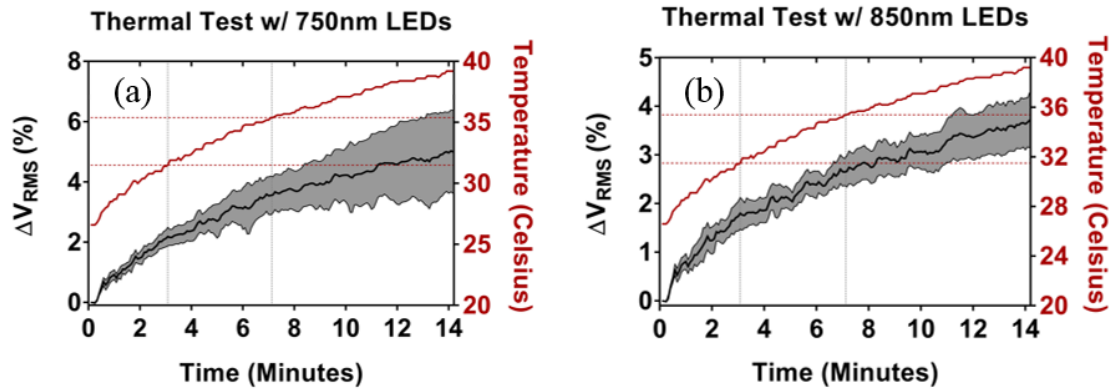


Figure 3. 4 System thermal response to local probe temperature changes. The red solid line corresponds to the local temperature measured at the probe, while the black solid line corresponds to the normalized changes in detector voltage levels. The shaded area indicates the standard derivation calculated from the optodes that share the same wavelength. The red dashed lines show the upper and lower bound of normal physiological temperature of human skin.(Olesen 1982)

A thermal stability test was conducted in order to determine the sensitivity of the probe to different ambient temperatures. This is relevant as the probe will be placed directly against the subject's skin, and skin temperature may change over time. A thermal sensor from a thermal data logger was positioned in contact with the underside of the probe. Five minutes of repeated measurements were taken on a solid phantom to establish a baseline; measurements were taken every five seconds. The local temperature of the

probe was controlled using a hotplate which was positioned under the optical phantom. The hotplate was then turned on and the probe temperature rose from approximately 26.6°C to 39.2°C over a period of approximately 14 minutes. Figure 3.4 shows the thermal response of the probe for the 750 nm and 850 nm optical channels. Within a normal physiological temperature range(Olesen 1982) (indicated by the area between two horizontal dashed lines in Figure 3.4), measured voltage changes correspond to an average thermal response of 0.35% V_{rms} per degree ($V_{rms}/^{\circ}C$) for the 750 nm channels and 0.22% V_{rms} per degree ($V_{rms}/^{\circ}C$) for the 850 nm channels. These results indicate only minor fluctuations in instrument response over the expected operating temperature range.

3.3.4 Probe Accuracy

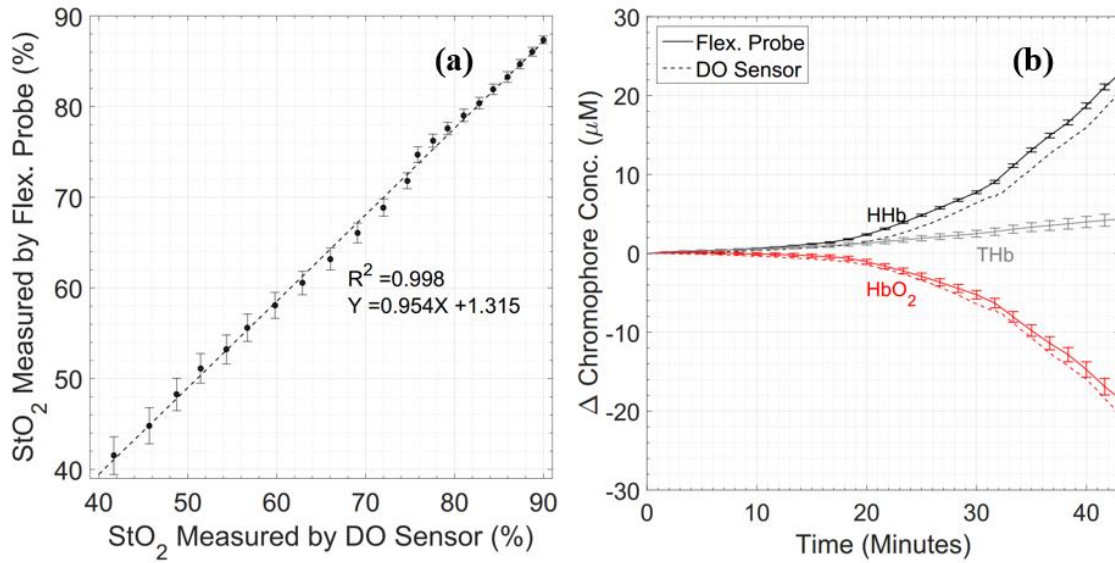


Figure 3. 5 Probe results compared to a dissolved oxygen sensor for (a) oxygen saturation and (b) chromophore concentration changes measurements taken from a blood-intralipid phantom during phantom deoxygenation.

To determine the accuracy of the wearable probe, it was tested against a commercial dissolved oxygen (DO) sensor (VisiFerm DO Arc 120, Hamilton Robotics), which served as a gold standard for this study. Measurements were taken on a blood-intralipid based liquid phantom during dynamic oxygenation changes. The phantom was made by adding 17 ml of pooled bovine blood (Carolina Biological Supply Company), 48 ml of intralipid (Fresenius Kabi, 20% I.V. Fat Emulsion), 120 ml of 10X Phosphate Buffered Saline (PBS) solution (Fisher Scientific), and 1015 ml of deionized water for a total phantom volume of 1200 ml. The phantom was contained in a 6-inch diameter cylindrical baking pan placed on a stirring hotplate which maintained a constant phantom temperature of 37°C. A magnetic stir bar was used to stir the phantom at a constant

spinning rate of 120 revolutions per minute.

The phantom started near 100% oxygen saturation and was slowly deoxygenated by adding a solution of baker's yeast, made by dissolving active dry yeast into deionized water with a concentration of 1 mg/ml. A total of 4.2 ml yeast solution was gradually added to the phantom which caused a change in oxygen saturation from approximately 100% to 34% over a 43-minute period. During this time, the wearable probe and the DO sensor simultaneously monitored the hemodynamics in the liquid phantom. Temperature and pH were monitored continuously throughout the test. The DO sensor measures the concentration of unbound oxygen, and DO concentrations were converted to oxygen saturation values using a published dissociation curve for matching temperature and pH levels.(Kelman 1966) DO measurements were taken every five seconds over the 43 minute period.

The Modified Beer-Lambert Law (MBLL) was utilized to convert the raw V_{rms} measurements from the wearable probe to oxygen saturation values as well as changes in oxyhemoglobin and deoxyhemoglobin concentration.(Kocsis, Herman, and Eke 2006) Measurements of the initial optical properties of the liquid phantom were taken using an in-house frequency domain diffuse optical spectroscopic imaging system. The initial optical properties were then used to calculate a differential pathlength factor assuming a homogeneous semi-infinite medium:(Arridge, Cope, and Delpy 1992)

$$DPF(\lambda) = \frac{1}{2} \left(\frac{3\mu'_s(\lambda)}{\mu_a(\lambda)} \right)^{\frac{1}{2}} \left[1 - \frac{1}{(1 + d(3\mu_a(\lambda)\mu'_s(\lambda))^{\frac{1}{2}})} \right] \quad (15)$$

where $\mu_a(\lambda)$ and $\mu'_s(\lambda)$ are the absorption and reduced scattering coefficient of diffusive medium, d is the separation of source and detector on the probe. The liquid phantom had a total hemoglobin concentration of approximately 30.8 μM , which is estimated from previously reported values for bovine blood (13 to 15 g/100mL).(Fraser 1991) Changes from an initial value of approximately 100% oxygen saturation (as verified by the DO sensor) were computed and compared with values from the DO sensor. Wearable probe measurements were taken once every five seconds during the 43-minute period.

Figure 3.5(a) shows the agreement between the wearable probe and the DO sensor for saturation values between 40% and 90%. Typical oxygen saturation levels of human breast tissue have been shown to be approximately 68%,(Srinivasan et al. 2006) and the tested range here was chosen as it is inclusive of saturation levels that meet or exceed those expected in human breast measurements. There is less than 5% disagreement in oxygen saturation measurements between the wearable probe and the DO sensor over this range, with an R^2 value of 0.998. Figure 3.5(b) shows changes in oxyhemoglobin (HbO₂), deoxyhemoglobin (HHb), and total hemoglobin (THb) over the 43-minute period. There was reasonable agreement between the wearable probe and the DO sensor for HbO₂ changes, with a difference of 2.13 μM by the end of the test. There were slightly larger differences in HHb measurements, with a maximum difference of 2.84 μM by the end of the test. These differences may be caused by a number of factors, including errors in the initial optical property estimates or small system nonlinearities.

3.4 *In vivo* Measurements

3.4.1 Cuff Occlusion Test

A cuff occlusion test was performed to demonstrate the *in vivo* measurement performance of the wearable probe. Baseline optical properties of the forearm were obtained from literature values. (Matcher, Cope, and Delpy 1997; Franceschini et al. 1999) The MBLL was used to determine chromophore concentration changes as before with optical scattering assumed constant over the measurement. Measurements were taken every 1.02 seconds during the occlusion test.

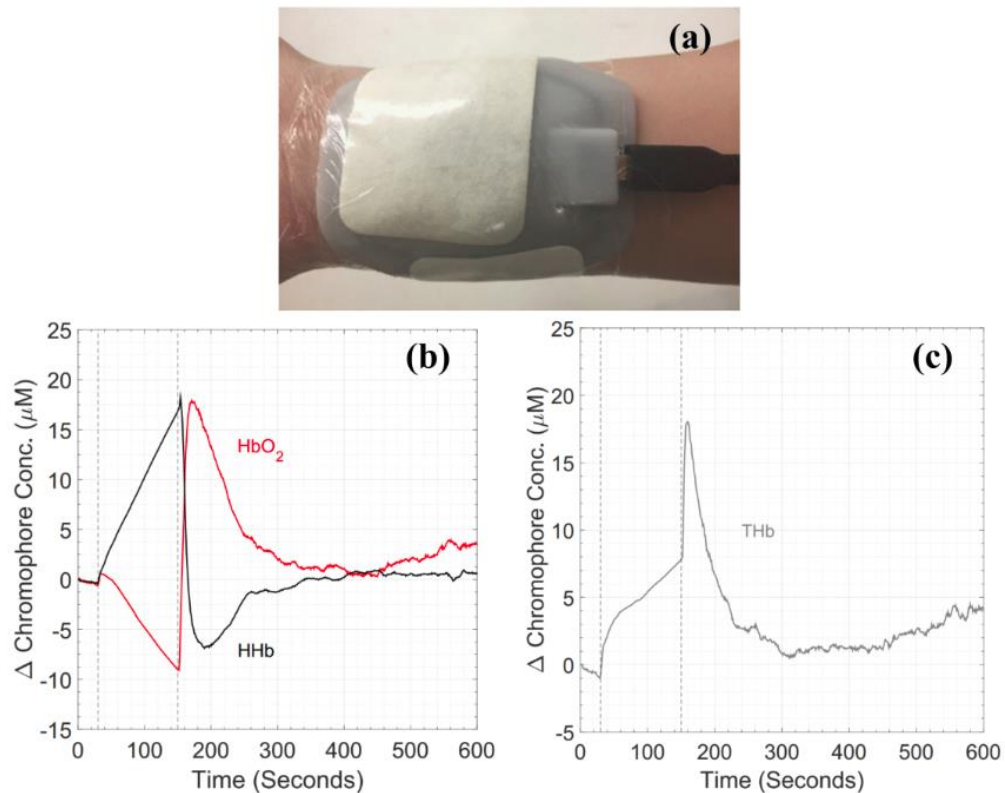


Figure 3. 6 (a) The probe is secured to the subject's skin using IV tape during cuff occlusion measurements. (b) and (c) Hemodynamic response at forearm during cuff occlusion test.

Figure 3.6 shows continuous extractions of oxyhemoglobin, deoxyhemoglobin, and total hemoglobin molar concentration changes from a single source-detector pair during the cuff occlusion. The wearable probe was securely attached to the forearm, and an adult blood pressure cuff was applied to the upper arm of a healthy volunteer with no pressure added to the aneroid sphygmomanometer. Starting from $t = 30$ sec, cuff pressure was rapidly increased to a maximum of approximately 200 mmHg. From the 30th second to the 150th second, the concentration of oxyhemoglobin gradually decreased while deoxyhemoglobin concentration increased at a faster rate. Changes in the total hemoglobin concentration during this period indicate a net influx of oxygenated blood into the forearm, which might be due to incomplete occlusion of arterial supply. At $t = 150$ sec, the cuff pressure was released, and oxygenated blood quickly refilled the forearm circulation, causing a rapid rise in oxyhemoglobin and total hemoglobin with a corresponding decrease in deoxyhemoglobin. Chromophore concentrations gradually returned to steady state. These observations match expectations and demonstrate the ability of the probe to measure hemodynamic changes in the *in vivo* setting. (Li et al. 2013)

3.4.2 Normal Volunteer Test

As a proof of concept, a normal volunteer test was conducted on a 46 year old pre-menopausal woman to evaluate the feasibility of taking continuous measurement over healthy female breast tissue. This test was carried out under the approval of Boston University Institutional Review Board.

The wearable probe was placed on the top left corner of her left breast, with a 5 mm distance between the wearable probe and the nipple. The HDMI cable was supported by placing it over the subject's neck and the wearable probe was secured using IV tape. The probe was allowed a ten-minute warm-up and stabilization period prior to optical measurements. The volunteer was allowed to move in the chair during the measurement. Repeated measurement cycles were taken every 1.2 seconds.

Figure 3.7 shows chromophore concentration changes over a ten-minute measurement period, which is a portion of a longer measurement. A 0.08Hz low-pass filter was applied to remove known physiological signals including heart beat (approximately 1Hz, aliased to 0.17 Hz for the sampling rate used), respiration (0.2 to 0.3Hz) and Mayer waves (approximately 0.1Hz). (Toronov et al. 2000; Tong, Lindsey, and Frederick 2011; Kirilina et al. 2013) The remaining low frequency components are expected to contain contributions from motion as well as tissue oxygenation fluctuations during resting state, which typically vary on sub-minute to minute time frames. (Jiang et al. 2013) Prior to filtering, variations in CW signal level were generally around 5%, which agrees well with previously reported measurements on healthy breast tissue over a similar time frame. (Durduran et al. 2002) We note that motion artifacts do have the potential to mask or mimic underlying physiological changes in breast tissue, and methods to detect and remove these from the data are currently being investigated.

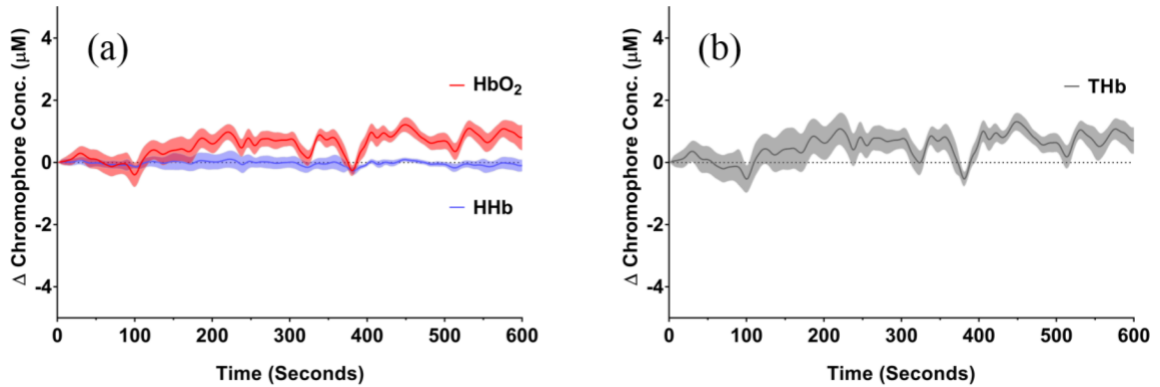


Figure 3. 7 Hemodynamic fluctuations of healthy female breast tissue at resting state. (a) Oxyhemoglobin (HbO_2) and deoxyhemoglobin (HHb), (b) total hemoglobin (THb).

3.5 Discussion

This work demonstrated the performance of a new, deep-tissue, optical wearable probe designed for monitoring breast cancer patients during presurgical chemotherapy. Tissue-simulating phantom measurements revealed low crosstalk (-60dB), high SNR (71dB), high precision (0.17%), and good thermal stability ($0.22\% \text{ V}_{\text{rms}}/\text{°C}$). The accuracy of our CW measurements was evaluated with a blood liquid phantom at different saturation levels, which resulted in less than 5% error in oxygen saturation estimates. Cuff occlusion and breast measurements reflected expected tissue hemodynamics.

The probe was specifically designed to monitor breast tumor oxygenation changes throughout chemotherapy infusions, which typically consist of one to three different cytotoxic and/or targeted agents sequentially infused intravenously over a period of several hours. There are several application specific considerations that affected the design of

this probe and ultimately differentiate it from other ambulatory and wearable diffuse optical devices that have been developed for monitoring cerebral or muscle oxygenation. First, the probe was designed to be highly flexible to conform to the natural breast tissue shape while still being housed in a single unit with static optode geometry in order to enable measurement comparisons between subjects. Additionally, although the investigation of chemotherapy induced changes during infusions is an emerging area of research, it is expected that substantial hemodynamics will likely change over timescales of minutes to hours, substantially slower than the timecourse of cerebral evoked potential or functional activations typically observed in the brain, or muscle contraction and relaxation observed for fitness monitoring applications. This relaxes the requirement for rapid measurement speeds often sought for other DOT applications, but increases the need for stable and repeatable measurements over long time periods. Our design was shown to provide highly stable measurements during phantom experiments, and only small fluctuations were observed during the normal breast measurement, but the issue of motion artifact reduction must be properly addressed prior to implementation in the clinical setting. We are currently exploring better ways of stabilizing the probe on the breast along with signal processing approaches for removing these artifacts from the data. It is of note that the largest change from baseline in HbO₂ concentration observed during the normal volunteer measurements in this study was approximately 8% over a 10 minute period. In comparison, changes of approximately 20 to 40% in HbO₂ were observed after the first 24 hours in patients receiving neoadjuvant chemotherapy in a prior study.(Roblyer et al. 2011) In the future, a normal volunteer study will be conducted to

better identify the magnitude of natural physiological variations in breast hemodynamics during multi-hour measurements in order to better understand how continuous measurements may be able to track treatment response.

To the best of our knowledge, this CW imaging system is the first demonstration of a wearable device aimed at continuously monitoring the hemodynamic response from breast cancer patients and represents a promising new tool to target unexplored prognostic timepoints during neoadjuvant chemotherapy infusions.

3.6 Disclosures

The authors have no conflicts of interest.

3.7 Acknowledgements

The authors gratefully acknowledge funding from the National Institute of Biomedical Imaging and Bioengineering of the National Institutes of Health (NIBIB-NIH) under the grant number: 5-U54-EB015403 and the Boston University – Fraunhofer USA Inc. Alliance Award.

CHAPTER 4. GENERATION III CW DIFFUSE OPTICAL SPECTROSCOPIC IMAGING SYSTEM

The Chapter is in preparation for publishing with the following contributing authors:

Fei Teng^a, Vivian Pera^b, Hannah Peterson^b, Tim Cormier^c, Alexis Sauer-Budge^c, David Chargin^c, Sam Brookfield^c, Adam Eggebrecht^d, Naomi Ko^e, Yingdi Tang^b, Darren Roblyer^b

^a Boston University, Dept. of Electrical and Computer Engineering, Boston, MA, 02215, USA

^b Boston University, Dept. of Biomedical Engineering, Boston, MA, 02215, USA

^c Boston University, Fraunhofer Center for Manufacturing Innovation, Boston, MA, 02446, USA

^d Washington University, Dept. of Radiology, St. Louis, MO, 63110, USA

^e Section of Hematology and Oncology, Women's Health Unit, Boston Medical Center, 801 Massachusetts Ave, First Floor, Boston, MA, 02118, USA

4.1 Introduction

Locally advanced breast cancers (LABC) are breast tumors that are large (>2 cm), may have a direct extension to the skin or chest wall, or present with regional metastasis to lymph or mammary nodes (Garg and Prakash 2015). LABC presents at least three substantial challenges to clinical treatment. First, the 5 year overall survival rate for LABC patients can be as low as 76% even after a combination of surgery, radiotherapy

and chemotherapy (SEER Cancer Statistics Review 2018). Second, with traditional treatment procedures most subjects have to endure mastectomy, which aggressively removes the entire affected breast and axillary lymph nodes (Steligo 2017). Third, some primary breast tumors may not be resectable as the cancer invades the skin or chest wall (Garg and Prakash 2015).

To overcome these challenges, preoperative chemotherapy, also called neoadjuvant chemotherapy (NAC), was introduced to shrink tumor size before surgery. NAC has been increasingly adopted as the default treatment plan for LABC patients (Ragaz, Band, and Goldie 2012). The pathological outcome to NAC, proposed by the American Joint Committee on Cancer (AJCC), is staged as complete response (pCR): absence of invasive carcinoma in the breast and node, partial response (PR): downgrade in either or both tumor (T) or node (N) stage, and no response (NR): stable or increase in either or both T or N stage (AJCC 2017). Approximately 10% of LABC patients achieve pCR, 60% PR, and 30% NR, even after weeks to months of treatment. Some patients may even develop progressive disease during NAC (Kuerer et al. 2000; Esserman 2004; Keam et al. 2013). Therefore, the prediction of patients' response to NAC at earlier timepoints based on tissue anatomic or functional imaging could be highly valuable in optimizing the treatment plan and maximizing outcomes.

Several traditional clinical imaging methods have been explored for breast cancer monitoring during the course of NAC. For example, positron emission tomography/computed tomography (PET/CT) using fluorine-18-fluorodeoxyglucose (18F-FDG) has been reported to predict patients' response with about 80 - 90% accuracy

(Schelling et al. 2000; Chen et al. 2004; Biersack, Bender, and Palmedo 2008). Magnetic resonance imaging (MRI) and functional MRI have both demonstrated prognostic value for NAC (Esserman et al. 1999; Heldahl et al. 2011; Rigter et al. 2013; Dave et al. 2017). Ultrasonography and mammography have both been studied for NAC monitoring, but their prognostic accuracy is not comparable to the imaging modalities mentioned above (Tadayyon et al. 2016; Gu et al. 2017; Nam et al. 2017).

Unfortunately, these clinical imaging modalities are accompanied by high expense, lack of portability, and/or safety issues due to the use of ionizing radiation or exogenous contrast agents. In contrast, diffuse optical imaging, which utilizes near infrared light and portable imaging platforms, avoids these limitations. Previous studies with these diffuse optical instruments have demonstrate that the pathological response of LABC patients to neoadjuvant chemotherapy can often be determined within weeks to months after the start of treatment, and are typically associated with a decrease of hemoglobin concentration and water content, and an increase of lipid concentration (Cerussi et al. 2007; Jiang et al. 2009; Choe and Durduran 2012). Recently, the acute response (first hours to days of treatment) to NAC has also been shown to manifest through significant difference between responders and non-responders when monitored with diffuse optical instruments. For example, in a study of 23 LABC subjects, tissue oxyhemoglobin concentration was determined to discriminate the pathological outcome from chemotherapy on the very first day after initial infusion (Roblyer et al. 2011). Confirmation of chemotherapy response this early during treatment could substantially minimize treatment burden and avoid ineffective chemotherapy.

This work aimed to address several unmet needs of existing breast cancer diffuse optical monitoring devices. First, previous designs typically deliver light to and from the patient using optical fibers. This type of design is often bulky, heavy, and fragile. Second, the optical probe or patient/device interface is typically rigid and poorly conforms to the natural shape of human tissue. This is limiting as it may be uncomfortable for the patient, especially during extended measurements. Third, for optical probes with limited number of light sources and detectors, a 2D mapping of tissue properties may require the probe head to be sequentially scanned over gridded positions on the skin (Roblyer et al. 2011). Therefore, data acquisition for each iteration may take 10s of minutes, and poor temporal and spatial resolution excludes the possibility of real time monitoring of tissue hemodynamics.

In order to address these limitations, a new wearable diffuse optical probe was designed and fabricated to investigate if very early timepoints during a patient's first NAC infusion are predictive of overall response (pCR versus non-pCR). These timepoints correspond to an already scheduled patient visit and have so far been unexplored for their prognostic value. A breath-hold was used to evaluate the vascular performance of breast and tumor tissue in normal volunteers and breast cancer patients as this hemodynamic challenge has been recently shown to be useful for monitoring NAC response (Flexman et al. 2013).

4.2 Methods

A wearable probe was designed to monitor locally advanced breast tumors during the course of neoadjuvant chemotherapy. Factors considered in the design include the

tissue depth and sizes of locally advanced breast tumors, the near infrared absorption and scattering properties of human breast tissue, and the anticipated changes expected to occur during a hemodynamic challenge, in this case a breath hold. Design choices and methods are described below.

4.2.1 Wavelength selection

The probe was designed to extract oxyhemoglobin (HbO₂) and deoxyhemoglobin (HHb) changes during a hemodynamic breath hold challenge. The choice of imaging wavelengths was determined in part by a condition number analysis previously shown to be useful for optimizing wavelength selection (Corlu et al. 2003). The condition number $\kappa(A)$ is defined as

$$\kappa(A) = \|A^{-1}\| \cdot \|A\| \quad (16)$$

where $A = \begin{pmatrix} \varepsilon_{\lambda_1}^{HbO_2} & \varepsilon_{\lambda_1}^{HHb} \\ \varepsilon_{\lambda_2}^{HbO_2} & \varepsilon_{\lambda_2}^{HHb} \end{pmatrix}$, and each element of the matrix are the optical extinction

coefficients for HbO₂ and HHb at the chosen wavelength pair. Optimized wavelength pairs correspond to a condition number closer to one. Dual wavelength pairs in the near infrared (NIR) wavelength band from 600 to 900 nm were tested using condition number analysis.

4.2.2 Optode Topology

The imaging probe was designed to measure the most prevalent tumor size ranges based on current epidemiological data, with a target range of 2 to 4 cm in diameter, which represent the 34 and 74 percentiles of locally advanced breast tumors sizes (Elkin et al.

2005). An overall probe diameter of 60 mm was chosen for all designs to accommodate a large range of tumor sizes.

The probe was designed with an array of optical sources and detectors; the surface topography of these components directly affects the probed tissue volume. Three optode topographies were considered and compared using Finite Element Method (FEM) simulations of a breast tumor hemodynamic challenge. The topographies are shown in Figure 4.1 and included a “12 pointed star” pattern, a “rectangular” pattern, and a “central rectangular” pattern. The “12-pointed star” pattern was an extension of our prior probe design which utilized a central hub with arms radiated outward (Teng et al. 2017). Both the rectangular and central rectangular topographies have been utilized in prior tomographic NIRS systems for neuroimaging applications (Khan et al. 2012; Perdue, Fang, and Diamond 2012; Eggebrecht et al. 2014; Li et al. 2016).

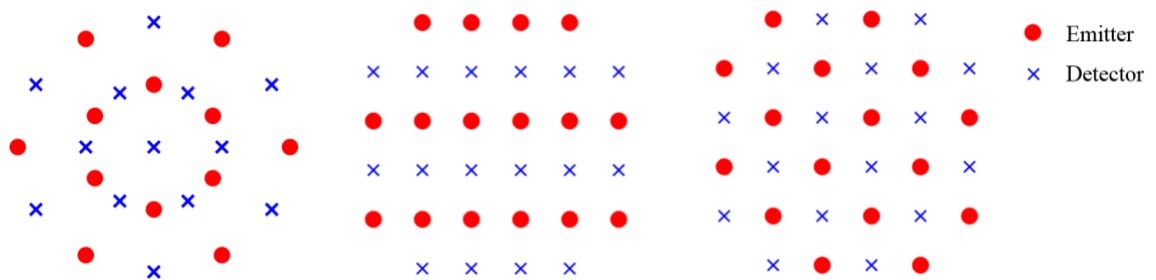


Figure 4. 1 Optode geometries. Left: 12-pointed star. Middle: Rectangular geometry. Right: Central rectangular geometry

Each probe optode topology was tested using Nirfast, a Matlab software suite that utilizes FEM for numerically solving the photon diffusion equation. A tumor-like inclusion was modelled on a homogeneous background and incremental increases and

decreases in the inclusion absorption were simulated to mimic the hemodynamic perturbations anticipated from a breath hold challenge. Figure 4.2 shows the simulation geometry. The background HbO₂ and HHb concentrations were set to 5.2 μ M and 15.6 μ M, respectively, and were based on previously reported healthy breast tissue properties (Shah et al. 2004). The inclusion was a 35 mm diameter sphere at a depth of 5 mm.

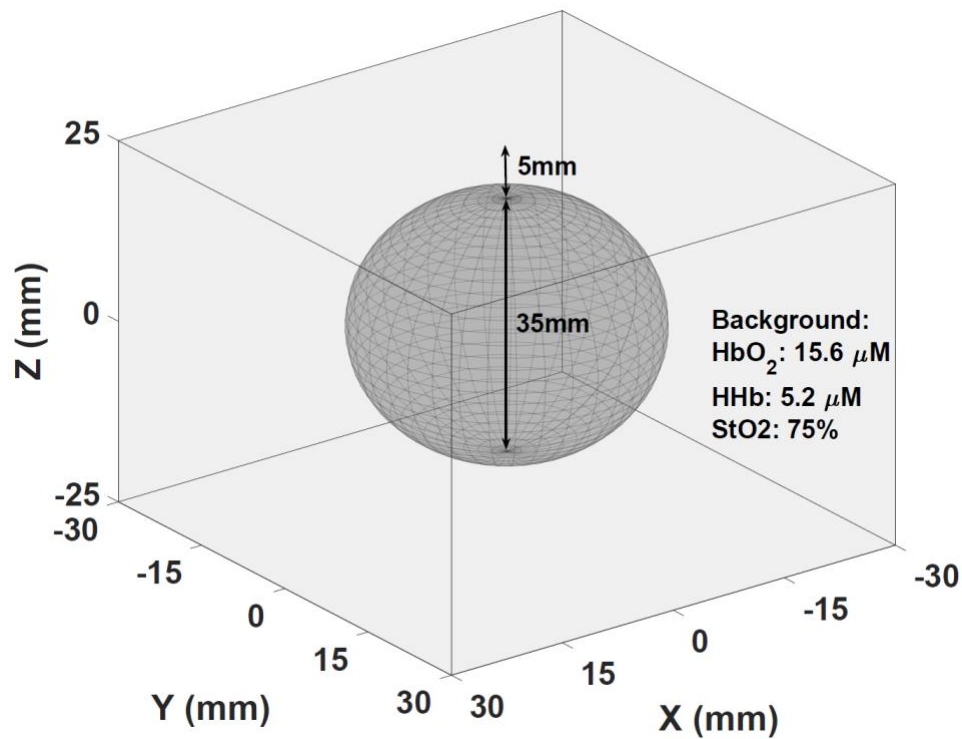


Figure 4. 2 Simulation geometry utilized for optode configuration comparisons. The inclusion mimics a 35 mm diameter breast tumor embedded in healthy breast tissue.

HbO₂ was incremented or decremented by 3, 6, 9 and 12 μ M and HHb was incremented or decremented by 1, 2, 3, or 4 μ M. The magnitude of these changes roughly corresponds to the documented changes of chromophore concentrations for locally advanced breast tumors on the day one after their initial NAC infusion (Roblyer et al. 2011). The

reconstructed changes in HbO₂ and HHb concentrations were compared with the ground truth for all simulations. Crosstalk between reconstructed HbO₂ and HHb was also evaluated. Scattering was assumed to be homogeneous and set to a wavelength-insensitive constant of 1 mm⁻¹ for all simulations.

4.2.3 Printed circuit board (PCB) design

The probe is shown in Figure 4.3. It was fabricated using a four-layer rigid-flex PCB design. Nine rigid PCB “islands” are connected through 0.9 mm flexible connections that allow flexion between rigid neighbors. The bottom copper layer (shown in Figure 4.3 (a)) is populated with several I²C compatible integrated circuits including an LED switch (MAX6964, Maxim Integrated), a bus buffer (PCA9600, NXP Semiconductors), and two analog multiplexers (MAX14661, Maxim Integrated). Additionally, MOSFET arrays (SSM6N43FU, LF, Toshiba) are used to sequential switch each LED. The middle layers of the PCB sit at the interface between the rigid and flexible substrates and facilitate trace routing.

The top copper layer (shown in Figure 4.3 (b)) is populated with 32 LEDs (qty 16 SMT750-23 and qty 16 SMT850-23, Roithner Lasertechnik) and 16 optical detectors (TSL250RD, ams). The LEDs are surface mount PLCC-2 packages with 750 nm and 850 nm center wavelengths. The detector is an 8-SOIC silicon photo detector module with a built in transimpedance amplifier, the maximum responsivity of this sensing module is $76.8mV/(\mu W/cm^2)$ at 770 nm.

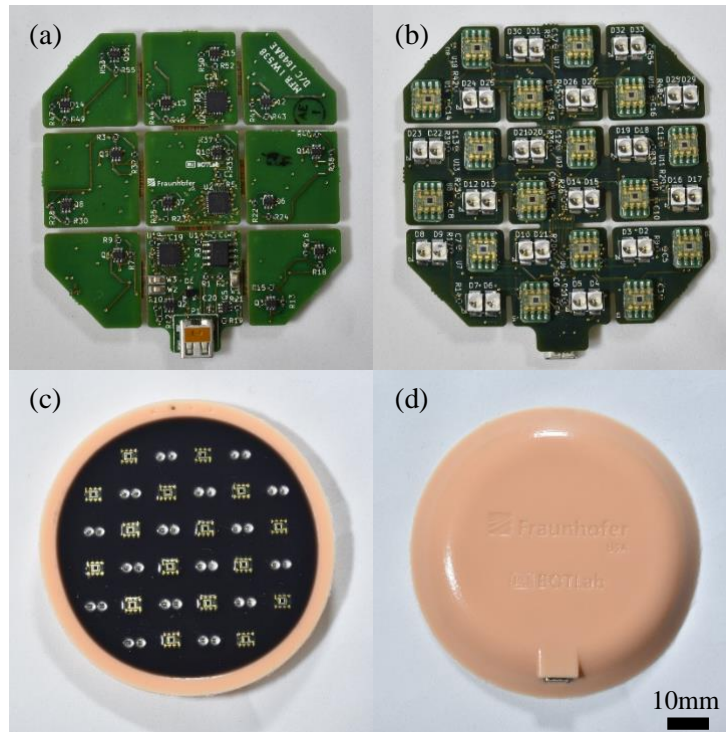


Figure 4. 3 (a) Bottom and (b) top view of rigid-flex PCB. (c) Top and (d) bottom view of the potted wearable probe.

The wearable probe communicates with a peripheral control box through a HDMI cable. LEDs and detectors are sequentially selected using I²C compatible multiplexers and microprocessors. Amplified photodiode voltage was measured with a 16-bit analog to digital converter (USB-6361 OEM, National Instruments).

4.2.4 Biocompatible probe housing

The probe is designed to conform to the curved surface of breast tissue, and is potted and cured in a medical grade silicone housing. Figures 4.3(c) and 4.3(d) show the top and bottom sides of the probe encased in housing. It is made with skin-safe silicone (Ecoflex 00-30, Smooth-On Inc.) and pigments (Silc Pig, Smooth-On Inc.). The silicone

and curing agent and mixed with the flesh color dye, vacuumed, transferred to a 3D printed mold, further vacuumed and then cured. A black silicone layer is used on the bottom surface of the probe to reduce light crosstalk from emitters to detectors. The optical emitters and detectors protrude from the silicone surface by approximately 0.3 mm and indent the soft tissue of the breast. The total dimension is 79.4 mm wide and 9.6 mm thick, and its overall weight is 41.8 grams. IV tape firmly secures the silicone probe over the curved surface of bust model as shown in Figure 4.4.

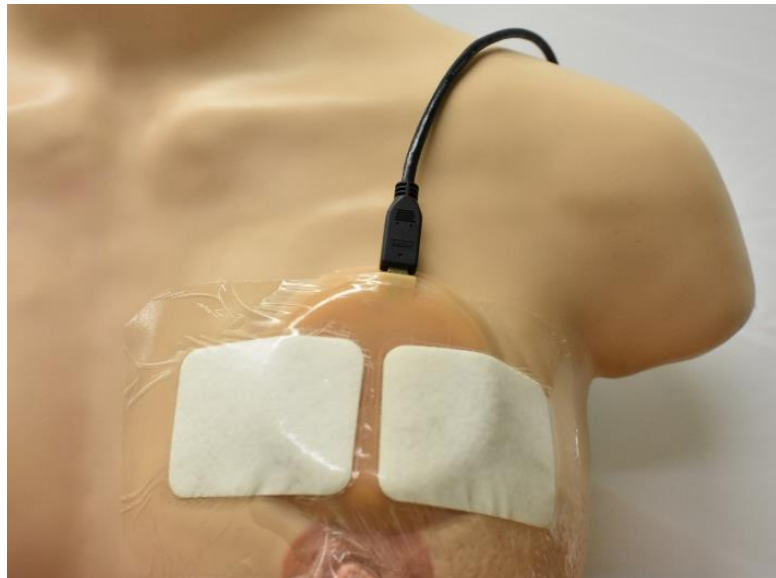


Figure 4. 4 Wearable probe attached to the curved surface of human bust model.

4.2.5 System characterization

The SNR of each source-detector optode pair was evaluated using a custom silicone tissue-simulating phantom. The optical properties of the phantom closely match reported healthy breast tissue values (Durduran et al. 2002; Shah et al. 2004). These optical properties were confirmed using a benchtop frequency domain diffuse optical

spectroscopy system (Torjesen, Istfan, and Roblyer 2017), and were measured to be:

$\mu_a = 0.0036 \text{ mm}^{-1}$ (750 nm), $\mu_a = 0.0026 \text{ mm}^{-1}$ (850 nm) and $\mu'_s = 0.9 \text{ mm}^{-1}$ (750 nm), $\mu'_s = 0.8 \text{ mm}^{-1}$ (850 nm).

The SNR of each optode was calculated as:

$$20 \cdot \log_{10} \left(\frac{V_b - V_d}{\text{std}(V_b - V_d)} \right)$$

where V_b and V_d are the mean of the DC voltage collected for phantom and dark measurements respectively. Dark measurements were taken with the LEDs off. All measurements were taken under ambient fluorescent lighting. A custom black rubber sheet was utilized to block light leakage from neighboring optodes for SNR measurements as they were taken on rigid flat phantom.

The system dynamic range was computed as a combination of the dynamic range of the 16-bit ADC (96 dB) and the operating range of the LEDs (26 dB). System precision was evaluated by computing the standard derivation of phantom measurement taken over a continuous two-hour period. The acquisition speed of the probe was determined by recording the time necessary to sequentially scan 408 optodes (the shortest source-detector optodes were excluded).

4.2.6 Channel phantom for simulated breath hold tumor hemodynamics

A dynamic channel phantom was fabricated to mimic an embedded inclusion (tumor) with changing hemoglobin levels. Figure 4.5 (a) shows the phantom geometry and Figure 4.5 (b) shows the fabricated phantom. This channel inclusion has a diameter

of 35 mm and it is 5 mm deep from the top air-phantom interface. These dimensions match the diameter of a common locally advanced breast tumor (Elkin et al. 2005). The solid silicone phantom was fabricated using titanium dioxide and nigrosin to control optical scattering and absorption respectively. Optical properties were validated using a frequency-domain diffuse optical spectroscopy system (Torjesen, Istfan, and Roblyer 2017). Measured reduced scattering coefficients are $\mu'_s = 0.78/mm$ and $\mu'_s = 0.67/mm$ at 750 nm and 850 nm, respectively. Measured absorption coefficients at the same wavelength pair are $\mu_a = 0.043/mm$ and $\mu_a = 0.0028/mm$.

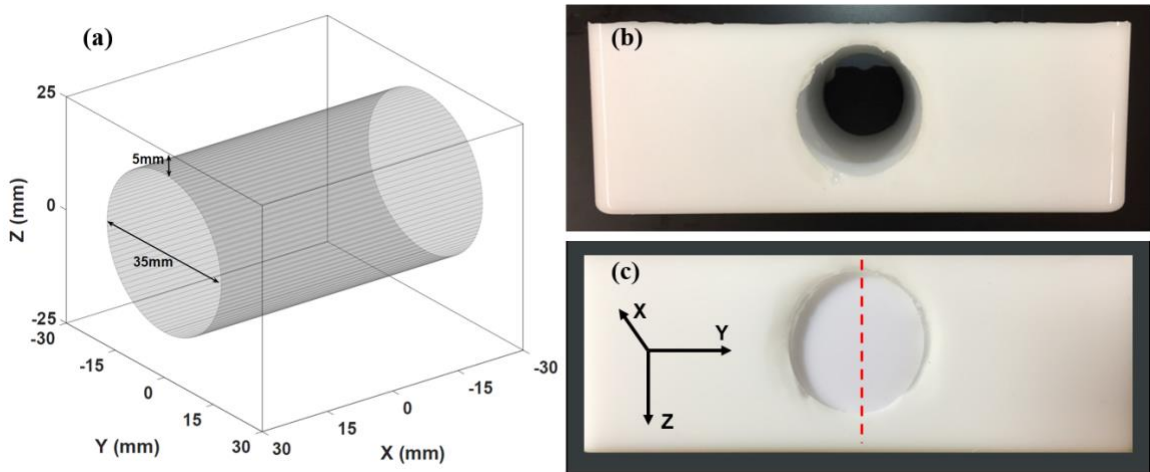


Figure 4. 5 (a) Channel phantom geometry. (b) Unfilled and (c) filled channel phantom.

The channel was filled with an intralipid-based liquid solution to mimic tumor optical properties as shown in Figure 4.5 (c). The liquid phantom utilizes a 20% fat emulsion which was diluted with deionized water to adjust optical scattering. Five different liquid phantom batches were prepared. The first was fabricated to match the

absorption and reduced scattering of the solid phantom. The others had 25%, 50%, and 100% increases in μ_a . These five batches were sequentially filled and drained from the channel and used to validate the ability of the wearable probe to detect changes in depth resolved optical absorption.

4.2.7 Normal volunteer breath hold study

All human subject measurement procedures were approved by Boston University institutional review board. A set of two wearable probes were placed on the top half of each breast of each volunteer (one probe per breast). The two probes were placed in mirror symmetry, and each was secured with an intravenous transparent dressing. A female volunteer was recruited to perform three repeat breath holds. Each breath hold measurement consisted of a 30 second system warm-up, followed by five iterative dark measurements, then one minute of baseline measurements, 30 seconds of breath hold measurements, two minutes of breath release measurements, and then at least two minutes of rest before the next breath hold.

4.2.8 Rise time and fall time calculations during breath hold

The human measurement protocol was designed to measure a hemodynamic breath hold challenge in breast tumors. Prior work has demonstrated that changes in HHb concentration during the course of breath hold and release can be described in terms of modified RC circuit step response functions as shown in here: (Flexman et al. 2013)

$$f(t) = \begin{cases} \frac{t}{t_p} \cdot \frac{1 - e^{-\frac{t}{t_r}}}{1 - e^{-\frac{t_p}{t_r}}} & t \leq t_p \\ e^{-\frac{t-t_p}{t_f}} & t > t_p \end{cases} \quad (17)$$

where t_p corresponds to the time when a maximum positive change in HHb occurs and t_r and t_p are the rise and fall time of this piecewise function. Normal volunteer data collected as part of this study were fit to these functions. The rise and fall time coefficients were fitted using the built in Trust-Region algorithm in MATLAB, with initial values chosen at 10.

4.2.9 Effect of system acquisition speed on the accuracy and precision of fall time calculations

The maximum acquisition speed of two wearable probes operating in tandem is approximately 0.2 Hz. This speed was determined by taking 408 unique optode measurements per probe. Finite switching, settling, and acquisition times for each optode contribute to this measurement rate. As one of the goals of the study was to extract fall times from breath hold data, an analysis was conducted to ensure that this acquisition rate provides both accurate and precise extractions. Simulated rise and fall HHb time traces were generated using Equation 17. Previously reported fall time coefficients were utilized for different breast tissue types; healthy tissue: 15s; benign: 25s; malignant: 30s (Flexman et al. 2013). The simulated data corresponded to a 1 Hz sampling rate, and was downsampled to 0.5 Hz, 0.33 Hz, 0.2 Hz, and 0.1 Hz to simulate slower acquisition rates.

Gaussian white noise (GWN) was added to the simulated data sets. Noise characteristics were estimated by fitting an experimentally measured HHb healthy volunteer data set collected at 3 Hz using an earlier low-optode density probe prototype to equation 17 (Teng et al. 2017). The standard deviation of the fit residuals was used as the standard deviation of the GWN and 1000 separate noise sets were generated. Each set added to the simulated time trace data, and rise and fall times were extracted. The distribution of these fit time constants was then determined at different acquisition rates to evaluate how lower sampling rates degrade fall time extraction accuracy and precision.

4.2.10 Tomographic reconstructions

Tomographic reconstructions were conducted for both phantom and healthy volunteer data. The first order optodes were excluded for all reconstructions due to signal saturation, leaving 408 optical channels for every measurement. Channels with signal levels less than 10 dB above the noise floor were excluded from image reconstruction. The Rytov approximation was used for all reconstructions, and is shown here:

$$\Phi = \Phi_0 \cdot \exp(\delta\theta) \quad (18)$$

where Φ_0 and Φ indicate the fluence rate measured with baseline and perturbed optical properties, respectively. For iterative measurements, the perturbation of media optical properties from the k th to the $k+1$ th measurement leads to the following expression:

$$\delta\theta = \ln\left(\frac{\Phi_{k+1}}{\Phi_k}\right) \quad (19)$$

The ratio of fluence rates can be replaced with the ratio of measured voltages:

$$\delta\theta = \ln\left(\frac{V_{k+1}}{V_k}\right) \quad (20)$$

$\delta\theta$ is linearly correlated with spatial variations in media optical properties:

$$\ln\left(\frac{V_{k+1}}{V_k}\right) = J_k \cdot \Delta\mu_k \quad (21)$$

where $\Delta\mu_k$ represents the change in a media optical property, and J is the Jacobian matrix, which describes the mapping of media optical property changes to surface measurements.

Assuming μ'_s is time-invariant, the elements of J are expressed as:

$$J_k = \begin{pmatrix} \frac{\partial \ln \Phi_1}{\partial \mu_1} & \frac{\partial \ln \Phi_1}{\partial \mu_2} & \dots & \frac{\partial \ln \Phi_1}{\partial \mu_j} \\ \frac{\partial \ln \Phi_2}{\partial \mu_1} & \frac{\partial \ln \Phi_2}{\partial \mu_2} & \dots & \frac{\partial \ln \Phi_2}{\partial \mu_j} \\ \vdots & \vdots & \dots & \vdots \\ \frac{\partial \ln \Phi_i}{\partial \mu_1} & \frac{\partial \ln \Phi_i}{\partial \mu_2} & \dots & \frac{\partial \ln \Phi_i}{\partial \mu_j} \end{pmatrix}$$

where i and j indicate the optode pair and node inside the simulation volume.

Reconstruction of the subsurface optical property changes requires calculating the pseudoinverse of J_k , which can be expressed as

$$J_k^+ = (L^{-1})^T (\tilde{A}^T \tilde{A} + \alpha \cdot \text{diag}(\tilde{A}^T \tilde{A}))^{-1} J_k \quad (22)$$

where $\tilde{A} = J_k \cdot L$, and L is the Tikhonov regularization matrix (Boas, Gaudette, and Arridge 2001; Eggebrecht et al. 2014). The changes in the media optical properties can then be computed as:

$$\Delta\mu_k = J_k^+ \cdot \ln\left(\frac{V_{k+1}}{V_k}\right). \quad (23)$$

4.3 Results

4.3.1 Wavelength selection

Figure 4.6 shows the results of the condition number analysis for different wavelength pairs. A black-dashed contour line is shown for a relatively small condition value of $10^{1/2}$. 750 nm and 850 nm LEDs were chosen for the wearable probe based on their relatively small condition number (3.1) as well as commercial availability.

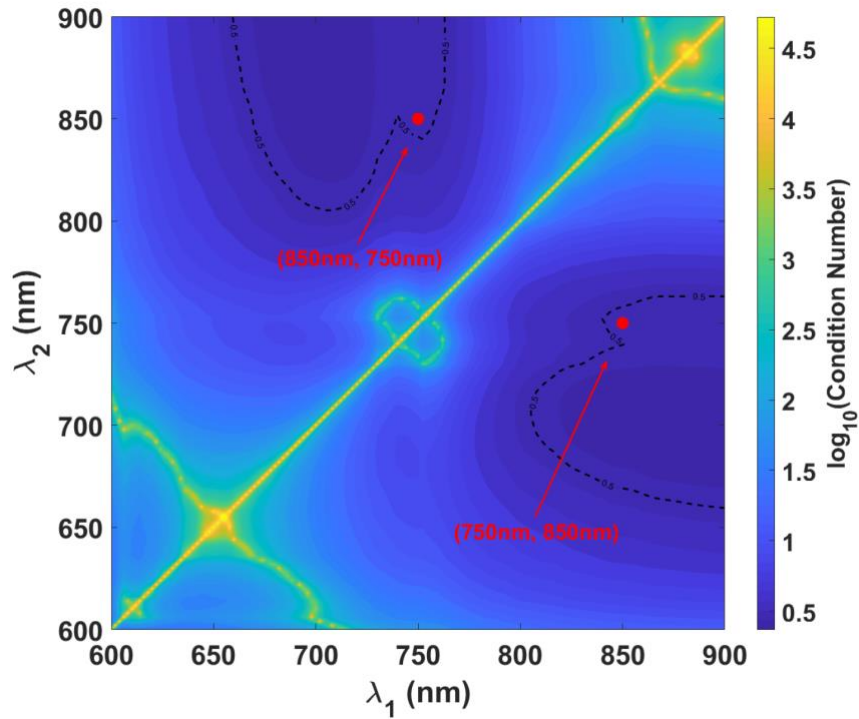
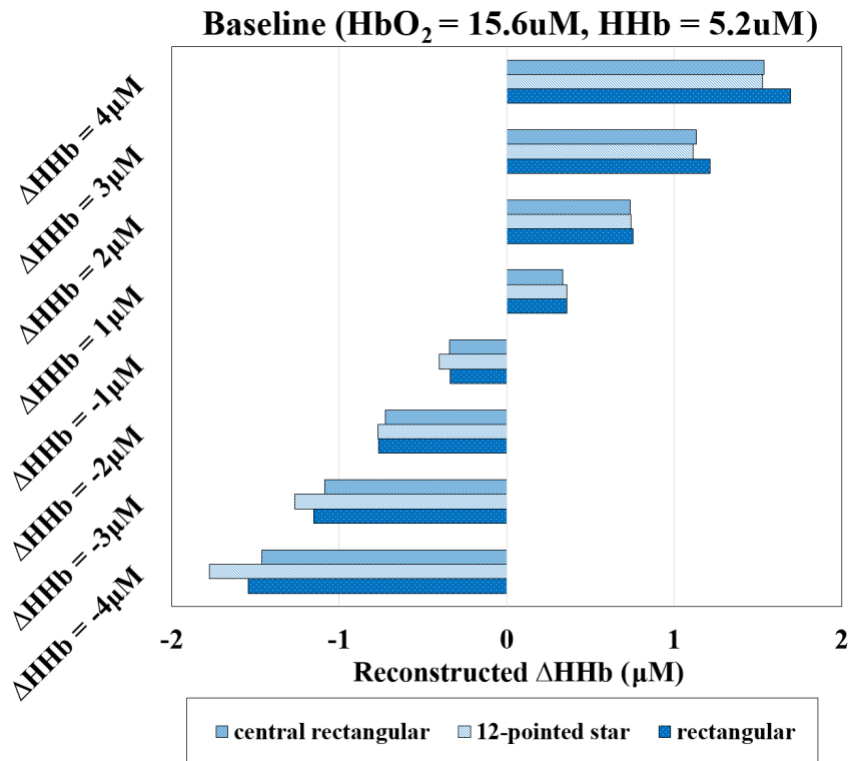


Figure 4. 6 Condition numbers associated with wavelength pair selections. The dashed isoline indicates $10^{0.5}$. The condition number corresponding to 750 nm and 850 nm is shown with the red dot markers.

4.3.2 Optode geometry validation

Reconstructed chromophore changes were calculated within the 3D inclusion volume for FEM simulations conducted with each optode geometry. Results are shown in Figure 4.7. Results were similar for each geometry with 35% to 40% of target changes recovered. A 6 – 12 % crosstalk was observed between HHb and HbO₂. The “central rectangular” pattern was chosen for the probe design because of the equivocal simulation results and because of its relative ease of fabrication. This design has 7 source-detector separation orders, ranging from 10.0 to 53.9 mm. There is a total of 512 separate optodes (i.e., source-detector pairs).



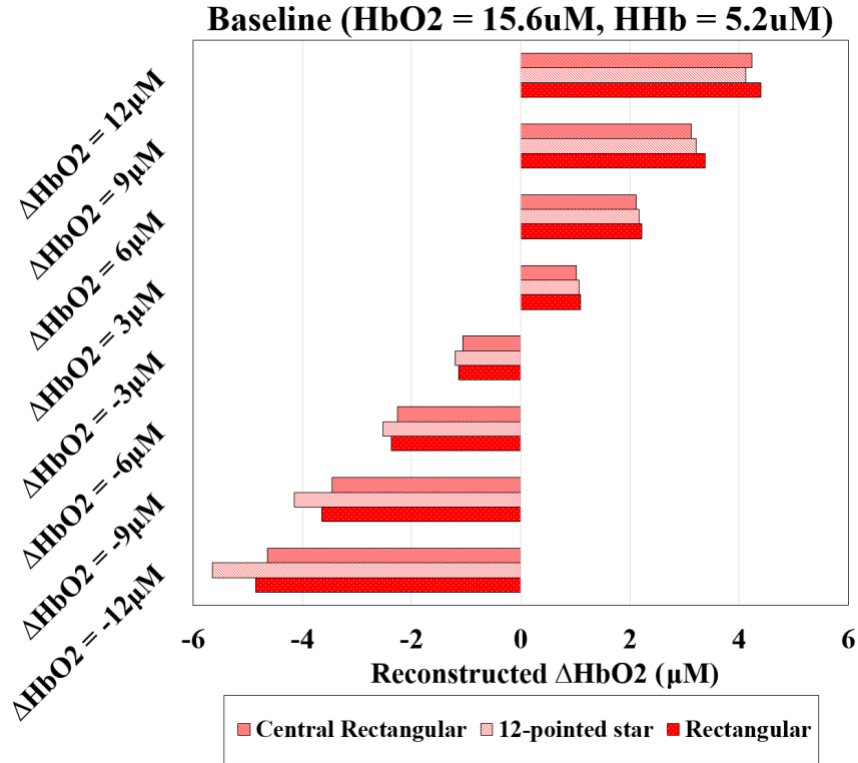


Figure 4. 7 Tomographic reconstruction results from various simulated chromophore perturbations in an embedded inclusion (tumor). Simulation ground truth is indicated on the y-axes and reconstructed values are indicated on the x-axis.

(a) Reconstructed changes in HbO₂ and HHb for perturbations in HHb. (b)

Reconstructed changes in HbO₂ and HHb for perturbations in HbO₂.

4.3.3 System performance

SNR results are shown in Figure 4.8. LED forward current was reduced for the shortest optodes to avoid saturation. SNR was at least 29 dB for all separations. At each separation, SNR varied by as much as 20 dB, likely due to differences in optical coupling between the optical transducers and phantom.

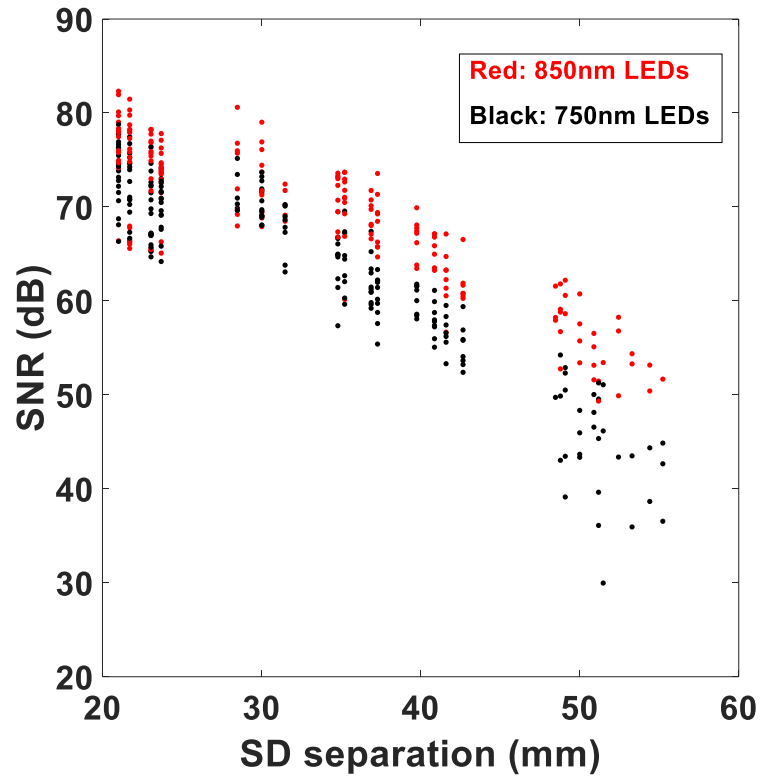


Figure 4. 8 Signal to noise for probe source-detector separations.

Other system characteristics are shown in Table 4.1. Thermal characteristics and accuracy are cited from our prior work (Teng et al. 2017).

Dimensions	
Diameter	79.38 (mm)
Thickness	9.56 (mm)
Optodes	
Wavelength	750/850 (nm)
Total Amount	512
Orders of Optodes Separation	7
System Characteristics	
Dynamic Range	122 (dB)
Acquisition Speed (maximum ratings)	0.45 (Hz)
Overall Precision	1.01 (%)
Accuracy*	< 5 (%)
Thermal Effect*	0.29 (%/°C)
* values cited from Teng <i>et al.</i> , 2017	

Table 4. 1 System characteristics of high density wearable imaging system

4.3.4 Channel phantom results

Figure 4.9 shows $\Delta\mu_a$ reconstructions from the channel phantom for experimental μ_a increases of 25%, 50% and 100% from baseline. The X-Z plane through the center of

the channel is shown. The % of target $\Delta\mu_a$ is indicated by the colorbar and by labeled isolines. Optical property changes up to 4.0 cm in depth can be detected when a threshold of 10% of target $\Delta\mu_a$ is utilized. It is of note that the accuracy of reconstruction degrades for larger $\Delta\mu_a$, which is expected for Rytov approximation (Bigio and Fantini 2016). These results indicate the wearable probe is capable of detecting subsurface μ_a perturbations that are of the same magnitude as those anticipated during a breath hold challenge.

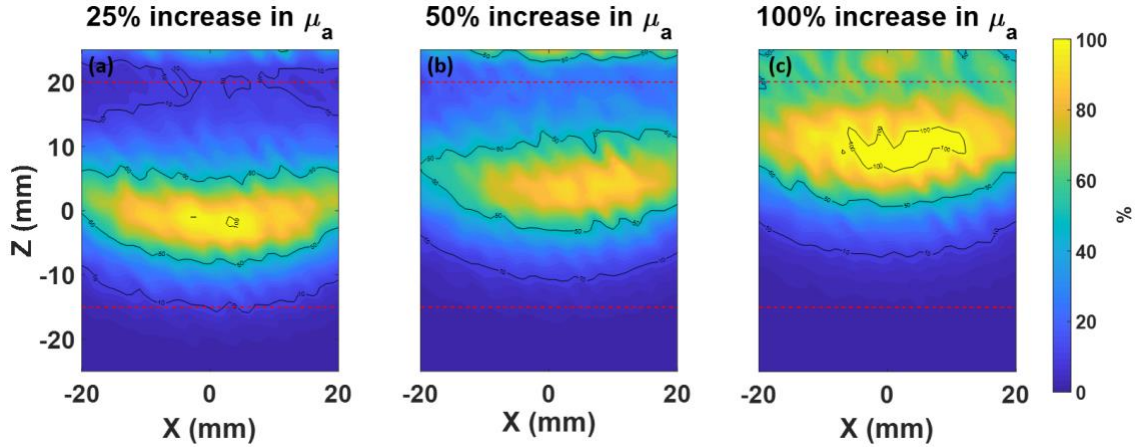


Figure 4. 9 $\Delta\mu_a$ reconstructions using the Rytov approximation. Changes in μ_a are shown in the X-Z plane through the center of the channel. The color bar and isolines indicate the % of target $\Delta\mu_a$ reconstructed. The same regularization parameter, $\alpha = 1$, was used for all three reconstructions.

4.3.5 Fall time analysis

Figure 4.10 shows the relationship between probe acquisition speed and fall time coefficient extraction accuracy and precision for healthy breast (black), benign breast lesions (blue), and malignant breast (red) tissue types. Downsampling had a negligible

effect on overall accuracy. However, reduced acquisition speed degraded the precision of fall time extractions. Extraction uncertainties were as large as 27% at 0.1 Hz.

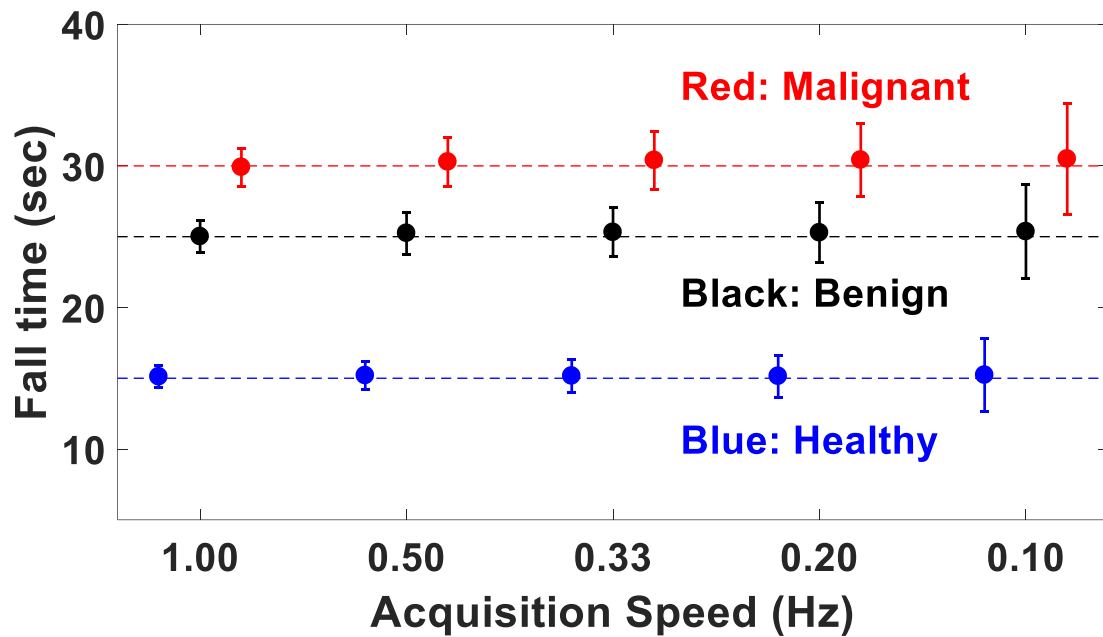


Figure 4. 10 HHb fall time extraction accuracy and precision with respect to probe acquisition speeds.

Figure 4.11 shows the effect of reducing the probe acquisition speed on the theoretical ability to separate benign tissue from malignant tissue. An area under the curve (AUC) of more than 0.9 was maintained until the acquisition speed was reduced to less than 0.2 Hz. The accuracy, precision, and ROC analysis strongly suggest that an acquisition rate of 0.2 Hz is sufficient for capturing fall time hemodynamics.

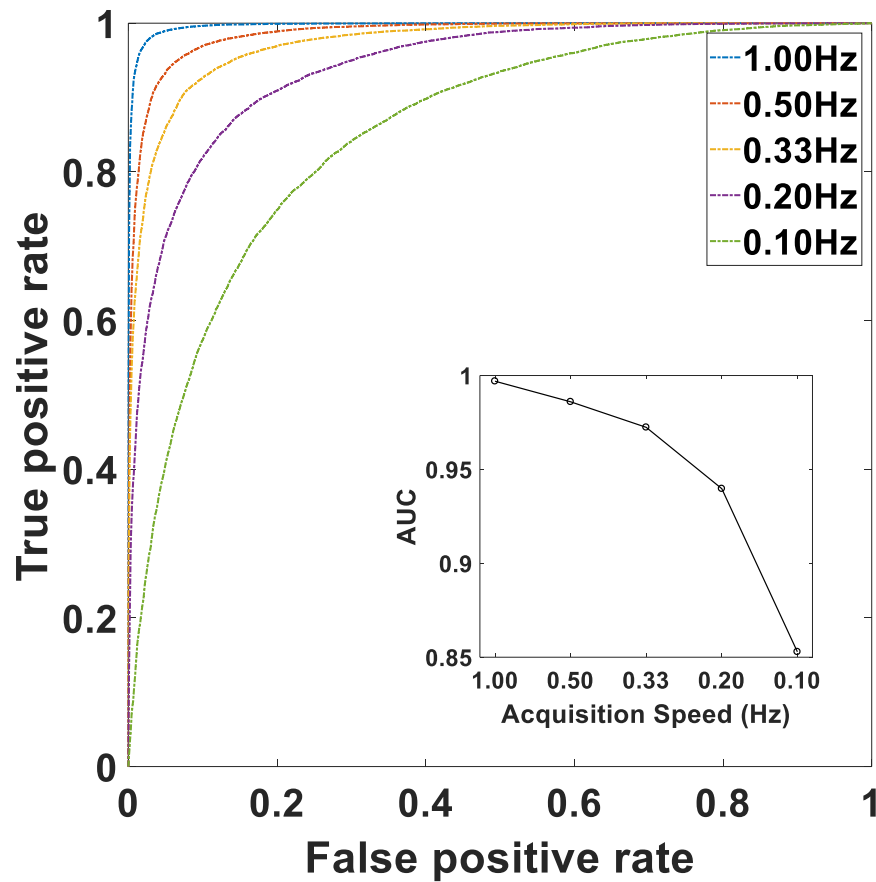
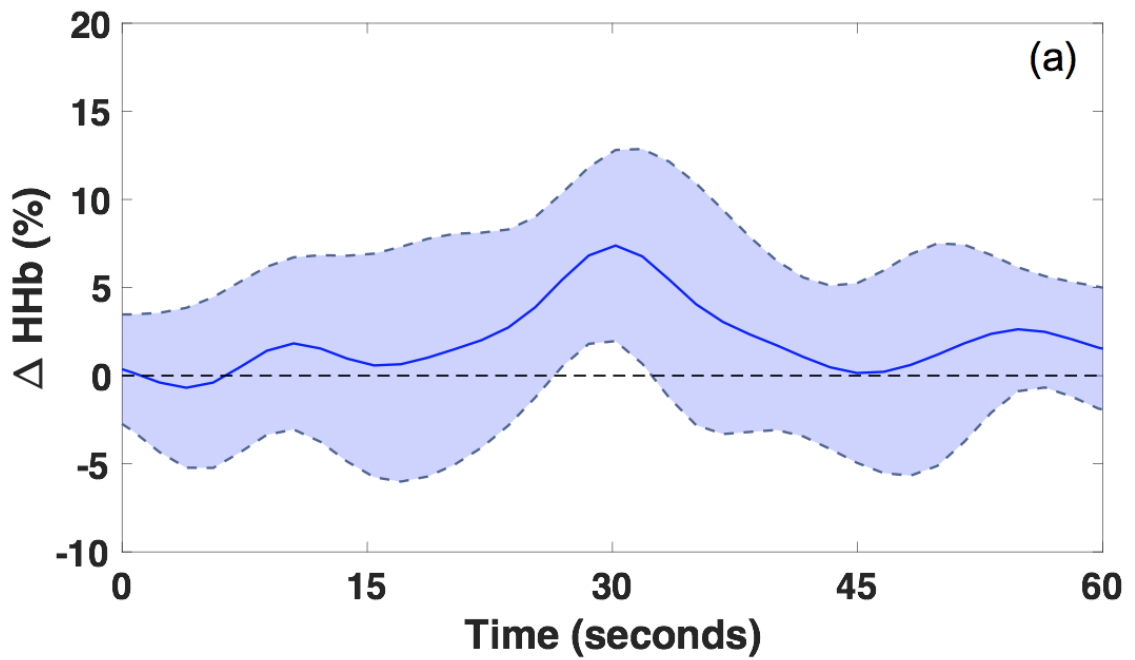


Figure 4. 11 ROC curve analysis for differentiating benign and malignant tissue types based on fall times in a simulated system as acquisition speeds are reduced from 1 Hz to 0.1 Hz.

4.3.6 Normal volunteer results

Figure 4.12 (a) shows the moving average of HHb changes for a female normal volunteer as she took a 30 second breath hold. After 60 seconds of baseline measurements, the subject stopped gas exchange, which accordingly led to higher HHb concentrations due to tissue oxygen consumption and vessel dilation. The maximum change of HHb for this subject reached 7.4 % when assuming a baseline HHb

concentration of $6.9 \mu M$, which has been previously reported for pre-menopause breast tissue (Shah et al. 2004) Our result indicates a reasonable match with previous published results shown in Figure 4.12 (b) (Flexman et al. 2013), in terms of the initial enhancement during breath hold period, the normalized maximum changes in deoxyhemoglobin concentration from baseline, and the washout rate in the first 15 seconds of breath release period.



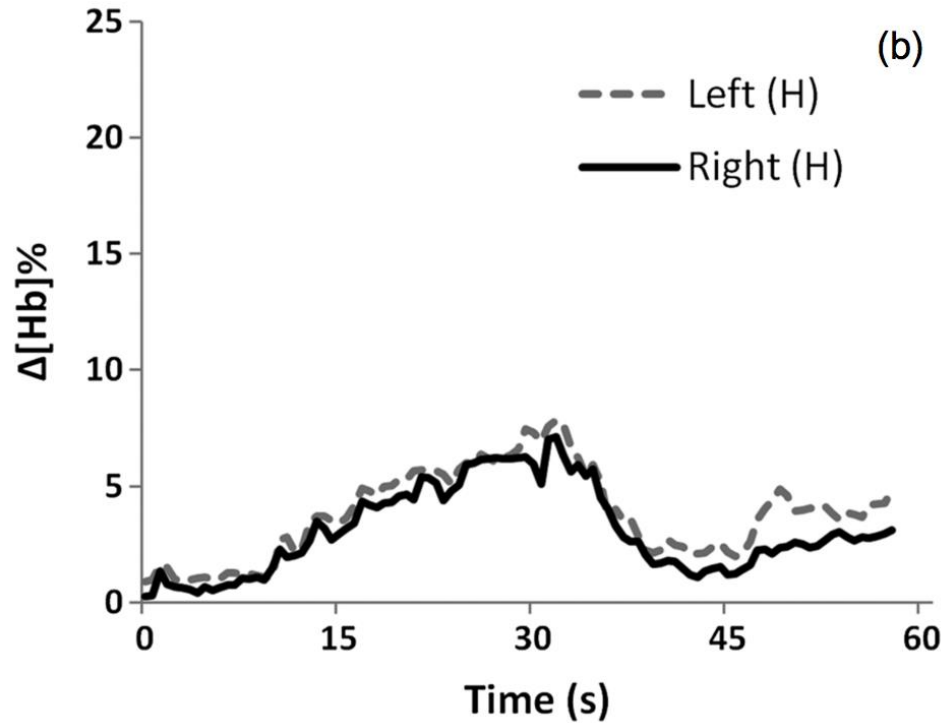


Figure 4. 12 HHb concentration changes in healthy breast tissue during breath hold challenge. (a) Results from the wearable optical probe at Biomedical Optical Technologies Lab at Boston University, (b) results adapted from Flexman’s study at Columbia University

4.4 Discussion

This work introduced a high optode density, deep-tissue, and wearable imaging system designed for monitoring breast cancer patients during presurgical chemotherapy. Characterizations and validations of this prototype were performed with numerical simulations, solid and liquid tissue-simulating phantom measurements, and a healthy human subject measurement.

The system was characterized with a bevy of *in vitro* and *in vivo* tests. For example, measurements on a breast-mimicking silicone phantom revealed high precision (1.01%) and high signal quality. Additionally, the ability of the wearable probe to extract changes in absorption in an embedded inclusion was tested with a channel phantom. The results indicate highly accurate optical property reconstruction absorption perturbation as large as 50% of baseline. It should be noted, however, that the *in vitro* validation experiments in this work may have oversimplified the heterogeneity of tumor-bearing breast tissue. The inclusion used for our studies was regular and homogeneous, whereas tumors may have a hypoxic core with an irregular and proliferating periphery. Discrepancies between the assumed and the actual tissue geometry may affect reconstruction accuracy.

In vivo validation of the wearable imaging system was implemented through breath hold measurement with a healthy female subject. Previous studies have suggested that breath hold induced tissue hemodynamics may be indicative of LABC patients' response to NAC. Although the physiology of breath hold is far from being comprehensively understood, the fundamentals of gas exchange physiology between alveoli and capillaries have been well studied (Parkes 2006), as the diffusion of oxygen and carbon dioxide molecules is driven by the gradient of partial pressure between alveoli and the capillaries. Breath hold prevents gas renewal at alveoli, so that the partial pressure difference between alveoli and capillaries is gradually reduced. This brings down the exchange efficiency for both gases, which should have caused reduced tissue oxygen saturation. However, increased amount of carbon dioxide strongly dilates the

vessels, which accordingly increases tissue blood volume. Therefore, within breath hold period, these two effects will promote the concentration of deoxyhemoglobin and competing each other on the concentration of oxyhemoglobin. Measured tissue hemodynamic results confirmed this theoretical background, and the same observations were seen in previously published findings (Flexman et al. 2013; Gunther et al. 2018).

The wearable probe had several limitations. For example, the acquisition speed could be increased to achieve finer temporal resolution of 3D tissue hemodynamics. The system is currently limited due to sequential scanning of measurement channels, and the settling time between successive optodes. An additional limitation is the current inability to dynamically change the LED forward current during measurements. This limits the use of optodes with the shortest and longest source detector separation due to saturation and low signal respectively.

In the future, a normal volunteer study with larger sample size is planned to better validate the performance of this wearable system in monitoring breath hold hemodynamics. Promising results from normal volunteer study will lead to breast cancer monitoring to LABC patients in the clinical setting.

To the best of our knowledge, this CW imaging system is the first demonstration of a wearable device on female breast tissue for rapid hemodynamic monitoring during breath hold challenge. It targets the first hours of neoadjuvant chemotherapy and holds potential to feedback real time treatment response.

CHAPTER 5. SUMMARY AND FUTURE DIRECTIONS

5.1 Summary

The major contribution of this work lies in design and fabrication of a clinic-ready wearable physiological sensing device for breast cancer monitoring. This device not only has the potential to explore an uncharted domain in clinical monitoring devices (i.e. continuous measurements during treatment), but also provides a more patient-friendly and economical imaging method for tumor hemodynamics monitoring.

In terms of hardware development, this work began with optical transducer selection, and evaluated the feasibility of electronics design using rigid PCBs. The electronics design was then improved and electric and optical components were migrated to a flexible PCB. The probe was accompanied by a silicone housing and was designed to adapt to the curvature of human breast. Based on the design experience from first two iterations of probes, a final generation probe was fabricated that featured a much higher density of optical transducers, and more versatile optical channel switching electronics. Additionally, the supporting electronics were miniaturized and integrated into an electrical enclosure.

Custom software was also developed to operate the probe. The probe described in Chapter 3 was equipped with software that provided real-time feedback of tissue hemodynamics. The probe described in chapter 4 included an interactive user-interface that provided instructions and feedback to normal volunteers measured during breath holds.

In terms of system characterization, this work analyzed the signal quality, system

precision and accuracy in both *in vivo* and *ex vivo* experiments, and also demonstrated system performance in human volunteers. The wearable imaging system was successfully used to monitor fast tissue hemodynamics during cuff occlusion and breast holds. Results were in agreement with previous studies exploring these same hemodynamic challenges.

In terms of physiological data processing, this work utilized 2-D and 3-D reconstruction methods of tissue optical and functional properties using analytical and numerical models. Tomographic simulations and measurements helped to guide the design of the optical transducer array during the system hardware development phase.

Together, these results support the feasibility of breast tumor hemodynamic monitoring with this new wearable optical probe.

5.2 Future directions

Several future directions of this project are described below. The first relates to the clinical application, and the others relate to system hardware improvements.

In the near future, it is anticipated that the clinical-ready prototype will be transferred to the clinical and used to perform wearable tissue imaging in LABC patients during the course of chemotherapy infusions. This will validate the ability to perform real-time monitoring of tumor hemodynamics, and potentially further confirm our previous finding that oxyhemoglobin flare occurs in pathologically responsive patients (Roblyer et al. 2011).

The wearable device is limited by several system constraints that could be addressed in the future. The first related to the footprint of light sources and detectors. The current LEDs are in PLCC-2 packages; each one has a single LED chip. As shown in

figure 3.1, two separate LED packages are required for the current system. In the future, a single PLCC-4 package containing two LEDs could be used reduce the footprint of light source by 50%.

The second hardware limitation is the electrical bandwidth of the CW imaging system. The system described in chapter 4 currently uses DC (non-modulated) light sources. Modulation is desired as it helps to eliminate pink noise. The rise time and fall time of the current photodiode sensing module are on the order of hundreds of microseconds, supporting modulation in the kHz range. It is possible that modulation in this range may limit or reduce the overall data acquisition rate as sample lengths need to be sufficient to capture the AC amplitude of the modulated signal. In the future, an optical detector with faster response may allow for modulated light detection without compromising acquisition speed.

A third hardware limitation is related to the removal of motion artifacts. Future probe designs may take advantage of ICs that provide motion data of a subject under study. For example, Figure 5.1 shows a multi-chip module consisting of two dies integrated into a single QFN package. One die houses the 3-Axis gyroscope and the 3-Axis accelerometer. Motion artifacts identification and removal from optical sensing data could be allow higher accuracy with the wearable probe.

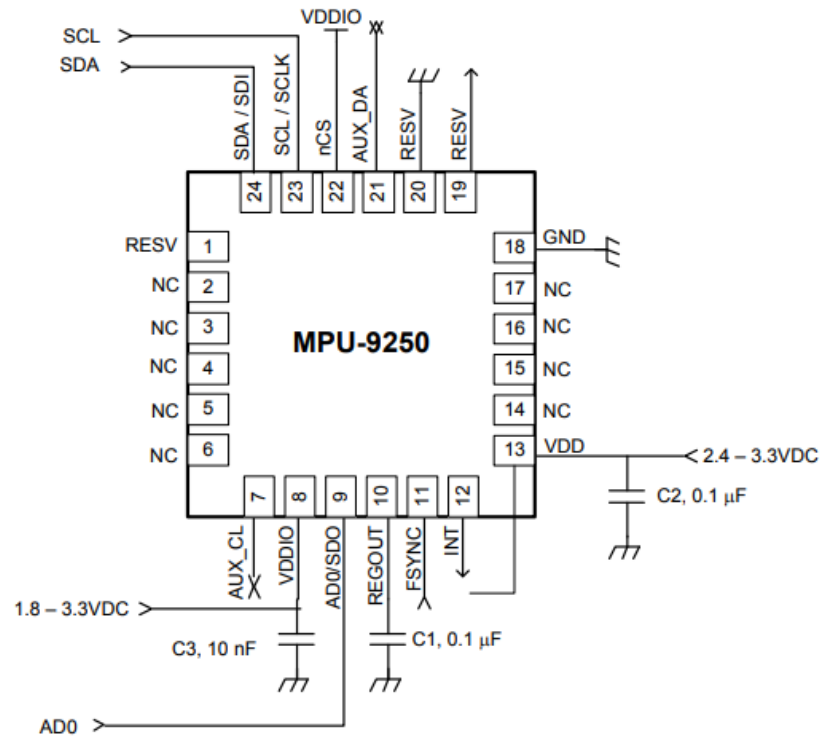
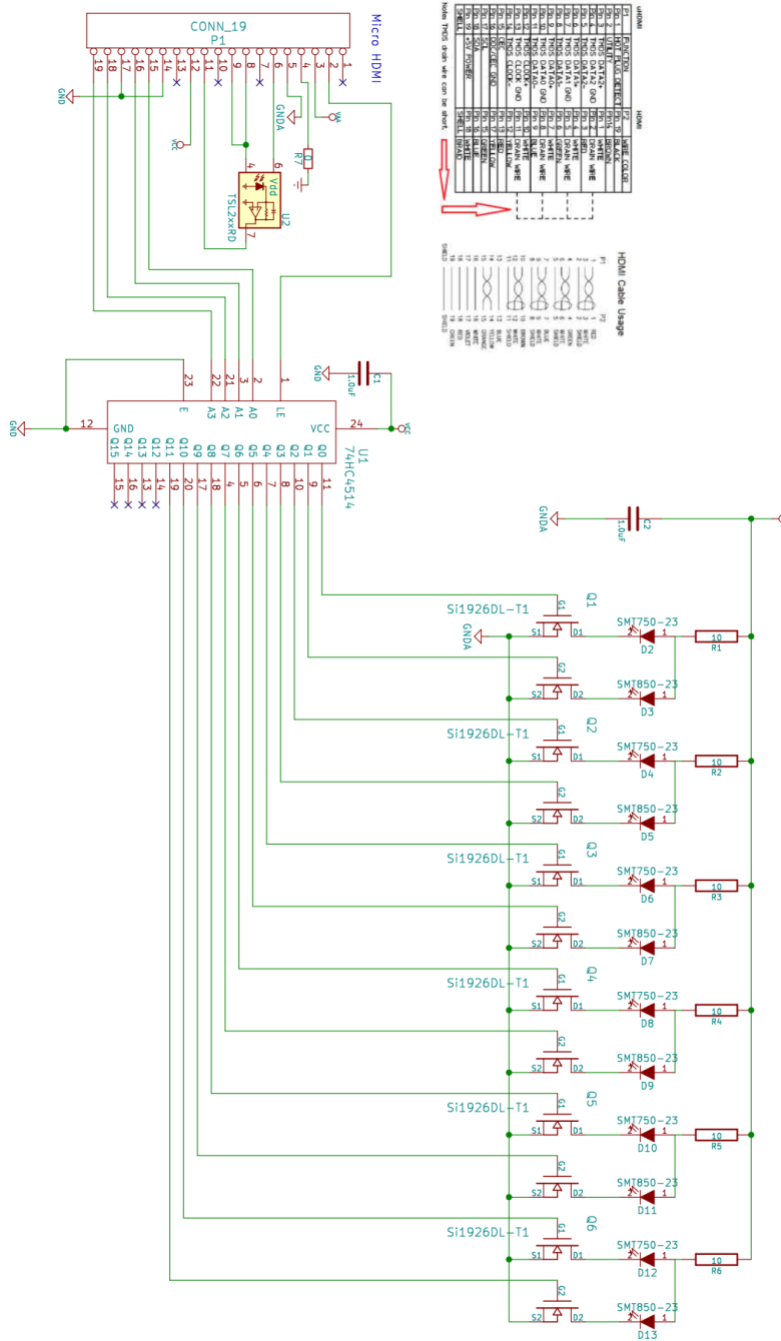


Figure 5. 1 MPU-9250 QFN application schematic for I²C operation

APPENDIX

1. Gen2 – Wearable Electronics Design

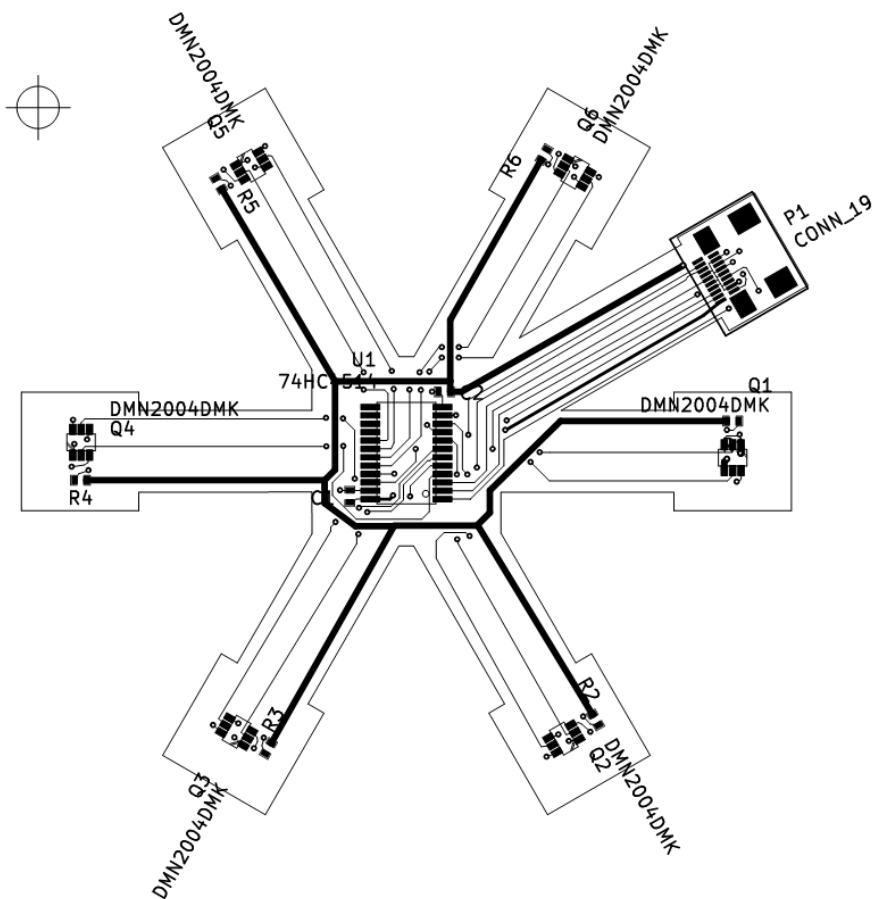
1.1 Schematic capture



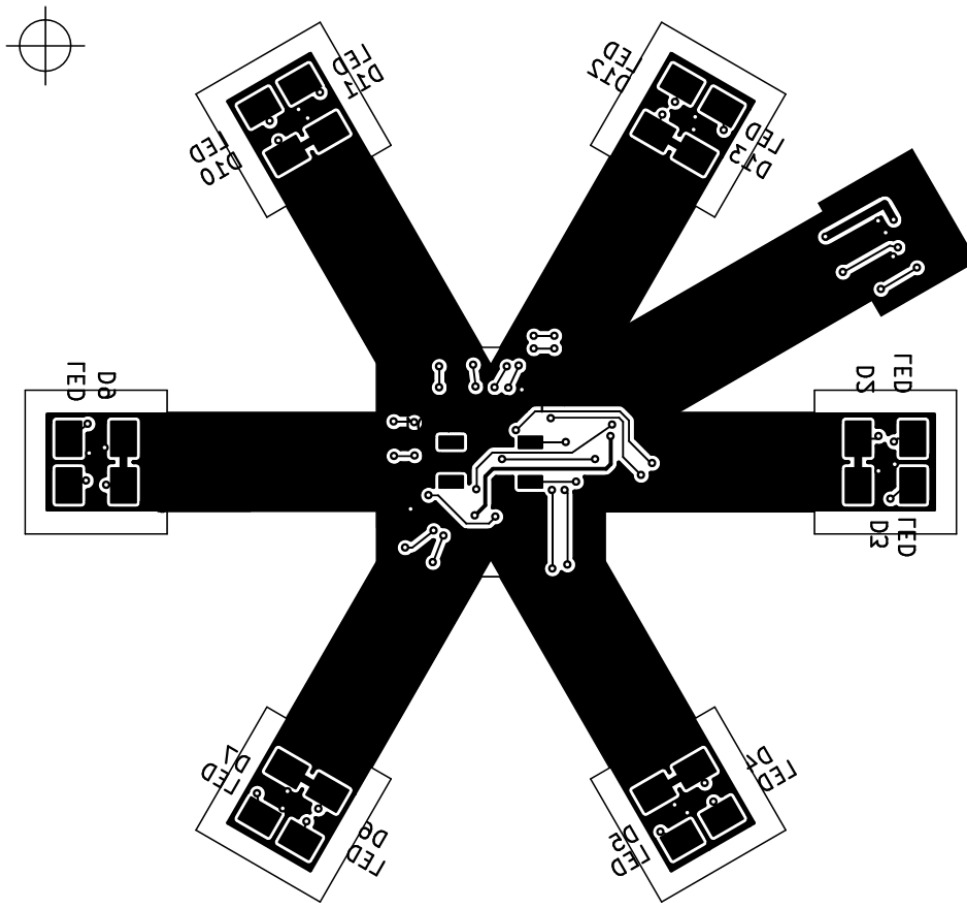
1.2 PCB stack-up



1.3 PCB layout (Top layer)



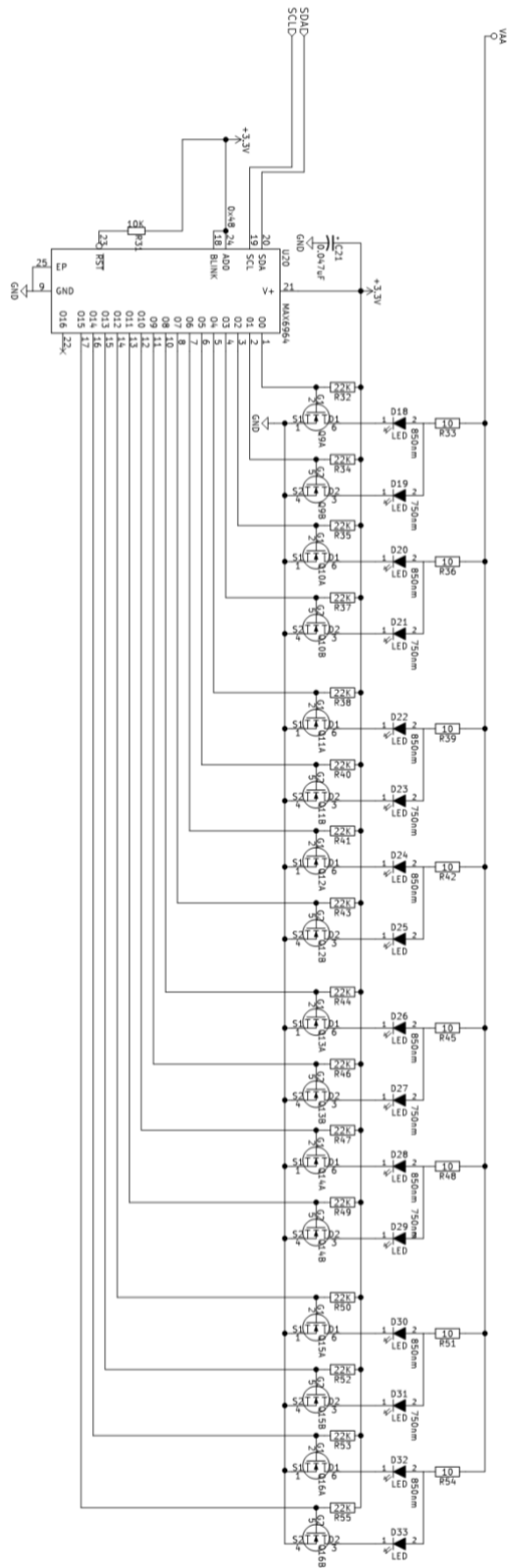
1.4 PCB layout (Bottom layer)

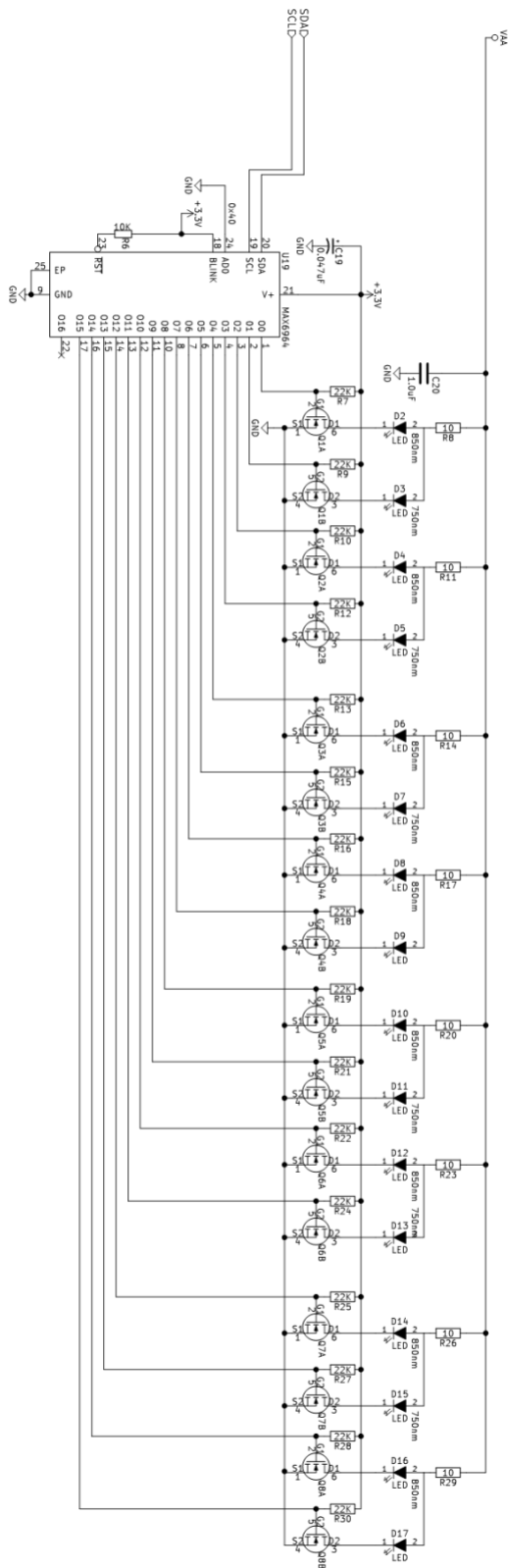


1.5 Contributions

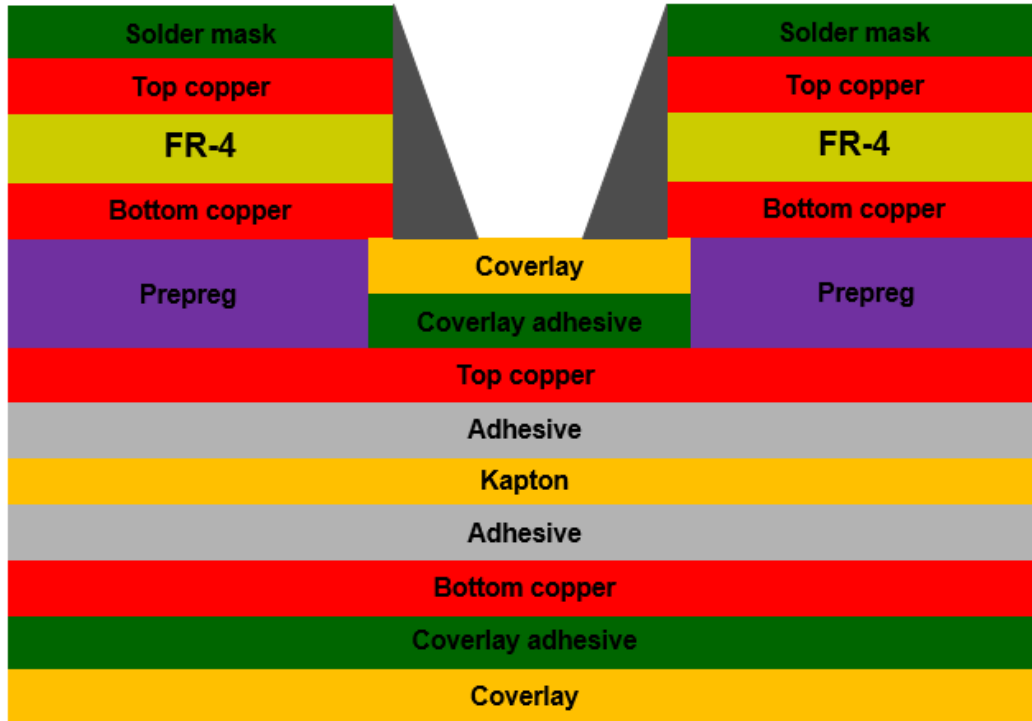
This CAD design comes from joint collaboration from BOTLab and Fraunhofer CMI, USA. BOTLab contributed to the schematic capture, component selection, circuit test and troubleshooting. Fraunhofer transferred the schematic design from ExpressPCB to KiCad, and contributed to flexible circuit layout.

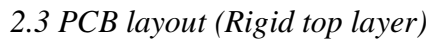




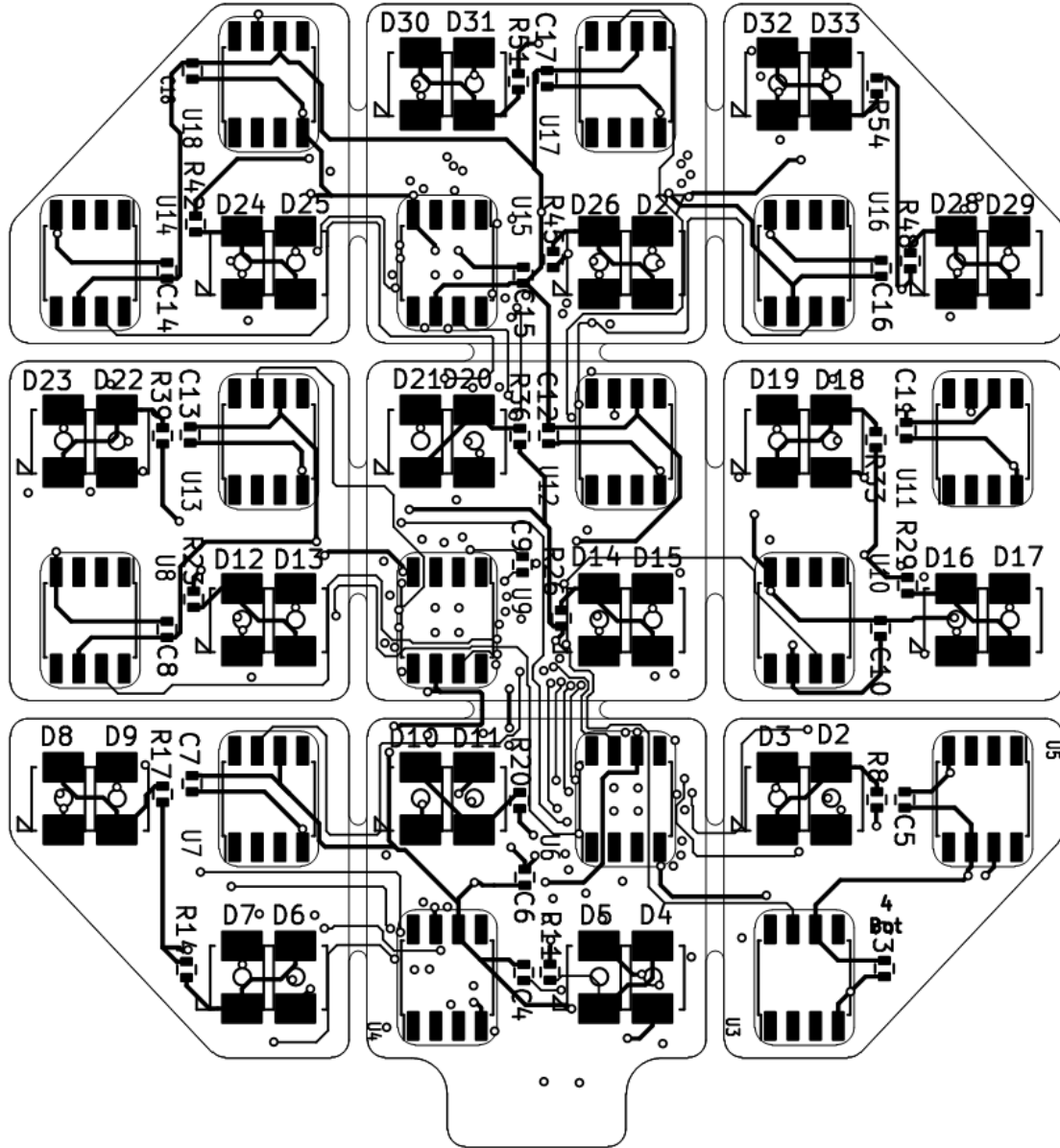


2.2 PCB stack-up





2.3 PCB layout (Flexible bottom layer)

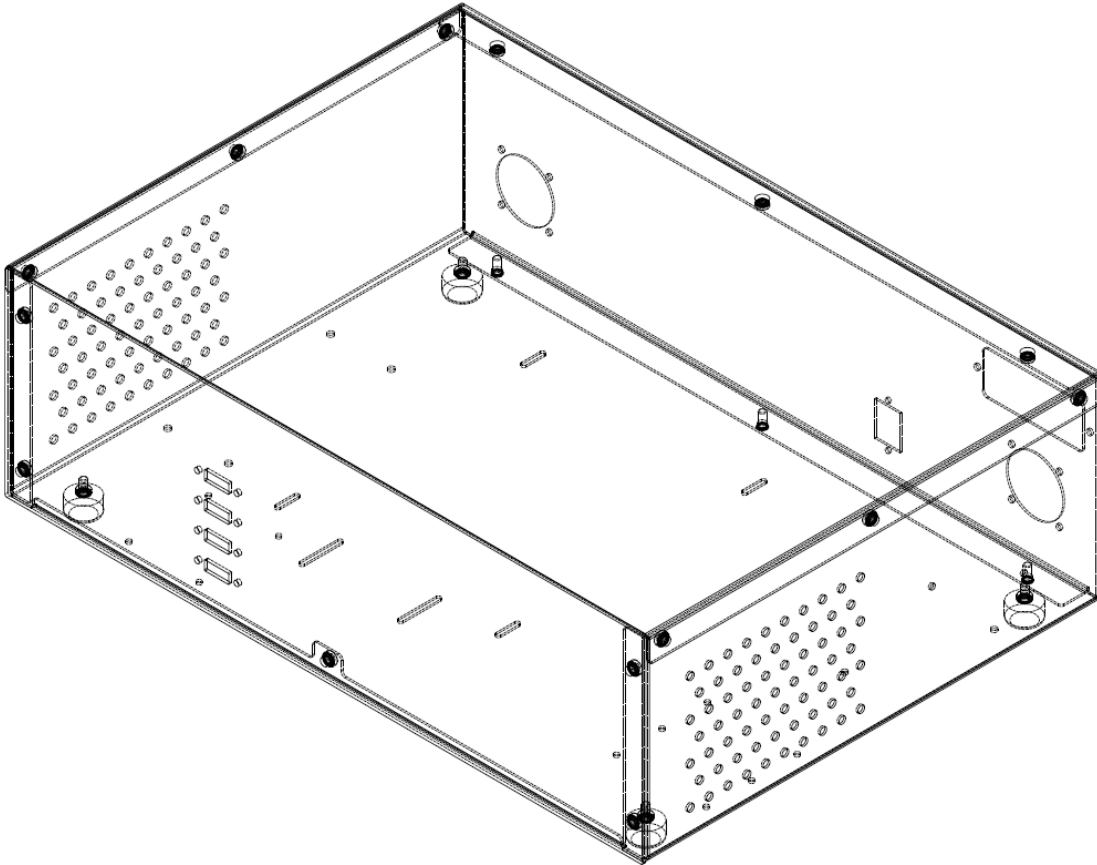


2.5 Contributions

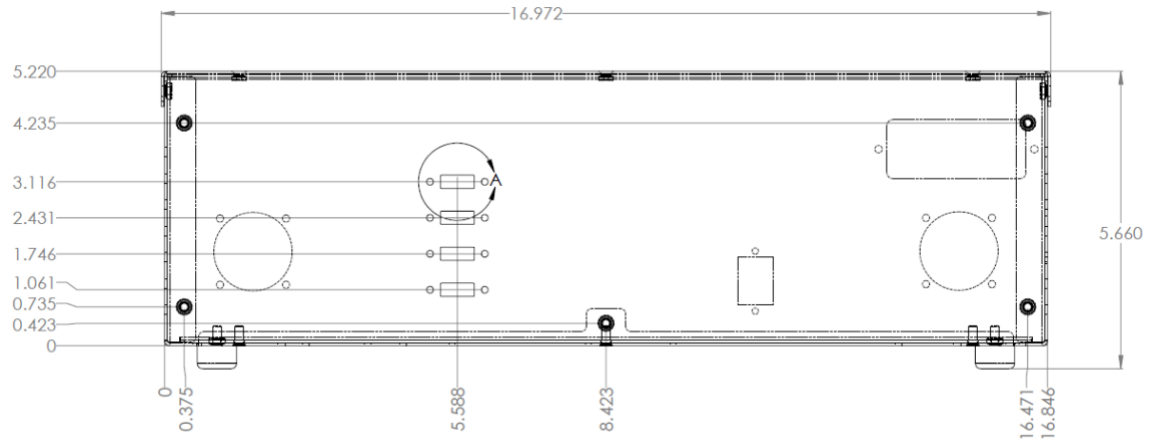
BOTLab and Fraunhofer CMI, USA. both contributed to the schematic capture, component selection, circuit test and troubleshooting.

3. Portable Electronic Enclosure Design

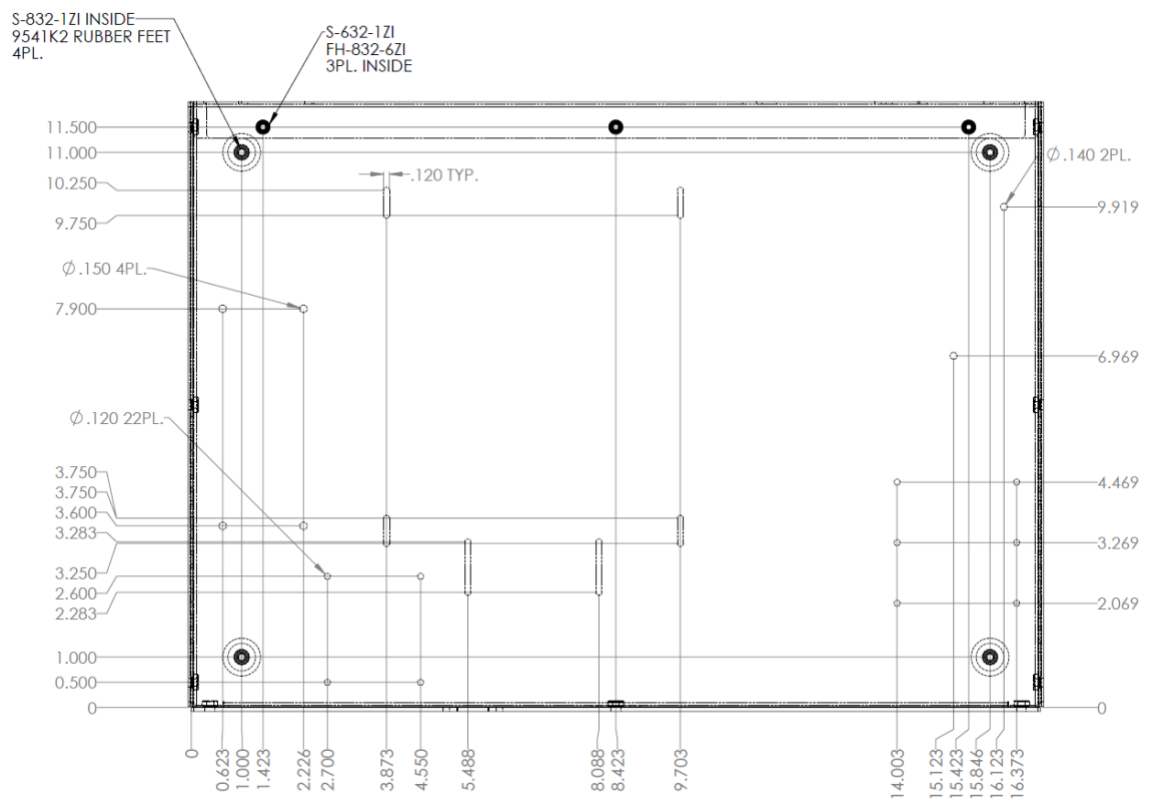
3.1 Overview



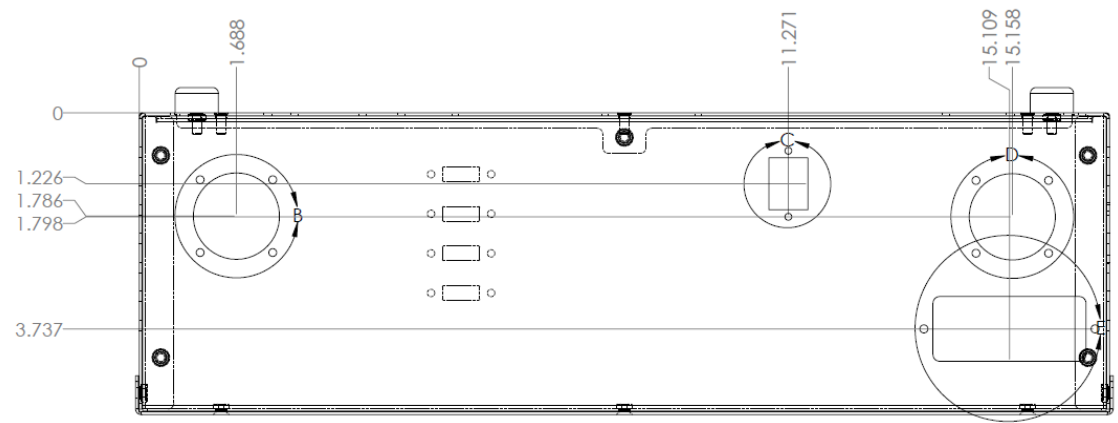
3.1 Front view with dimensions (inch)



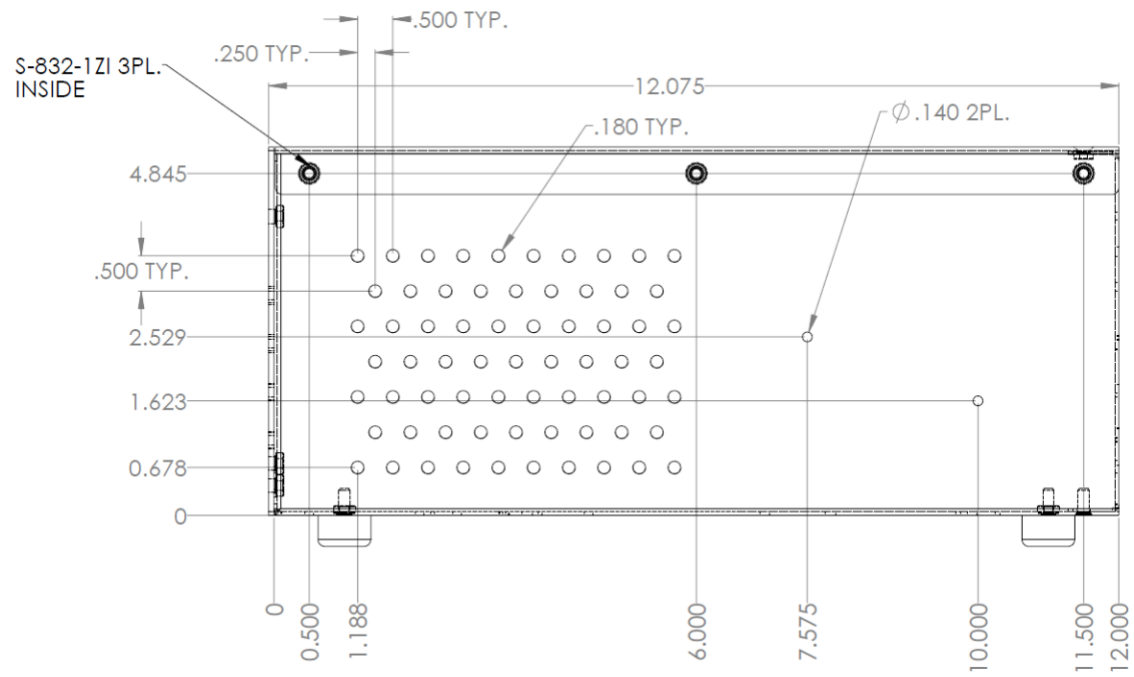
3.2 Bottom view with dimensions (inch)



3.3 Back view with dimensions (inch)



3.4 Side view with dimensions (inch)



3.5 Contributions

This mechanical design is finished by BOTLab, and manufactured by Protocase (Sydney, Nova Scotia, Canada).

4. Blood Liquid Phantom Recipe

Total Volume:

1200ml (in a cylindrical baking can)

Content:

Bovine Blood:	17ml (~25uM Hemoglobin)
	Citrated, Pooled, 100 mL, Carolina Biological Supply Co.
Intralipid:	48ml (~0.8/mm Mus')
	20% Intravenous Fat Emulsion, Fresenius Kabi
PBS solution:	120ml
	Phosphate-Buffered Saline (10X) pH 7.4, ThermoFisher
DI water:	1015ml
HCl (pH = 1):	Optional
NaOH (pH = 13):	Optional

Procedure:

- 1: Collect and pour DI water into baking can.
- 2: Collect and pour PBS solution into a cylindrical baking pan. Stir the solution with a glass stirring rod.
- 3: Collect and pour intralipid into baking pan, Stir the solution again.
- 4: Collect bovine blood with pipette, and transfer blood to baking pan. Stir the solution again.
- 5: Measure and adjust the pH of solution. (in most cases, the pH value is between 7.4 ± 0.5 , which waives PH adjustment)

BIBLIOGRAPHY

- AJCC. 2017. AJCC - Updated Breast Chapter for Eighth Edition.
<https://cancerstaging.org/About/news/Pages/Updated-Breast-Chapter-for-8th-Edition.aspx>.
- American Cancer Society. 2018. Early History of Cancer | American Cancer Society.
<https://www.cancer.org/cancer/cancer-basics/history-of-cancer/what-is-cancer.html>.
- Anderson, P. G., J. M. Kainerstorfer, A. Sassaroli, N. Krishnamurthy, M. J. Homer, R. A. Graham, and S. Fantini. 2015. Broadband Optical Mammography: Chromophore Concentration and Hemoglobin Saturation Contrast in Breast Cancer. *PLoS One* 10 (3):e0117322.
- Arridge, S. R., M. Cope, and D. T. Delpy. 1992. The theoretical basis for the determination of optical pathlengths in tissue: temporal and frequency analysis. *Physics in Medicine and Biology* 37 (7):1531.
- Atsumori, H., M. Kiguchi, A. Obata, H. Sato, T. Katura, T. Funane, and A. Maki. 2009. Development of wearable optical topography system for mapping the prefrontal cortex activation. *The Review of Scientific Instruments* 80 (4):043704.
- Benni, P. B., B. Chen, F. D. Dykes, S. F. Wagoner, M. Heard, A. J. Tanner, T. L. Young, K. Rais-Bahrami, O. Rivera, and B. L. Short. 2005. Validation of the Cas Neonatal NIRS System by Monitoring VV-ECMO Patients. In *Oxygen Transport to Tissue XXVI, Advances in Experimental Medicine and Biology.*, eds. P. Okunieff, J. Williams, and Y. Chen, 195–201. Springer US
http://link.springer.com/chapter/10.1007/0-387-26206-7_27 (last accessed 17 August 2016).
- Bevilacqua, F., A. J. Berger, A. E. Cerussi, D. Jakubowski, and B. J. Tromberg. 2000. Broadband absorption spectroscopy in turbid media by combined frequency-domain and steady-state methods. *Applied Optics* 39 (34):6498–6507.
- Biersack, H.-J., H. Bender, and H. Palmedo. 2008. FDG-PET in Monitoring Therapy of Breast Cancer. In *Breast Cancer*, 181–188. Springer, Berlin, Heidelberg
https://link.springer.com/chapter/10.1007/978-3-540-36781-9_14 (last accessed 29 June 2018).
- Bigio, I. J., and S. Fantini. 2016. *Quantitative Biomedical Optics: Theory, Methods, and Applications*. Cambridge University Press.
- Boas, D. A., T. Gaudette, and S. R. Arridge. 2001. Simultaneous imaging and optode calibration with diffuse optical tomography. *Optics Express* 8 (5):263–270.

- Bozkurt, A., A. Rosen, H. Rosen, and B. Onaral. 2005. A portable near infrared spectroscopy system for bedside monitoring of newborn brain. *BioMedical Engineering OnLine* 4:29.
- Brechon, S. 2012. A Brief History of Breast Cancer. *A Brief History of Breast Cancer*. <https://www.maurerfoundation.org/a-brief-history-of-breast-cancer/> (last accessed 4 July 2018).
- Busch, D. R., R. Choe, M. A. Rosen, W. Guo, T. Durduran, M. D. Feldman, C. Mies, B. J. Czerniecki, J. Tchou, A. DeMichele, M. D. Schnall, and A. G. Yodh. 2013. Optical malignancy parameters for monitoring progression of breast cancer neoadjuvant chemotherapy. *Biomedical Optics Express* 4 (1):105–121.
- Campbell, I. G., S. E. Russell, D. Y. H. Choong, K. G. Montgomery, M. L. Ciavarella, C. S. F. Hooi, B. E. Cristiano, R. B. Pearson, and W. A. Phillips. 2004. Mutation of the PIK3CA Gene in Ovarian and Breast Cancer. *Cancer Research* 64 (21):7678–7681.
- Cerussi, A. E., A. J. Berger, F. Bevilacqua, N. Shah, D. Jakubowski, J. Butler, R. F. Holcombe, and B. J. Tromberg. 2001. Sources of Absorption and Scattering Contrast for Near-Infrared Optical Mammography. *Academic Radiology* 8 (3):211–218.
- Cerussi, A. E., V. W. Tanamai, D. Hsiang, J. Butler, R. S. Mehta, and B. J. Tromberg. 2011. Diffuse optical spectroscopic imaging correlates with final pathological response in breast cancer neoadjuvant chemotherapy. *Philosophical Transactions of the Royal Society of London A: Mathematical, Physical and Engineering Sciences* 369 (1555):4512–4530.
- Cerussi, A. E., V. W. Tanamai, R. S. Mehta, D. Hsiang, J. Butler, and B. J. Tromberg. 2010. Frequent optical imaging during breast cancer neoadjuvant chemotherapy reveals dynamic tumor physiology in an individual patient. *Academic Radiology* 17 (8):1031–1039.
- Cerussi, A., D. Hsiang, N. Shah, R. Mehta, A. Durkin, J. Butler, and B. J. Tromberg. 2007. Predicting response to breast cancer neoadjuvant chemotherapy using diffuse optical spectroscopy. *Proceedings of the National Academy of Sciences of the United States of America* 104 (10):4014–4019.
- Cerussi, A., N. Shah, D. Hsiang, A. Durkin, J. Butler, and B. J. Tromberg. 2006. In vivo absorption, scattering, and physiologic properties of 58 malignant breast tumors determined by broadband diffuse optical spectroscopy. *Journal of Biomedical Optics* 11 (4):044005.
- Chance, B., S. Nioka, J. Zhang, E. F. Conant, E. Hwang, S. Briest, S. G. Orel, M. D. Schnall, and B. J. Czerniecki. 2005. Breast cancer detection based on incremental

- biochemical and physiological properties of breast cancers: a six-year, two-site study. *Academic Radiology* 12 (8):925–933.
- Chen, X., M. O. Moore, C. D. Lehman, D. A. Mankoff, T. J. Lawton, S. Peacock, E. K. Schubert, and R. B. Livingston. 2004. Combined use of MRI and PET to monitor response and assess residual disease for locally advanced breast cancer treated with neoadjuvant chemotherapy¹. *Academic Radiology* 11 (10):1115–1124.
- Choe, R., and T. Durduran. 2012. Diffuse Optical Monitoring of the Neoadjuvant Breast Cancer Therapy. *IEEE Journal of Selected Topics in Quantum Electronics* 18 (4):1367–1386.
- Choe, R., S. D. Konecky, A. Corlu, K. Lee, T. Durduran, D. R. Busch, S. Pathak, B. J. Czerniecki, J. Tchou, D. L. Fraker, A. Demichele, B. Chance, S. R. Arridge, M. Schweiger, J. P. Culver, M. D. Schnall, M. E. Putt, M. A. Rosen, and A. G. Yodh. 2009. Differentiation of benign and malignant breast tumors by in-vivo three-dimensional parallel-plate diffuse optical tomography. *Journal of Biomedical Optics* 14 (2):024020.
- Cipolla, M. J. 2009. *Control of Cerebral Blood Flow*. Morgan & Claypool Life Sciences. <https://www.ncbi.nlm.nih.gov/books/NBK53082/> (last accessed 18 July 2018).
- Corlu, A., T. Durduran, R. Choe, M. Schweiger, E. M. C. Hillman, S. R. Arridge, and A. G. Yodh. 2003. Uniqueness and wavelength optimization in continuous-wave multispectral diffuse optical tomography. *Optics Letters* 28 (23):2339.
- Coyle, S. M., T. E. Ward, and C. M. Markham. 2007. Brain–computer interface using a simplified functional near-infrared spectroscopy system. *Journal of Neural Engineering* 4 (3):219.
- Culver, J. P., R. Choe, M. J. Holboke, L. Zubkov, T. Durduran, A. Slem, V. Ntziachristos, B. Chance, and A. G. Yodh. 2003. Three-dimensional diffuse optical tomography in the parallel plane transmission geometry: evaluation of a hybrid frequency domain/continuous wave clinical system for breast imaging. *Medical Physics* 30 (2):235–247.
- Dakin, J. P., and R. G. W. Brown. 2006. *Handbook of Optoelectronics (Two-Volume Set)*. CRC Press.
- Daly, J. C. 1984. *Fiber Optics*. CRC Press.
- Dave, R. V., R. Millican-Slater, D. Dodwell, K. Horgan, and N. Sharma. 2017. Neoadjuvant chemotherapy with MRI monitoring for breast cancer. *The British Journal of Surgery* 104 (9):1177–1187.

- Delpy, D. T., M. Cope, P. van der Zee, S. Arridge, S. Wray, and J. Wyatt. 1988. Estimation of optical pathlength through tissue from direct time of flight measurement. *Physics in Medicine & Biology* 33 (12):1433.
- Durduran, T., R. Choe, J. P. Culver, L. Zubkov, M. J. Holboke, J. Giammarco, B. Chance, and A. G. Yodh. 2002. Bulk optical properties of healthy female breast tissue. *Physics in Medicine and Biology* 47 (16):2847–2861.
- Eggebrecht, A. T., S. L. Ferradal, A. Robichaux-Viehoever, M. S. Hassanpour, H. Dehghani, A. Z. Snyder, T. Hershey, and J. P. Culver. 2014. Mapping distributed brain function and networks with diffuse optical tomography. *Nature Photonics* 8 (6):448–454.
- Elkin, E. B., C. Hudis, C. B. Begg, and D. Schrag. 2005. The effect of changes in tumor size on breast carcinoma survival in the U.S.: 1975–1999. *Cancer* 104 (6):1149–1157.
- Esserman, L. 2004. Neoadjuvant chemotherapy for primary breast cancer: lessons learned and opportunities to optimize therapy. *Annals of Surgical Oncology* 11 (1 Suppl):3S–8S.
- Esserman, L., N. Hylton, L. Yassa, J. Barclay, S. Frankel, and E. Sickles. 1999. Utility of Magnetic Resonance Imaging in the Management of Breast Cancer: Evidence for Improved Preoperative Staging. *Journal of Clinical Oncology* 17 (1):110–110.
- Falou, O., H. Soliman, A. Sadeghi-Naini, S. Iradji, S. Lemon-Wong, J. Zubovits, J. Spayne, R. Dent, M. Trudeau, J. F. Boileau, F. C. Wright, M. J. Yaffe, and G. J. Czarnota. 2012. Diffuse optical spectroscopy evaluation of treatment response in women with locally advanced breast cancer receiving neoadjuvant chemotherapy. *Translational Oncology* 5 (4):238–246.
- Farrell, T. J., M. S. Patterson, and B. Wilson. 1992. A diffusion theory model of spatially resolved, steady-state diffuse reflectance for the noninvasive determination of tissue optical properties in vivo. *Medical Physics* 19 (4):879–888.
- Flexman, M. L., M. A. Khalil, R. Al Abdi, H. K. Kim, C. J. Fong, E. Desperito, D. L. Hershman, R. L. Barbour, and A. H. Hielscher. 2011. Digital optical tomography system for dynamic breast imaging. *Journal of Biomedical Optics* 16 (7):076014–076014–16.
- Flexman, M. L., H. K. Kim, J. E. Gunther, E. A. Lim, M. C. Alvarez, E. Desperito, K. Kalinsky, D. L. Hershman, and A. H. Hielscher. 2013. Optical biomarkers for breast cancer derived from dynamic diffuse optical tomography. *Journal of Biomedical Optics* 18 (9):096012.

- Flexman, M. L., Y. Li, A. M. Bur, C. J. Fong, J. M. Masciotti, R. Al Abdi, R. L. Barbour, and A. H. Hielscher. 2008. The design and characterization of a digital optical breast cancer imaging system. *Conference proceedings: ... Annual International Conference of the IEEE Engineering in Medicine and Biology Society. IEEE Engineering in Medicine and Biology Society. Annual Conference* 2008:3735–3738.
- Franceschini, M.-A., E. Gratton, D. M. Hueber, and S. Fantini. 1999. Near-infrared absorption and scattering spectra of tissues in vivo. In *SPIE Proceedings, vol. 3597: Optical Tomography and Spectroscopy of Tissue III* 526–531. <http://dx.doi.org/10.1117/12.356854> (last accessed 29 August 2016).
- Fraser, C. M. 1991. *The Merck Veterinary Manual: A Handbook of Diagnosis, Therapy, and Disease Prevention and Control for the Veterinarian*. Merck & Company.
- Gao, L., C. E. Elwell, M. Kohl-Bareis, M. Gramer, C. E. Cooper, T. S. Leung, and I. Tachtsidis. 2011. Effects of Assuming Constant Optical Scattering on Haemoglobin Concentration Measurements Using NIRS during a Valsalva Manoeuvre. In *Oxygen Transport to Tissue XXXII, Advances in Experimental Medicine and Biology.*, eds. J. C. LaManna, M. A. Puchowicz, K. Xu, D. K. Harrison, and D. F. Bruley, 15–20. Springer US http://link.springer.com/chapter/10.1007/978-1-4419-7756-4_3 (last accessed 16 August 2016).
- Garg, P. K., and G. Prakash. 2015. Current definition of locally advanced breast cancer. *Current Oncology* 22 (5):e409–e410.
- Ge, J., B. Zhu, S. Regalado, and A. Godavarty. 2008. Three-dimensional fluorescence-enhanced optical tomography using a hand-held probe based imaging system. *Medical Physics* 35 (7):3354–3363.
- Gu, Y.-L., S.-M. Pan, J. Ren, Z.-X. Yang, and G.-Q. Jiang. 2017. Role of Magnetic Resonance Imaging in Detection of Pathologic Complete Remission in Breast Cancer Patients Treated With Neoadjuvant Chemotherapy: A Meta-analysis. *Clinical Breast Cancer* 17 (4):245–255.
- Gunther, J. E., E. A. Lim, H. K. Kim, M. Flexman, M. Altoé, J. A. Campbell, H. Hibshoosh, K. D. Crew, K. Kalinsky, D. L. Hershman, and A. H. Hielscher. 2018. Dynamic Diffuse Optical Tomography for Monitoring Neoadjuvant Chemotherapy in Patients with Breast Cancer. *Radiology* 287 (3):778–786.
- Hale, G. M., and M. R. Querry. 1973. Optical Constants of Water in the 200-nm to 200- μ m Wavelength Region. *Applied Optics* 12 (3):555–563.
- Hall, J. M., M. K. Lee, B. Newman, J. E. Morrow, L. A. Anderson, B. Huey, and M. C. King. 1990. Linkage of early-onset familial breast cancer to chromosome 17q21. *Science* 250 (4988):1684–1689.

- Heldahl, M. G., S. Lundgren, L. R. Jensen, I. S. Gribbestad, and T. F. Bathen. 2011. Monitoring neoadjuvant chemotherapy in breast cancer patients: improved MR assessment at 3 T? *Journal of Magnetic Resonance Imaging* 34 (3):547–556.
- Intes, X., S. Djeziri, Z. Ichalalene, N. Mincu, Y. Wang, P. St.-Jean, F. Lesage, D. Hall, D. A. Boas, and M. Polyzos. 2004. Time-domain optical mammography Softscan: initial results on detection and characterization of breast tumors. In *Photonics North 2004: Photonic Applications in Astronomy, Biomedicine, Imaging, Materials Processing, and Education*, 188–198. International Society for Optics and Photonics <https://www.spiedigitallibrary.org/conference-proceedings-of-spie/5578/0000/Time-domain-optical-mammography-Softscan--initial-results-on-detection/10.1117/12.593755.short> (last accessed 1 July 2018).
- Izzetoglu, M., K. Izzetoglu, S. Bunce, H. Ayaz, A. Devaraj, B. Onaral, and K. Pourrezaei. 2005. Functional near-infrared neuroimaging. *IEEE Transactions on Neural Systems and Rehabilitation Engineering* 13 (2):153–159.
- Jacques, S. L. 2013. Optical properties of biological tissues: a review. *Physics in Medicine & Biology* 58 (11):R37.
- Jacques, S. L., and B. W. Pogue. 2008. Tutorial on diffuse light transport. *Journal of Biomedical Optics* 13 (4):041302–041302–19.
- Jiang, S., B. W. Pogue, C. M. Carpenter, S. P. Poplack, W. A. Wells, C. A. Kogel, J. A. Forero, L. S. Muffly, G. N. Schwartz, K. D. Paulsen, and P. A. Kaufman. 2009. Evaluation of Breast Tumor Response to Neoadjuvant Chemotherapy with Tomographic Diffuse Optical Spectroscopy: Case Studies of Tumor Region-of-Interest Changes. *Radiology* 252 (2):551–560.
- Jiang, S., B. W. Pogue, P. A. Kaufman, J. Gui, M. Jermyn, T. E. Frazee, S. P. Poplack, R. DiFlorio-Alexander, W. A. Wells, and K. D. Paulsen. 2014. Predicting Breast Tumor Response to Neoadjuvant Chemotherapy with Diffuse Optical Spectroscopic Tomography prior to Treatment. *Clinical Cancer Research* 20 (23):6006–6015.
- Jiang, S., B. W. Pogue, K. E. Michaelsen, M. Jermyn, M. A. Mastanduno, T. E. Frazee, P. A. Kaufman, and K. D. Paulsen. 2013. Pilot study assessment of dynamic vascular changes in breast cancer with near-infrared tomography from prospectively targeted manipulations of inspired end-tidal partial pressure of oxygen and carbon dioxide. *Journal of Biomedical Optics* 18 (7). <http://www.ncbi.nlm.nih.gov/pmc/articles/PMC3706903/> (last accessed 13 September 2016).
- Keam, B., S.-A. Im, Y. Lim, S.-W. Han, H.-G. Moon, D.-Y. Oh, N. Cho, S.-H. Lee, W. Han, W. K. Moon, D.-W. Kim, T.-Y. Kim, I. A. Park, and D.-Y. Noh. 2013. Clinical

- Usefulness of AJCC Response Criteria for Neoadjuvant Chemotherapy in Breast Cancer. *Annals of Surgical Oncology* 20 (7):2242–2249.
- Kelman, G. R. 1966. Digital computer subroutine for the conversion of oxygen tension into saturation. *Journal of Applied Physiology* 21 (4):1375–1376.
- Khan, B., C. Wildey, R. Francis, F. Tian, M. R. Delgado, H. Liu, D. Macfarlane, and G. Alexandrakis. 2012. Improving optical contact for functional near-infrared brain spectroscopy and imaging with brush optodes. *Biomedical Optics Express* 3 (5):878–898.
- Kingston, R. H. 1995. *Optical Sources, Detectors, and Systems: Fundamentals and Applications*. Academic Press.
- Kirilina, E., N. Yu, A. Jelzow, H. Wabnitz, A. M. Jacobs, and I. Tachtsidis. 2013. Identifying and quantifying main components of physiological noise in functional near infrared spectroscopy on the prefrontal cortex. *Frontiers in Human Neuroscience* 7. <http://www.ncbi.nlm.nih.gov/pmc/articles/PMC3865602/> (last accessed 9 September 2016).
- Kocsis, L., P. Herman, and A. Eke. 2006. The modified Beer–Lambert law revisited. *Physics in Medicine and Biology* 51 (5):N91.
- Kuerer, H. M., K. K. Hunt, L. A. Newman, M. I. Ross, F. C. Ames, and S. E. Singletary. 2000. Neoadjuvant chemotherapy in women with invasive breast carcinoma: conceptual basis and fundamental surgical issues. *Journal of the American College of Surgeons* 190 (3):350–363.
- Levenberg, K. 1944. A method for the solution of certain non-linear problems in least squares. *Quarterly of Applied Mathematics* 2 (2):164–168.
- Li, J., C. Yen, D. Liaw, K. Podsypanina, S. Bose, S. I. Wang, J. Puc, C. Miliaresis, L. Rodgers, R. McCombie, S. H. Bigner, B. C. Giovanella, M. Ittmann, B. Tycko, H. Hibshoosh, M. H. Wigler, and R. Parsons. 1997. PTEN, a Putative Protein Tyrosine Phosphatase Gene Mutated in Human Brain, Breast, and Prostate Cancer. *Science* 275 (5308):1943–1947.
- Li, L., M. Cazzell, O. Babawale, and H. Liu. 2016. Automated voxel classification used with atlas-guided diffuse optical tomography for assessment of functional brain networks in young and older adults. *Neurophotonics* 3 (4):045002.
- Li, T., Y. Lin, Y. Shang, L. He, C. Huang, M. Szabunio, and G. Yu. 2013. Simultaneous measurement of deep tissue blood flow and oxygenation using noncontact diffuse correlation spectroscopy flow-oximeter. *Scientific Reports* 3:1358.

- Macnab, A. J., and L. Stothers. 2008. Development of a near-infrared spectroscopy instrument for applications in urology. *The Canadian Journal of Urology* 15 (5):4233–4240.
- Madsen, K., H. Nielsen, and O. Tingleff. 2004. Methods for Non-Linear Least Squares Problems (2nd ed.). http://www2.imm.dtu.dk/pubdb/views/edoc_download.php/3215/pdf/imm3215.pdf (last accessed 18 July 2018).
- Malkin, D., F. P. Li, L. C. Strong, C. E. Nelson, D. H. Kim, and et al. 1990. Germ Line p53 Mutations in a Familial Syndrome of Breast Cancer, Sarcomas, and Other Neoplasms. *Science* 250 (4985):1233.
- Marquardt, D. 1963. An Algorithm for Least-Squares Estimation of Nonlinear Parameters. *Journal of the Society for Industrial and Applied Mathematics* 11 (2):431–441.
- Matcher, S. J., M. Cope, and D. T. Delpy. 1997. In vivo measurements of the wavelength dependence of tissue-scattering coefficients between 760 and 900 nm measured with time-resolved spectroscopy. *Applied Optics* 36 (1):386.
- McKendrick, R., R. Parasuraman, and H. Ayaz. 2015. Wearable functional near infrared spectroscopy (fNIRS) and transcranial direct current stimulation (tDCS): expanding vistas for neurocognitive augmentation. *Frontiers in Systems Neuroscience* :27.
- Muehleemann, T., D. Haensse, and M. Wolf. 2008. Wireless miniaturized in-vivo near infrared imaging. *Optics Express* 16 (14):10323.
- Nam, K., J. R. Eisenbrey, M. Stanczak, A. Sridharan, A. C. Berger, T. Avery, J. P. Palazzo, and F. Forsberg. 2017. Monitoring Neoadjuvant Chemotherapy for Breast Cancer by Using Three-dimensional Subharmonic Aided Pressure Estimation and Imaging with US Contrast Agents: Preliminary Experience. *Radiology* 285 (1):53–62.
- National Cancer Institute. 2018. Female Breast Cancer - Cancer Stat Facts. *Cancer Stat Facts: Female Breast Cancer*. <https://seer.cancer.gov/statfacts/html/breast.html>.
- Olesen, B. 1982. Thermal Comfort. *Technical Review* 11:3–37.
- Parkes, M. J. 2006. Breath-holding and its breakpoint. *Experimental Physiology* 91 (1):1–15.
- Perdue, K. L., Q. Fang, and S. G. Diamond. 2012. Quantitative assessment of diffuse optical tomography sensitivity to the cerebral cortex using a whole-head probe. *Physics in Medicine & Biology* 57 (10):2857.

- Pham, T. H., O. Coquoz, J. B. Fishkin, E. Anderson, and B. J. Tromberg. 2000. Broad bandwidth frequency domain instrument for quantitative tissue optical spectroscopy. *Review of Scientific Instruments* 71 (6):2500–2513.
- Pinti, P., C. Aichelburg, F. Lind, S. Power, E. Swingler, A. Merla, A. Hamilton, S. Gilbert, P. Burgess, and I. Tachtsidis. 2015. Using Fiberless, Wearable fNIRS to Monitor Brain Activity in Real-world Cognitive Tasks. *Journal of Visualized Experiments: JoVE* (106).
- Piper, S. K., A. Krueger, S. P. Koch, J. Mehnert, C. Habermehl, J. Steinbrink, H. Obrig, and C. H. Schmitz. 2014. A wearable multi-channel fNIRS system for brain imaging in freely moving subjects. *NeuroImage* 85, Part 1:64–71.
- Pogue, B., M. Testorf, T. McBride, U. Osterberg, and K. Paulsen. 1997. Instrumentation and design of a frequency-domain diffuse optical tomography imager for breast cancer detection. *Optics Express* 1 (13):391.
- Prahl, S. 1998. Tabulated Molar Extinction Coefficient for Hemoglobin in Water. <https://omlc.org/spectra/hemoglobin/summary.html> (last accessed 4 July 2018).
- Ragaz, J., P. R. Band, and J. H. Goldie. 2012. *Preoperative (Neoadjuvant) Chemotherapy*. Springer Science & Business Media.
- Rigter, L. S., C. E. Loo, S. C. Linn, G. S. Sonke, E. van Werkhoven, E. H. Lips, H. A. Warnars, P. K. Doll, A. Bruining, I. A. Mandjes, M. J. V. Peeters, J. Wesseling, K. G. Gilhuijs, and S. Rodenhuis. 2013. Neoadjuvant chemotherapy adaptation and serial MRI response monitoring in ER-positive HER2-negative breast cancer. *British Journal of Cancer* 109 (12):2965–2972.
- Roblyer, D., S. Ueda, A. Cerussi, W. Tanamai, A. Durkin, R. Mehta, D. Hsiang, J. A. Butler, C. McLaren, W.-P. Chen, and B. Tromberg. 2011. Optical imaging of breast cancer oxyhemoglobin flare correlates with neoadjuvant chemotherapy response one day after starting treatment. *Proceedings of the National Academy of Sciences of the United States of America* 108 (35):14626–14631.
- Schelling, M., N. Avril, J. Nährig, W. Kuhn, W. Römer, D. Sattler, M. Werner, J. Dose, F. Jänicke, H. Graeff, and M. Schwaiger. 2000. Positron Emission Tomography Using [18F]Fluorodeoxyglucose for Monitoring Primary Chemotherapy in Breast Cancer. *Journal of Clinical Oncology* 18 (8):1689–1695.
- Scholkmann, F., and M. Wolf. 2013. General equation for the differential pathlength factor of the frontal human head depending on wavelength and age. *Journal of Biomedical Optics* 18 (10):105004–105004.

- SEER Cancer Statistics Review. 2018. SEER Cancer Statistics Review (CSR), 1975-2015. https://seer.cancer.gov/csr/1975_2015/sections.html.
- Shah, N., A. E. Cerussi, D. Jakubowski, D. Hsiang, J. Butler, and B. J. Tromberg. 2004. Spatial variations in optical and physiological properties of healthy breast tissue. *Journal of Biomedical Optics* 9 (3):534–540.
- Shah, N., A. Cerussi, C. Eker, J. Espinoza, J. Butler, J. Fishkin, R. Hornung, and B. Tromberg. 2001a. Noninvasive functional optical spectroscopy of human breast tissue. *Proceedings of the National Academy of Sciences of the United States of America* 98 (8):4420–4425.
- . 2001b. Noninvasive functional optical spectroscopy of human breast tissue. *Proceedings of the National Academy of Sciences of the United States of America* 98 (8):4420–4425.
- Soliman, H., A. Gunasekara, M. Rycroft, J. Zubovits, R. Dent, J. Spayne, M. J. Yaffe, and G. J. Czarnota. 2010. Functional Imaging Using Diffuse Optical Spectroscopy of Neoadjuvant Chemotherapy Response in Women with Locally Advanced Breast Cancer. *Clinical Cancer Research* 16 (9):2605–2614.
- Spinelli, L., A. Torricelli, A. Pifferi, P. Taroni, G. Danesini, and R. Cubeddu. 2005. Characterization of female breast lesions from multi-wavelength time-resolved optical mammography. *Physics in Medicine and Biology* 50 (11):2489–2502.
- Srinivasan, S., B. W. Pogue, S. Jiang, H. Dehghani, C. Kogel, S. Soho, J. J. Gibson, T. D. Tosteson, S. P. Poplack, and K. D. Paulsen. 2006. In vivo hemoglobin and water concentrations, oxygen saturation, and scattering estimates from near-infrared breast tomography using spectral reconstruction. *Academic Radiology* 13 (2):195–202.
- Steligo, K. 2017. *The Breast Reconstruction Guidebook: Issues and Answers from Research to Recovery*. JHU Press.
- Stojanovic, R., and D. Karadaglic. 2013. Design of an Oximeter Based on LED-LED Configuration and FPGA Technology. *Sensors* 13 (1):574–586.
- Tadayyon, H., L. Sannachi, M. Gangeh, A. Sadeghi-Naini, W. Tran, M. E. Trudeau, K. Pritchard, S. Ghandi, S. Verma, and G. J. Czarnota. 2016. Quantitative ultrasound assessment of breast tumor response to chemotherapy using a multi-parameter approach. *Oncotarget* 7 (29):45094–45111.
- Tamura, M., Y. Hoshi, and F. Okada. 1997. Localized near-infrared spectroscopy and functional optical imaging of brain activity. *Philosophical Transactions of the Royal Society B: Biological Sciences* 352 (1354):737–742.

- Taroni, P., A. Pifferi, G. Quarto, L. Spinelli, A. Torricelli, F. Abbate, A. Villa, N. Balestreri, S. Menna, E. Cassano, and R. Cubeddu. 2010. Noninvasive assessment of breast cancer risk using time-resolved diffuse optical spectroscopy. *Journal of Biomedical Optics* 15 (6):060501.
- Teng, F., T. Cormier, A. Sauer-Budge, R. Chaudhury, V. Pera, R. Istfan, D. Chargin, S. Brookfield, N. Y. Ko, and D. M. Roblyer. 2017. Wearable near-infrared optical probe for continuous monitoring during breast cancer neoadjuvant chemotherapy infusions. *Journal of Biomedical Optics* 22 (1):014001–014001.
- Tisdall, M. M., C. Taylor, I. Tachtsidis, T. S. Leung, C. Pritchard, C. E. Elwell, and M. Smith. 2009. The Effect on Cerebral Tissue Oxygenation Index of Changes in the Concentrations of Inspired Oxygen and End-Tidal Carbon Dioxide in Healthy Adult Volunteers. *Anesthesia and Analgesia* 109 (3):906–913.
- Tong, Y., K. P. Lindsey, and B. deB Frederick. 2011. Partitioning of physiological noise signals in the brain with concurrent near-infrared spectroscopy and fMRI. *Journal of Cerebral Blood Flow & Metabolism* 31 (12):2352–2362.
- Torjesen, A., R. Istfan, and D. Roblyer. 2017. Ultrafast wavelength multiplexed broad bandwidth digital diffuse optical spectroscopy for in vivo extraction of tissue optical properties. *Journal of Biomedical Optics* 22 (3):36009.
- Toronov, V., M. A. Franceschini, M. Filiaci, S. Fantini, M. Wolf, A. Michalos, and E. Gratton. 2000. Near-infrared study of fluctuations in cerebral hemodynamics during rest and motor stimulation: Temporal analysis and spatial mapping. *Medical Physics* 27 (4):801–815.
- Torricelli, A., L. Spinelli, A. Pifferi, P. Taroni, R. Cubeddu, and G. Danesini. 2003. Use of a nonlinear perturbation approach for in vivo breast lesion characterization by multiwavelength time-resolved optical mammography. *Optics Express* 11 (8):853.
- Ueda, S., D. Roblyer, A. Cerussi, A. Durkin, A. Leproux, Y. Santoro, S. Xu, T. D. O’Sullivan, D. Hsiang, R. Mehta, J. Butler, and B. J. Tromberg. 2012. Baseline tumor oxygen saturation correlates with a pathologic complete response in breast cancer patients undergoing neoadjuvant chemotherapy. *Cancer Research* 72 (17):4318–4328.
- Wang, L., S. L. Jacques, and L. Zheng. 1995. MCML—Monte Carlo modeling of light transport in multi-layered tissues. *Computer Methods and Programs in Biomedicine* 47 (2):131–146.
- Welsh, J. 2013. Chapter 40 - Animal Models for Studying Prevention and Treatment of Breast Cancer. In *Animal Models for the Study of Human Disease*, ed. P. M. Conn,

- 997–1018. Boston: Academic Press
<http://www.sciencedirect.com/science/article/pii/B9780124158948000403>.
- Wooster, R., G. Bignell, J. Lancaster, S. Swift, S. Seal, J. Mangion, N. Collins, S. Gregory, C. Gumbs, and G. Micklem. 1995. Identification of the breast cancer susceptibility gene BRCA2. *Nature* 378 (6559):789–792.
- Yoo, K. M., F. Liu, and R. R. Alfano. 1990. When does the diffusion approximation fail to describe photon transport in random media? *Physical Review Letters* 64 (22):2647–2650.
- Yu, G., T. Durduran, D. Furuya, J. H. Greenberg, and A. G. Yodh. 2003. Frequency-domain multiplexing system for in vivo diffuse light measurements of rapid cerebral hemodynamics. *Applied Optics* 42 (16):2931.
- Yu, Y., A. Sassaroli, D. K. Chen, M. J. Homer, R. A. Graham, and S. Fantini. 2010. Near-infrared, broad-band spectral imaging of the human breast for quantitative oximetry: applications to healthy and cancerous breasts. *Journal of Innovative Optical Health Sciences* 03 (04):267–277.
- Yuan, G., U. Alqasemi, A. Chen, Y. Yang, and Q. Zhu. 2014. Light-emitting diode-based multiwavelength diffuse optical tomography system guided by ultrasound. *Journal of Biomedical Optics* 19 (12):126003.
- Zhang, Q., X. Yan, and G. E. Strangman. 2011. Development of motion resistant instrumentation for ambulatory near-infrared spectroscopy. *Journal of Biomedical Optics* 16 (8):087008.
- Zhou, C., R. Choe, N. Shah, T. Durduran, G. Yu, A. Durkin, D. Hsiang, R. Mehta, J. Butler, A. Cerussi, B. J. Tromberg, and A. G. Yodh. 2007. Diffuse optical monitoring of blood flow and oxygenation in human breast cancer during early stages of neoadjuvant chemotherapy. *Journal of Biomedical Optics* 12 (5):051903.
- Zhu, Q., S. Tannenbaum, P. Hegde, M. Kane, C. Xu, and S. H. Kurtzman. 2008. Noninvasive Monitoring of Breast Cancer during Neoadjuvant Chemotherapy Using Optical Tomography with Ultrasound Localization. *Neoplasia* 10 (10):1028–1040.

VITA

